ALMA MATER STUDIORUM
UNIVERSITÀ DI BOLOGNA

DOTTORATO DI RICERCA IN

SCIENZE E TECNOLOGIE AEROSPAZIALI

Ciclo 36

Settore Concorsuale: 09/A1 - INGEGNERIA AERONAUTICA, AEROSPAZIALE E NAVALE

Settore Scientifico Disciplinare: ING-IND/03 - MECCANICA DEL VOLO

ATTITUDE AND TRAJECTORY CONTROL SYSTEM DESIGN FOR THE EMERGENCY MANEUVER OF AN UNMANNED HELICOPTER

Presentata da: Daniele Fattizzo

Coordinatore Dottorato

Alessandro Talamelli

Supervisore

Fabrizio Giulietti

Co-supervisore

Emanuele Luigi De Angelis

Esame finale anno 2024

Abstract

The constant growth in the Unmanned Aerial Systems industrial sector, and the perspective of new applications in various, operational scenarios pose a challenge in the development of more performing and safe systems. In this context, crucial importance will be the development of systems with higher emergency management capabilities and enhanced control performance.

Within the wide panorama of the UAVs, the helicopter configuration, due to features related to variable-pitch flapping rotor, is gaining an increasing interest w.r.t traditional multirotors. Variable-pitch flapping rotor gives the helicopter, two relevant advantages: a major cargo capability, and the possibility to perform the autorotation maneuver, which represents a valuable resource for improving safety. This is a safe landing maneuver, which is performed in the case of engine failure or severe tail damage. During the autorotation, the helicopter reaches a steady descent condition, where the rotor is driven by the impinging flow, and a negative collective pitch is imposed.

The main objectives of this thesis are 1) the development of the automatic autorotation maneuver for a small-scale helicopter, and 2) the implementation of a nonlinear dynamic controller, allowing precise reference attitude and velocity track-

ing. The design of a suitable maneuver has been conducted by dividing the maneuver into its two fundamental phases and analyzing the key variables to be considered and controlled. In particular, all the possible steady descent conditions were calculated with a trim algorithm, and a suitable flare profile was adopted and optimized. A PID-based control architecture has been adopted to follow the nominal autorotation maneuver in a closed loop. Several simulations have been considered to test the maneuver for a wide range of different initial conditions.

Also, a nonlinear dynamic inversion controller made of an inner loop for attitude stabilization and an outer loop for velocity control has been designed. The attitude control systems has been derived by inverting a medium-order helicopter rotational dynamics model, while for the velocity controller, a simpler translational dynamics system has been developed. To ensure adequate control performance, an extended Kalman filter allowing the estimation of the inflow ratio, has been developed and implemented. An extensive simulation campaign has been conducted in order to validate the controller in different flight maneuvers, including the autorotation.

Contents

List of Tables

List of Figures

Nomenclature

a_0, a_1, b_1 Main rotor coning, longitudinal and lateral flapping angles in rotor-hub system (rad)

A_{1c}, B_{1c} Lateral and longitudinal cyclic pitch measured from hub plane in Wind-Hub system (rad)

A_{1S}, B_{1s} Lateral and longitudinal cyclic pitch measured from hub plane in Hub-Body system(rad)

C_{l_α} Profile lift slope

e Flapping hinge offset (m)

$F_{()} = [X\, Y\, Z]^T$ Forces vector (N)

i_s Main rotor longitudinal tilt angle (rad)

I Inertia matrix in body axes (kg/m2)

K_1 Pitch-flap coupling ratio

M_β Blade weight moment about the flapping hinge (Nm)

m Total mass(kg)

$M_{()} = [L\, M\, N]^T$ Moments vector (Nm)

R Rotor radius (m)

U_P, U_T Normal and parallel blade element velocity components wrt the blade chord on the hub plane (m/s)

$V_{()} = [u\, v\, w]^T$ Linear velocity vector (m/s)

v_i induced velocity

Greek symbols

β Blade flapping angle (rad)

δ Main rotor profile drag coefficient

$\varepsilon = \frac{e}{R}$ Hinge offset ratio

θ_0, θ_{tr} Main rotor and tail rotor collective pitch (rad)

$\lambda = (w_h - v_i)/(\Omega\, R)$ Inflow ratio

$\lambda_i = v_i/(\Omega\, R)$ induced inflow ratio

$\mu = \sqrt{u_h^2 + v_h^2}/(\Omega\, R)$ Advance ratio

$\Xi = [\Phi\, \Theta\, \Psi]^T$ Roll, pitch and yaw angles(rad)

$\omega_{()} = [p\, q\, r]^T$ Angular velocity vector (rad/s)

Ω	Rotor angular velocity (rad/s)

Subscripts

b	Body frame
ccl	Counter-clockwise
cl	Clockwise
e	Earth fixed NED frame
fus	Fuselage
h	Hub-Body frame
LV	Local-Vertical frame
mr	Main rotor
sd	Steady descent
tr	Tail rotor
w	Wind-Hub frame

Chapter 1

Introduction

1.1 Problem definitions and motivations

The use of unmanned aerial systems for civil applications in various operational scenarios has been steadily increasing over the last two decades, especially for remote sensing, and enviromental applications. In this respect, the use of this relatively novel class of vehicles is already rather common in agriculture [28], construction sites [29, 31, 51], airports [14, 48, 49] and in many other contexts where their use provides an advantage over traditional piloted vehicles in terms of cost reduction and effectiveness, such as inspections, monitoring, environmental control and protection, remote sensing, mapping services, and, in a nowadays near future, parcel delivery.

With the rapid growth of the applications, the need to guarantee publicly acceptable levels of safety immediately became one of the most relevant issues for regulatory authorities. If the UAS eliminates risks and dangers for the pilot on board, still high risk is present for everything in the flight areas and on the ground (things and people) with the related potential material and human damages. The possibility of further

future developments, especially for larger autonomous aerial vehicles for transport and urban air mobility, is strictly related to their reliability, and capabilities to handle emergency situations. Thus safety standards shall be required for operating such vehicles over populated areas.

Several studies have already carried out trying to define risk evaluation models and risk mitigation techniques. The flight risk in these studies is a function of the flight context (surrounded area characteristics, mission features,etc). In Ref. [4] the risk on the ground is evaluated for a given trajectory, as a function of the population density, the vehicle reliability, and the time of flight over a specific position. Ref. [48] addresses the problem of collision risk for UAS operating in the airport environment, defining a collision risk model able to introduce alert zones based on a probabilistic conflict map. Ref. [42] compare different safety evolution models applied to a real mission case. Several studies have also highlighted how to minimize the risk avoiding dangerous areas [37] or improving vehicles' maneuverability and emergency-management capabilities. To this aim, the approaches to improve vehicles safety shall include the following two aspects: i) the vehicle intrinsic safety improvement, i.e. the study of configurations and control systems capable of making the flight as stable and safe as possible, and, ii) the possibility of concentrate on effective emergency management. As a result, a great effort is put in studying of advanced guidance systems ensuring obstacle detection and collision avoidance during the flight [17, 32, 35, 44].

A crucial role is also played by the GNC technologies allowing for the real-time tracking of planned trajectories [16, 45], and the automatic and autonomous systems

[6].

In this context, the main purpose of the present thesis is the study, implementation and validation of the automatic helicopter autorotation maneuver, allowing the aircraft to safely land after the engine failure. In particular, the following two objectives have been addressed:

- The design and simulation of the automatic autorotation maneuver, by taking into account constraints on initial conditions
- The implementation of an advanced control system based on the nonlinear dynamic inversion technique (NDI)

For such activities, a model-based design approach has been adopted. Starting from the mathematical model of the helicopter dynamics, a simulation environment has been realized. Other simplified models have also been considered for the optimization of the autorotation maneuver, for the design of the NDI controllers, and for the development of an extended Kalman filter for the mean inflow ratio estimation.

The automatic autorotation maneuver was studied, firstly investigating the key variables for the autorotation steady conditions, then with an off-line design of a nominal maneuver, and finally through the design, implementation, and simulation of a control system to perform this maneuver. The objective was to obtain a control system to perform an automatic autorotation maneuver after a powerplant failure. The system should bring the helicopter to the ground with acceptable residual velocity avoiding crashes. No constraints were considered on the final position of the helicopter.

The NDI approach has been selected because it may garantee increased performance in the case of complex dynamic systems. The proposed control architecture is a classical nested-loop structure, where the inner loop allows the attitude stabilization, whereas the outer loop provides the tracking of a commanded velocity. An extended Kalman filter for the inflow estimation has been implemented since NDI controller depends on the system state feedback.

1.2 The helicopter platform

Common UAVs scenarios include operations within unprepared or confined sites, such as urban spaces, high mountain environments, natural canyons, forests, naval ships, etc. Such scenarios require vertical takeoff/landing, hovering, and longitudinal/lateral flight capabilities. This makes the helicopter configuration a suitable candidate platform. Besides its maneuverability, the advantages of the helicopter configuration, with respect to classical multirotor configurations, are strictly related to the presence of a pitch variable flapping rotor. This characteristic determines higher cargo capabilities, especially when compact dimensions are required. Moreover, helicopters generally present wider flight envelope thus wider flight possibilities. An additional and crucial advantage is the possibility of the autorotation maneuver. Since other emergency safety systems, as parachutes [18, 31], are less common and less suitable for helicopters, the autorotation maneuver become a relevant resourche to improve their reliability. Unfortunately, from the flight safety point of view, the main limit is given by their natural instability. This made them more difficult to stabilize and control, posing the necessity of continuous research on control systems.

Mini-UAVs helicopters are commonly upgraded from Remote-Controlled (RC) hobby helicopters, by assembling an avionics suite. The role of this avionics suite is to collect and integrate various measurement signals, drive the actuators, provide communications with a Ground Control Station (GCS), and support real-time operations of automatic/autonomous flight control laws. From a control system point of view, helicopter systems can be characterized as Multiple-Input Multiple-Output (MIMO), under-actuated, nonlinear, and unstable dynamics. When compared to their full-size helicopter counterparts, or even to larger-size helicopter UAVs, small scale helicopter UAVs feature an increased power-to-mass ratio, an increase in stiffness of the main rotor assembly, and a higher torque-to-inertia ratio. Consequently, they are much more agile at the cost of higher levels of dynamics coupling and instability [34].

A brief description of the helicopter's main characteristics and flight is given in the following. As with all flying systems, an equilibrium between all the forces acting on the helicopter is what determines the flight. As visible in Fig. 1.1 three are the main forces acting on the helicopter: the thrust T, the drag D, and the weight W. The thrust is given by the main rotor aerodynamics and has the role of: i) overcoming the drag with its horizontal components to guarantee the advancing motion and ii) equilibrating the weight with its vertical component to make the system fly. The thrust originates from the descendent airflow induced by the rotor movement; the drag is a rearward force caused by the disruption of airflow by the moving rotors and vehicle.

In a standard helicopter configuration, a small tail rotor is mounted at the end of

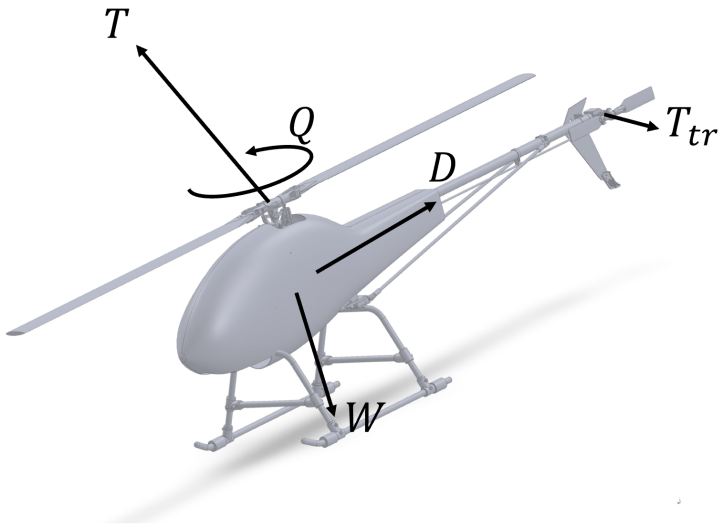

Figure 1.1: Scheme of the main forces and moments on the helicopter

the tail boom to produce a lateral thrust T_{tr}. This force generates a moment about the helicopter center of mass equilibrating the aerodynamic torque Q generated by the movement of the main rotor in the air.

The main characteristic of the helicopter is the flapping dynamics of the rotor blades. In the rotation around the rotor shaft, the blades generate a rotor disk or, more properly, a rotor cone (Fig. 1.2). This is due to the equilibrium established, for every single blade, around the rotor hub between the moments due to the blade weight, the aerodynamic lift and the centrifugal force. The inclination of the rotor cone depends on the flapping coefficients, namely the coning angle a_0, and the longitudinal and lateral flapping angles a_1 and b_1. If these angles change, even the direction of the thrust is modified. The helicopter control is based on the idea of changing the rotor thrust inclination to obtain different forces and moments

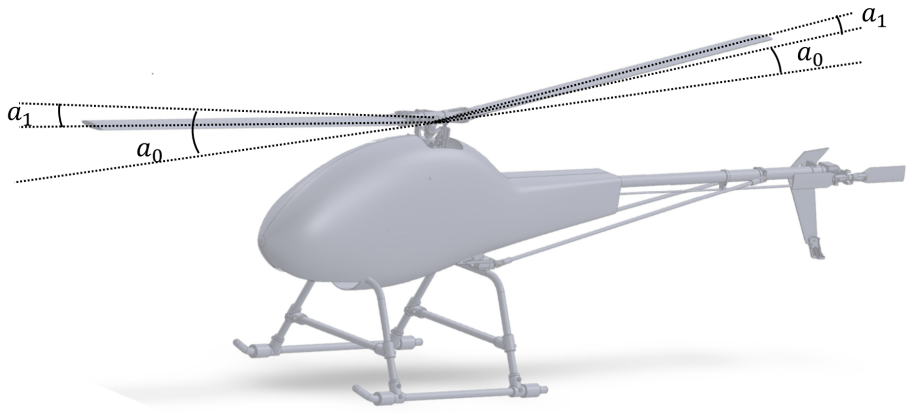

Figure 1.2: Flapping angles in the longitudinal plane

equilibrium, and then different flight conditions.

The manned helicopters have four separate flight control inputs, which allow for control of the attitude roll, pitch, and yaw angles. The controls are known as main rotor collective, main rotor longitudinal cyclic, main rotor lateral cyclic, and tail rotor anti-torque pedals. These pilot inputs are, in manned helicopters, connected to the main rotor swash plate and the tail rotor pitch lever, which are the final parts of the command chain of the system. In unmanned helicopters, all the actuators are servos, and, since there is no reason to talk about "pedals", the tail rotor command is simply called tail rotor pitch. The main rotor collective changes the pitch angle of all main rotor blades collectively, and independently of the blade rotational position. Through the collective, one can increase or decrease the total thrust derived from the main rotor. On the other hand, the main rotor cyclics change the pitch angle of the main rotor blades cyclically, i.e. the pitch angle of the rotor blades change depending

upon their position, as they rotate around the main rotor hub. A representation of the main rotor shaws-plate is reported in Fig. 1.3: here the blade incidence varies moving the pitch levers which tilt the swash plate that is connected to the rotor hub through the pitch links. The swashing plate is composed of a lower non-rotating part, connected to the pitch levers, and an upper rotating part connected to the blades. The pitch levers are, in turn, connected to a mixing unit which receives the pilot input by a further chain (for the manned helicopters) or by servos which are commanded by the board computer according to remote controls and/or control systems algorithms.

The pitch angle of every single blade varies during the rotation around the hub as a function of the azimuth ψ_{bl} according to:

$$\theta(\psi_{bl}) = \theta_0 - A_{1s}\cos\psi_{bl} - B_{1s}\sin\psi_{bl} \tag{1.1}$$

where θ_0 is the main rotor collective pitch and is imposed with a vertical movement of the swash plate, while A_{1s} and B_{1s} are the lateral and longitudinal cyclic pitches which tilt the swash plate. The fourth command of the helicopter, the tail rotor pitch is denoted by θ_{tr}. Note that the longitudinal pitch A_{1s} is defined to make the swashing plate tilt laterally while the lateral pitch B1s tilts the swashing plate longitudinally (Fig. 1.4). This is because, due to the flapping dynamic characteristics, an approximately 90° phase shift is established between the swashplate and the rotor cone orientations.

The primary effects of the four commands are briefly listed here:

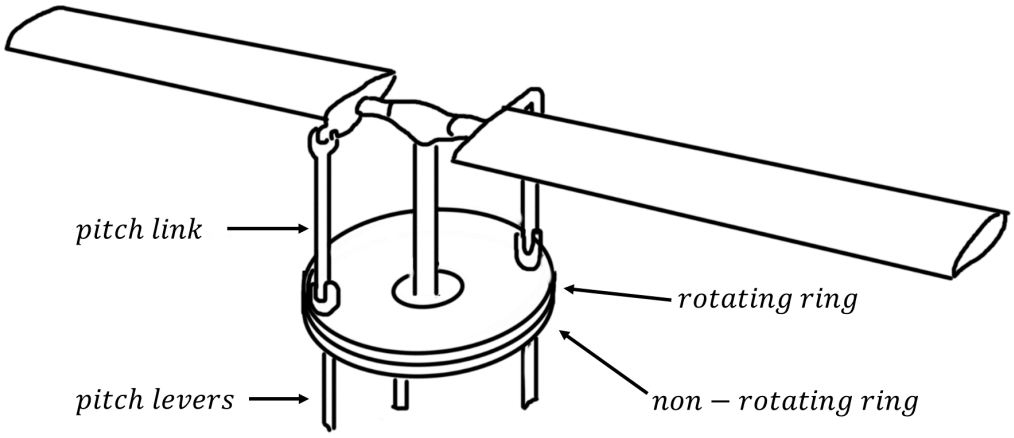

Figure 1.3: Swash plate

- the main rotor collective θ_0 is used to module the rotor thrust and to act on the equilibrium along z_b
- the lateral pitch A_{1s} primarily induces a roll moment to the hub tilting the rotor disk laterally
- the longitudinal pitch B_{1s} primarily induces a pitch moment to the hub tilting the rotor disk longitudinally
- the tail rotor pitch θ_{tr} is used to module the tail rotor thrust to equilibrate the yaw moment due to the main rotor aerodynamic torque or to generate a yaw moment

During nominal flight conditions, the rotor angular rate is kept constant at the

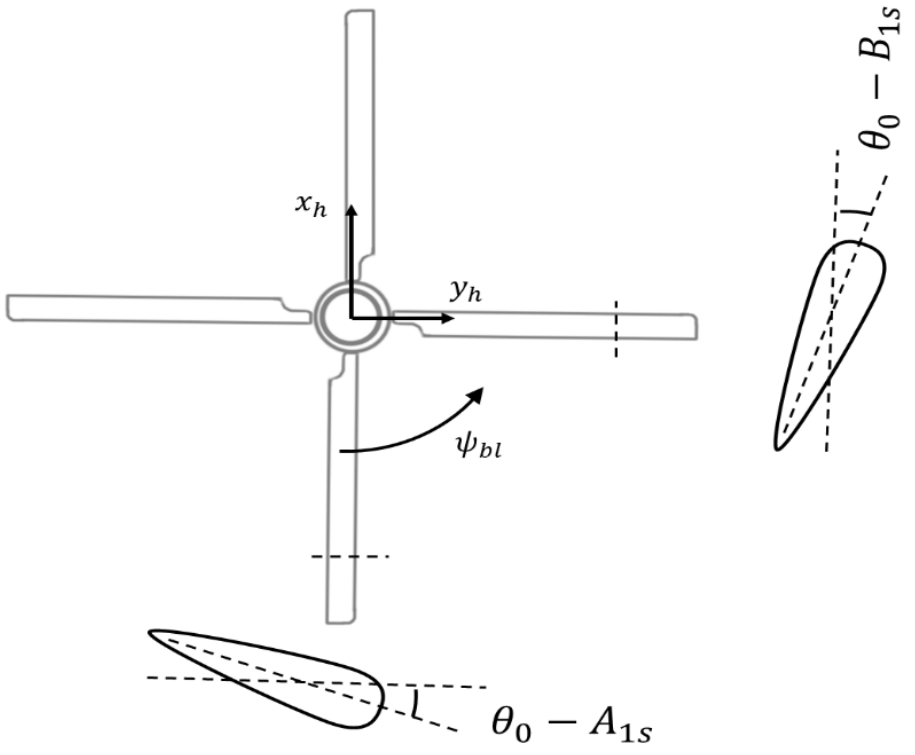

Figure 1.4: Pitch commands at the rotor hub

nominal value by the governor system.

One of the most important characteristics to classify the helicopters is the main rotor hub hinge system. In the case of a fully articulated main rotor system, each rotor blade is attached to the rotor hub through a series of hinges, which allow each blade to move independently of the others. For the case of a full-size helicopter, the flap hinge allows the blade to move in a plane containing the blade and the rotor shaft; the lag hinge allows the blade to move in the plane of rotation; whereas the pitch hinge allows the blade to rotate about its pitch (feathering) axis. Small-scale helicopters rotor hubs typically include a pitch hinge near the shaft and a lead-lag hinge further out, with stiff rubber rings often replacing the flap hinge in a hingeless flap mechanism. For the purpose of helicopter flight dynamics modeling, it is standard practice to model a hingeless rotor (and its flexible blades) as a rotor having rigid blades attached to a virtual hinge, this latter being offset from the main rotor axis. This virtual hinge is often modeled as a torsional spring with its stiffness.

1.3 The autorotation maneuver

Autorotation is the helicopter emergency landing maneuver. It is performed in the case of engine failure and may allow the safe landing of rotorcraft. During the autorotation, the rotor saves its kinetic energy, and its thrust capability, exploiting the impinging flow derived by the descent. In full-scale helicopters the collective pitch is set to its minimum value and, due to the blades washout, the rotor disk preserves a lifting region keeping a controlled descent. This aerodynamic condition is called wind-mill state. When a certain altitude has been reached, approaching

the ground, a proper collective command and a slight positive longitudinal input are used to exploit the residual energy in order to decelerate the vehicle. For manned helicopters, the autorotation is a critical maneuver requiring training and experience for the pilot. Normally, autorotation is not considered for unmanned rotorcrafts; small-scale platforms are equipped with a shut-off system as a safety measure in the case of control and/or power loss.

Nonetheless, for future scenarios related to urban mobility and delivery, where UAVs are supposed to operate over populated areas, the risk of uncontrolled crashes cannot be accepted. As a matter of fact, the use of these systems in a residential environment or in a work/construction site exposes people to health risks. Also, a catastrophic failure of the aircraft may cause an economic damage in the case of the loss of an expensive payload. In this context, the capability of an UAV helicopter to perform the autorotation maneuver becomes a valuable resource for improving its reliability. The problem of manned helicopter autorotation has been widely addressed and a large number of papers can be found in the scientific literature. On the contrary, autorotation for UAVs is relatively a new topic and it's gaining an increasing interest among the control system community. The optimal trajectory to minimize touch-down velocity has been evaluated in Ref. [22] by considering a very simple model of the vertical dynamics of the helicopter. Similar optimal approaches, with a more complex cost functions and dynamics models, have been considered in Ref. [5, 24, 33] whereas in Ref. [43] an optimal trajectory and control system for the tracking have been evaluated. In Ref. [27] the dynamic characteristics of a mixed rotor-wing aircraft during autorotation have been investigated.

Addressing autorotation trajectory design with open loop optimal techniques provides effective solutions but, at the same time, they are strongly affected by initial conditions, disturbances, and model errors. Therefore, the automatic tracking of such trajectories requires online systems to continuously run the optimal algorithm, leading to a large computational burden. Moreover, closed-loop effective tracking is achieved when the reference trajectories are simple functions of a few key measured states, while the optimal solutions are commonly more complex functions. This would introduce the need for simplifying these solutions, going through sub-optimal trajectories. For the purpose of the present work, a simpler approach has been preferred by focusing on the simplicity, robustness, computational cheapness, and in-flight trackability of the reference trajectory.

The autorotation maneuver has been first divided and studied into its main phases, then the design of a suitable nominal maneuver has been conducted and a proper control strategy has been developed to follow the designed pattern online. Finally, several simulations have been done to test the quality and efficiency of the designed maneuver and the control system. The maneuver has also been simulated with an alternative control system based on the nonlinear dynamic inversion technique.

1.4 Introduction on the helicopter control

The continuous development of unmanned aerial systems, and the challenges arising from the new applications, make the theme of control one of the main fields of research. Particular effort is put to increase the agility of these vehicles and, at the

same time, to ensure their safety. The interest in these themes is widespread in the academic as in the industrial field. Several possibilities are offered by scientific literature for controlling helicopters. Most of the techniques are based on nested control logics in which the inner control loop is used to stabilize the attitude dynamics, while the outer loop follows a commanded velocity. The traditional and simplest approach is given by the linear control, namely the use of PID logic. A decoupling is hypothesized and every single axis dynamics is studied considering linearized models. A SISO (single input -single output) model is adopted for the control synthesis. More elaborated models are used in the MIMO (multi input - multi output) approach. in this case, multivariable control theories have been elaborated to take into account the combined dynamic effect of the state variables. Several linear and nonlinear multivariable control techniques have been developed and tested in the last decades. One of the main categories is the Optimal control. Examples of helicopters controlled with Optimal approaches can be found in Ref. [20, 36, 43]. Advanced control techniques are represented by nonlinear control. In nonlinear control, the plant is described by more complex models, and the control system is developed considering its nonlinearities and trying to reduce their effects. The major advantage of nonlinear control, and its main motivation, is related to the possibility of:

- fully exploits the physical capabilities of the aircraft;
- fully exploits the control capabilities (actuators capabilities);
- fully exploits the flight envelope;
- ensures higher robustness of the system to model uncertainties and component

failures

Within the nonlinear control, particular interest has been put, in this thesis, on the nonlinear dynamic inversion control NDI. In this kind of technique, the control action is elaborated by inverting a nonlinear dynamic equation of the system. The inputs from the pilot, or from a navigation system, are given to a reference dynamics which is used to generate reference accelerations. These accelerations are, in turn, used to calculate the control action on the system. The effect is to cancel the nonlinearities of the systems imposing a desired reference dynamics. Several applications of this technique can be found in the full-scale fixed aircraft control [50, 52], for UAVs applications [1, 47], and in the space sector [15, 30].

1.5 Contributions

Objectives of this thesis were the study and design of the automatic autorotation maneuver for a small-scale helicopter and the development of a controller based on nonlinear dynamic inversion. Main contributions are reported in the following:

- the study of the autorotation steady descent conditions has been addressed by solving a trim algorithm that includes the equilibrium around the rotor shaft. The key variables and their role have been highlighted and discussed;
- the design of the flare profile has been conducted considering the implementability for on-board systems as a main requirement;
- the NDI controller for a small-scale helicopter has been developed inverting a medium-order dynamic model;

- An inflow ratio estimation algorithm has been developed using an extended Kalman filter where the fictitious measure is obtained measuring the helicopter accelerations and inverting a reduced order model of the rotor thrust.

1.6 Overview of the thesis

In this section an overview of the chapters contents is given. In chapter 2 the mathematical model for the helicopter dynamics, used for simulations is described. Some brief comment is also given on the several possible modeling accuracy levels and their typical applications. Some physical insight is also given for the main rotor inflow dynamics and flapping dynamics. In chapter 3 the offline design of the autorotation maneuver is performed. In particular, the first phase describes the calculation of the steady descent conditions with a trim algorithm, while the second part is dedicated to the flare profile design and optimization. Chapter 4 reports the classical controllers used for the attitude control and the PID based logic adopted for the automatic autorotation phases. In chapter 5 the NDI controller is described, first giving a brief general introduction and then applying the theory to obtain the attitude and velocity controller. Finally chapter 6 contains the main simulation results.

Chapter 2

Helicopter mathematical model

2.1 Helicopter modeling

The development of mathematical models, capable of describing the most relevant features of flying systems, is a fundamental need in several industrial and research branches of the aerospace sector, especially when a model-based approach is adopted. Depending on the model particular degree of reliability, which is in turn a function of the its complexity and its integration with the vehicle's data, the obtained simulation environment can be used for several tasks: from the flight performance analysis, to the dynamic characterization of the system, until the possibility of a platform for the design and simulation of control systems. The latter use is the main scope of the models implementation done in this work.

From a historical point of view, the development of helicopter models has been based on relatively simple analytical methods until the development of computers. After that, with the increasing computational power of computers and numerical techniques, higher levels of modeling have been developed for the description of flex-

ible blade dynamics and aerodynamic loads. Recent developments have led to full coupling of CFD (computational fluid dynamics) and CSD (computational structure dynamics) methods for the analysis of blade operating conditions, vibrations, and aeroacoustic. Due to their complexity, these kind of model results not suitable for flight mechanics analysis, especially in the first design phases, since their computational costs prevent direct dynamic simulations where fast solutions are required. In the field of flight mechanics and dynamics added application of these models is the validation of lower-order models when flight or wind tunnel data is not available. Besides their computational cheapness, low-order models have also at least two additional advantages: first, the direct relations between system parameters and variables, make these models smart tools to gain physical insight into rotorcraft behavior; second, they result suitable even for the development of control laws, which are usually based on very simple (most of the time linear) models.

Two different strategies are possible in the development of low–order rotorcraft mathematical models: building the models from first–principles (i.e. from physical laws), or identifying the model from flight–data. The identification approach is possible only when the system to be modeled is available or requires the development of large databases based on the design experience of a particular company or group. Limited exceptions to these problems are subsystem models (e.g. engine model) or blade profile or fuselage aerodynamic models. In these cases, data may be available provided that tests were performed for previous use of these components.

In the perspective of a first-principle model, several levels of complexity and accuracy can again be recognized. A wide literature exists on the modeling approaches

and numerical techniques for the analysis of the helicopters performance and dynamics. A simplified static analysis is given in Bramwell [7] which provides also closed formulas for the main rotor aerodynamic forces. Slightly more detailed models are described by Padfield [19], which introduces an equivalent hinge stiffness located at the rotor centre, and Johnson [23], Prouty [39], Arra [2], and Leishman [26] where more extensive use of blade element theory is applied. Particular attention is put on the tip-path-plane (TPP) dynamics and the rotor loads transmitted to the fuselage. Correction factors are also added in these textbooks to improve the model-to-reality performances agreement. Heffley and Minch [21] propose a minimum complexity mathematical model for the flight simulation of conventional helicopters. Flapping dynamics is here described by a first order dynamics for longitudinal and lateral TPP tilt angles, whereas coning is assumed constant. A uniform static inflow is used and rotor inplane forces are determined by thrust tilt only.

In a series of reports, Chen et al. [11, 12, 46] propose a mathematical model for both articulated and teetering rotors. The flapping follows a tip path plane representation, where the flapping angles distribution over the rotor disk is a first-order harmonic series with time-variant coefficients. These coefficients follow a second order linear dynamics. Linear aerodynamics is used to evaluate blade loads so that average rotor force and moment can be evaluated analytically by integrating aerodynamic and inertial loads along the blade span and over one rotor revolution. Static uniform inflow is here used. This latter model, with a slightly more complex inflow representation, has been selected in this work for the helicopter dynamics simulation.

Further complexity is reached in Tamallah [43], where the aerodynamic loads from

the main rotor are obtained by integrating the blade element force over the blade span at every time step. Here lag dynamics and flapping dynamics is considered for every single blade whereas a first-order harmonic series with time-variant coefficients is used to model the inflow ratio over the rotor disk.

The model complexity largely depends on three main points: the dynamics of the rotor, the aerodynamics of the rotor (blades and rotor aerodynamics, inflow, wake models) and the rotor-fuselage interaction. Main level of modellation, for the main rotor, as defined in Ref. [19], are reported in Tab. 2.1.

2.2 Assumptions

The scope of this section is to illustrate the mathematical model used for the dynamic simulation of a hinge-less flybar-less small-scale helicopter, adopted for the development and test of the automatic autorotation maneuver. The selected helicopter model is given by a 11 degrees of freedom non-linear dynamic system. The forces delivered by the rotors are obtained considering linear aerodynamics applied to the blade element theory. Aerodynamic loads on each blade are evaluated according to a simple strip theory with a unitary tip-loss factor, neglecting compressibility and stall effects. Blades are considered rigid and a linear twist θ_t along their span is assumed. An equivalent hinge stiffness K_β is added to consider the rigidity of the hinge-less rotor hub of the typical small-scale helicopter. A simplified model for the ground effect is considered whereas the presence of a reverse flow region is neglected. The forces and moments delivered by the main and tail rotors are obtained in closed formulas by integrating the blade-element loads on the blade span and one revolution

Level 0	Aerodynamics	linear airfoil aerodynamics static uniform inflow with momentum theory analytically averaged aerodynamic loads
	Dynamics	rigid blades, steady-state flapping, multi–blade coordinates
Level 1	Aerodynamics	linear airfoil aerodynamics dynamic inflow with momentum theory analytically integrated aerodynamic loads
	Dynamics	rigid blades featuring: 1) quasi-steady motion 2) flap dynamics 3) flap+lag dynamics 4) flap+lag dynamics and quasi-steady torsion
Level 2	Aerodynamics	nonlinear airfoil aerodynamics with (limited) 3-D effects dynamic inflow with momentum theory local effects of blade–vortex interaction 2-D unsteady aerodynamics and compressibility effects numerically integrated aerodynamic loads
	Dynamics	rigid blades featuring flap+lag dynamics low–order elastic bending and torsional blade models
Level 3	Aerodynamics	nonlinear 3-D aerodynamics with full wake analysis unsteady aerodynamics and compressibility effects numerically integrated aerodynamic loads
	Dynamics	detailed structural representation with elastic modes or finite elements

Table 2.1: Levels of rotor modelling

around the rotor.

The subsystems considered in the evaluation of the moments and forces acting on the system are the main rotors, the tail rotor, and the fuselage. No vertical or horizontal surfaces have been modeled due to the limited effect they have on the flight dynamics of small-scale helicopters. The complete helicopter forces and moments, as the flapping dynamics model, can be found in Ref. [11, 12, 46] whereas the main reference for the inflow model is Ref. [38].

2.3 Reference frames

Under the assumption of rigid helicopter fuselage in motion with respect to a flat, non-rotating Earth, an approximation of an inertial frame is provided by a North-East-Down frame, $\mathbb{F}_e = \{O, x_e, y_e, z_e\}$, centered in an arbitrary point O of the Earth surface, whereas a body-frame $\mathbb{F}_b = \{G, x_b, y_b, z_b\}$ is chosen to represent the motion of the rotorcraft. The origin of $\mathbb{F}_b$ is located in the centre of mass G of the rotorcraft, which also represents its position $OG = r_e = (x_e, y_e, z_e)^T$. Although a helicopter is a non-symmetric vehicle, it is possible to identify a longitudinal plane, with x_b pointing towards the front of the fuselage, z_b perpendicular to x_b in the longitudinal plane, pointing downwards, and y_b, normal to the longitudinal plane, completing a right-handed triad. A local-vertical frame $\mathbb{F}_{lv} = \{G, x_{lv}, y_{lv}, z_{lv}\}$ is also considered for guidance tasks. This frame is equivalent to the NED frame rotated around the z_e axis to follow the vehicle heading.

Other local frames are introduced for the main rotor moments and forces description. In particular, an hub-body frame $\mathbb{F}_h = \{H, x_h, y_h, z_h\}$ is centered to the main

rotor hub H and it is obtained rotating the body frame around the y_b such that z_h follows the rotor shaft direction. The hub-wind frame $\mathbb{F}_{hw} = \{H, x_{hw}, y_{hw}, z_{hw}\}$ is in turn obtained rotating the hub-body frame around the z_h to align x_{hw} to the rotor disk in-plane wind component.

The main matrices for the frame transformations are reported in the following. The trigonometric functions are somewhere abbreviated as $c = \cos$, $s = \sin$, $t = tan$. The symbol i_s it is used for the longitudynal shaft tilt angle, while β_w is the sideslip angle in the rotor disk plane.

body to NED matrix

$$\mathbf{T_{eb}} = \begin{bmatrix} c\,\theta\,c\,\psi & c\,\psi\,s\,\theta\,s\,\phi - c\,\phi\,s\,\psi & s\,\phi\,s\,\psi + c\,\phi\,c\,\psi\,s\,\theta \\ c\,\theta\,s\,\psi & c\,\phi\,c\,\psi + s\,\theta\,s\,\phi\,s\,\psi & c\,\phi\,s\,\theta\,s\,\psi - c\,\psi\,s\,\phi \\ -s\,\theta & c\,\theta\,s\,\phi & c\,\theta\,c\,\phi \end{bmatrix} \tag{2.1}$$

body to local-vertical

$$\mathbf{T_{lv\,b}} = \begin{bmatrix} c\,\theta & s\,\theta\,s\,\phi & c\,\phi\,s\,\theta \\ 0 & c\,\phi & -s\,\phi \\ -s\,\theta & c\,\theta\,s\,\phi & c\,\theta\,c\,\phi \end{bmatrix} \tag{2.2}$$

body to hub-body matrix

$$\mathbf{T_{hb}} = \begin{bmatrix} \cos i_s & 0 & \sin i_s \\ 0 & 1 & 0 \\ -\sin i_s & 0 & \cos i_s \end{bmatrix} \tag{2.3}$$

hub-body to hub-wind matrix

$$\mathbf{T_{hw\,h}} = \begin{bmatrix} \cos \beta_w & \sin \beta_w & 0 \\ -\sin \beta_w & \cos \beta_w & 0 \\ 0 & 0 & 1 \end{bmatrix} \tag{2.4}$$

2.4 State variables and commands

The state and command vectors of the system are reported below:

$$\begin{aligned} x &= [\, r_e;\, V_b;\, \Xi;\, \omega_b;\, a;\, \dot{a};\, \Omega;\, \lambda_i \,] \\ u &= [\, \theta_0;\, A_{1s};\, B_{1s};\, \theta_{tr} \,] \end{aligned}$$

where:

$r_e = [\, x_e;\, y_e;\, z_e \,]$	vehicle position in earth-fixed frame
$V_b = [\, u_b;\, v_b;\, w_b \,]$	velocity in body frame
$\Xi = [\, \phi;\, \theta;\, \psi \,]$	Euler angles
$\omega_b = [\, p;\, q;\, r \,]$	angular rates in body frame
$a = [\, a_0;\, a_1;\, b_1 \,]$	coning, longitudinal and lateral flapping angles
$\dot{a} = \left[\dot{a}_0;\, \dot{a}_1;\, \dot{b}_1 \right]$	coning, longitudinal and lateral flapping angles time derivatives
Ω	main rotor angular rate
λ_i	main rotor induced inflow ratio

and

θ_0	collective pitch
A_{1s}	lateral pitch
B_{1s}	longitudinal pitch
θ_{tr}	tail rotor pitch

The state variables of the system include the global system variables and some important local variables for the main rotor whereas the command vector is made up of main rotor collective, lateral and longitudinal pitch, and tail rotor collective pitch.

2.5 Kinematics equations

The attitude of the rotorcraft is expressed by means of Euler Angles ϕ, θ, ψ which vary in time as a function of ω_b as follows:

$$\begin{pmatrix} \dot{\phi} \\ \dot{\theta} \\ \dot{\psi} \end{pmatrix} = \begin{bmatrix} 1 & \sin\phi\tan\theta & \cos\phi\tan\theta \\ 0 & \cos\phi & -\sin\phi \\ 0 & \frac{\sin\phi}{\cos\theta} & \frac{\cos\phi}{\cos\theta} \end{bmatrix} \begin{pmatrix} p \\ q \\ r \end{pmatrix} \tag{2.5}$$

or in a contracted form:

$$\dot{\Xi} = \mathbf{R}\,\omega_b$$

The velocities in NED frame are written as function of Euler angles and velocities in body frame:

$$\begin{pmatrix} \dot{x}_e \\ \dot{y}_e \\ \dot{z}_e \end{pmatrix} = \begin{bmatrix} c\,\theta\,c\,\psi & c\,\psi\,s\,\theta\,s\,\phi - c\,\phi\,s\,\psi & s\,\phi\,s\,\psi + c\,\phi\,c\,\psi\,s\,\theta \\ c\,\theta\,s\,\psi & c\,\phi\,c\,\psi + s\,\theta\,s\,\phi\,s\,\psi & c\,\phi\,s\,\theta\,s\,\psi - c\,\psi\,s\,\phi \\ -s\,\theta & c\,\theta\,s\,\phi & c\,\theta\,c\,\phi \end{bmatrix} \begin{pmatrix} u_b \\ v_b \\ w_b \end{pmatrix} \tag{2.6}$$

or contracted

$$\dot{r}_e = \mathbf{T_{eb}} V_b$$

2.6 Translational and Rotational dynamics

The helicopter equations of motion are obatined under the hypothesis of rigid body:

$$\dot{V}_b = \frac{F_b - \omega \times V_b}{m} \tag{2.7}$$

$$\dot{\omega}_b = I^{-1}(M_b - \omega_b \times I\omega_b) \tag{2.8}$$

The total moment and force are given summing up all the contributions of the helicopter subsystems, namely the main rotor, tail rotor and fuselage:

$$F_b = F_{b,mr} + F_{b,tr} + F_{b,f} + W_b \tag{2.9}$$

$$M_b = M_{b,mr} + M_{b,tr} + M_{b,f} \tag{2.10}$$

The weight force W_b in the body frame is reported below:

$$W_b = m\,g \begin{pmatrix} -\sin\theta \\ \sin\phi\cos\theta \\ \cos\phi\cos\theta \end{pmatrix} \tag{2.11}$$

Detailed expressions of other components can be found in the following subsections. Complete derivation of the subsystems forces and moments is reported in Ref. [11, 46]

2.6.1 Clockswise correction factor for main rotor and tail rotor models

Main helicopter model adopted in this work has been developed in Ref. [11, 12, 46]. These works considered only counter-clockwise rotors. A correction factor χ is here introduced according to Ref. [13] for the case of clockwise rotors. In particular, the

following matrices Π_1 and Π_2 will be found in the following sections:

$$\Pi_1 = \begin{pmatrix} 1 & 0 & 0 \\ 0 & \chi & 0 \\ 0 & 0 & 1 \end{pmatrix} \tag{2.12}$$

$$\Pi_2 = \begin{pmatrix} \chi & 0 & 0 \\ 0 & 1 & 0 \\ 0 & 0 & \chi \end{pmatrix} \tag{2.13}$$

where $\chi = 1$ for the counter-clockwise rotor and $\chi = -1$ for the clockwise rotor.

2.6.2 Main rotor moments and forces

The total air velocity hitting the helicopter, written in body axes is given by:

$$V_b^{air} = V_b - T_{be}\, V_w \tag{2.14}$$

where V_w is the wind velocity with respect to the ground in NED frame. Transforming V_b^{air} in the hub-body frame it is possible to obtain the air velocity needed for the calculation of the main rotor aerodynamic forces:

$$V_h = \Pi_1 \left(T_{hb} \left(V_b^{air} + \omega_b \times GH \right) \right) = [\, u_h; v_h; w_h \,] \tag{2.15}$$

where $GH = r_h$ is the hub position vector in the body frame. Also the angular rate can be written in the hub system:

$$\omega_h = \Pi_2 \left(T_{hb}\, \omega_b \right) = \left[\, p_h; q_h; r_h \, \right] \tag{2.16}$$

We also define the advance ratio μ and the inflow ratio λ as:

$$\mu = \frac{\sqrt{u_h^2 + v_h^2}}{\Omega\, R} \tag{2.17}$$

$$\lambda = \frac{w_h - v_i}{\Omega\, R} = \mu_z - \lambda_{i,0} \tag{2.18}$$

where v_i is the mean induced velocity of the rotor. The local sideslip β_w and the rotor wake angle χ are instead defined as:

$$\beta_w = \arctan \frac{v_h}{u_h} \tag{2.19}$$

$$\chi = \arctan \frac{\mu}{\lambda} \tag{2.20}$$

The main rotor presents three main active aerodynamic forces: the thrust T, the horizontal rotor drag force H (opposite to x_h when the helicopter advances) and the

lateral force Y. Their expression in the hub-wind reference frame are:

$$\begin{aligned} T =& \frac{1}{2} N_b \, \rho \, C_{l_\alpha} \, c \, R \, (\Omega \, R)^2 \left\{ \frac{1}{2} \left(1 - \varepsilon^2\right) \lambda + \theta_0 \left[\frac{1}{3} + \frac{\mu^2}{2} \left(1 - \varepsilon\right) \right] + \theta_t \left(\frac{1}{4} + \frac{\mu^2}{4} \left(1 - \varepsilon^2\right) \right) \right. \\ & - \frac{\mu}{2} \left(1 - \varepsilon^2\right) \left(B_{1c} - K_1 \, b_1\right) - a_0 \left[\frac{1}{3} + \frac{\mu^2}{2} \left(1 - \varepsilon\right) \right] K_1 + a_1 \, \frac{\mu}{2} \, \varepsilon \left(1 - \varepsilon\right) - \frac{\dot{a}_0}{\Omega} \left(\frac{1}{3} - \frac{\varepsilon}{2} \right) \\ & \left. + \frac{\dot{b}_1}{\Omega} \, \frac{\mu}{4} \left(1 - \varepsilon\right)^2 + \frac{\mu}{4} \left(1 - \varepsilon^2\right) \left(\frac{p_h}{\Omega} \cos \beta_w + \frac{q_h}{\Omega} \sin \beta_w \right) \right\} - N_b \frac{M_b}{g} \, \ddot{a}_0 \end{aligned} \tag{2.21}$$

$$C_T = \frac{T}{\rho \pi R^4 \Omega^2} \tag{2.22}$$

$$
\begin{aligned}
H_w = \frac{1}{2}\, N_b\, \rho\, C_{l_\alpha}\, c\, R\, (\Omega\, R)^2 \left\{ \frac{\delta\, \mu}{2\, C_{l_\alpha}}\, \left(1-\varepsilon^2\right) - \frac{1}{4}\, (\theta_0 - K_1\, a_0)\, \left[2\, \lambda\, \mu\, (1-\varepsilon) - \mu\, (1-\varepsilon)^2\, \frac{\dot{a}_0}{\Omega} \right.\right. \\
\left. - \left(\varepsilon - \frac{2}{3}\right)\, \left(\frac{\dot{b}_1}{\Omega} - a_1\right) - \frac{2}{3}\, a_1 + \frac{2}{3}\, \left(\frac{p_H}{\Omega}\, \cos\beta_w + \frac{q_H}{\Omega}\, \sin\beta_w\right) \right] \\
- \frac{\theta_t}{4}\, \left[\mu\, \lambda\, \left(1-\varepsilon^2\right) + \frac{\dot{a}_0}{\Omega}\, \mu\, \left(\varepsilon - \frac{2}{3}\right) - 2\, \left(\frac{\varepsilon}{3} - \frac{1}{4}\right)\, \left(\frac{\dot{b}_1}{\Omega} - a_1\right) - \frac{a_1}{2} \right. \\
\left. + \frac{1}{2}\, \left(\frac{p_H}{\Omega}\, \cos\beta_w + \frac{q_H}{\Omega}\, \sin\beta_w\right) \right] + \frac{1}{4}\, (A_{1c} - K_1\, a_1)\, \left[-b_1\, \frac{\mu}{4}\, \left(1-\varepsilon^2\right) \right. \\
\left. + \frac{1}{4}\, \mu\, (1-\varepsilon)^2\, \left(\frac{\dot{a}_1}{\Omega} + b_1\right) + \frac{2}{3}\, a_0 + \frac{\mu}{4}\, \left(1-\varepsilon^2\right)\, \left(-\frac{p_H}{\Omega} \sin\beta_w + \frac{q_H}{\Omega} \cos\beta_w\right) \right] \\
+ \frac{1}{4}\, (B_{1c} - K_1\, b_1)\, \left[\frac{3}{4}\, \mu\, (1-\varepsilon)^2\, \left(\frac{\dot{b}_1}{\Omega} - a_1\right) + \left(1-\varepsilon^2\right)\, \left(\lambda - a_1\, \frac{\mu}{4}\right) + \left(\varepsilon - \frac{2}{3}\right)\, \frac{\dot{a}_0}{\Omega} \right. \\
\left. + \frac{3}{4}\mu\, \left(1-\varepsilon^2\right)\, \left(\frac{p_H}{\Omega}\, \cos\beta_w + \frac{q_H}{\Omega}\, \sin\beta_w\right) \right] + \left[\frac{1}{4}\, \left(\varepsilon\, (1-\varepsilon)\, \left(\frac{\dot{b}_1}{\Omega} - a_1\right)\, 4\, \lambda \right. \right. \\
\left. - \left(1-\varepsilon^2\right)\, \left(2\, \lambda\, \left(\frac{\dot{b}1}{\Omega} - a_1\right) - a_1\, \lambda\right) - \left(\frac{2}{3} - \varepsilon\right)\, \left(a_1\, \frac{\dot{a}_0}{\Omega} + a_0\, \left(\frac{\dot{a}_1}{\Omega} + b_1\right)\right) \right) \\
- \frac{2}{3}\, a_0\, \left(-\frac{p_H}{\Omega}\, \sin\beta_w + \frac{q_H}{\Omega}\, \cos\beta_w\right) - \left(2\, \left(1-\varepsilon^2\right)\, \lambda - 4\, \left(\frac{1}{3} - \frac{\varepsilon}{2}\right)\, \frac{\dot{a}_0}{\Omega}\right)\, \left(\frac{p_H}{\Omega}\, \cos\beta_w \right. \\
\left. + \frac{q_H}{\Omega}\, \sin\beta_w\right) + 4\, \frac{\dot{a}_0}{\Omega}\, \left(\frac{\dot{b}_1}{\Omega} - a_1\right)\, \left(\frac{1}{3} - \varepsilon + \varepsilon^2\right) \Bigg] + \frac{\mu}{4}\, \left[\varepsilon\, (1-\varepsilon)\, \left(a_1\, \left(\frac{\dot{b}_1}{\Omega} - a_1\right) \right. \right. \\
\left. \left. + b_1\, \left(\frac{\dot{a}_1}{\Omega} + b_1\right)\right) + \frac{1}{4}\, (1-\varepsilon)^2\, \left(b_1\, \left(\frac{\dot{a}_1}{\Omega} + b_1\right) + a_1\, \left(\frac{\dot{b}_1}{\Omega} - a_1\right)\right) \right. \\
- \frac{1}{2}\, \left(1-\varepsilon^2\right)\, \left(a_1\, \left(\frac{\dot{b}_1}{\Omega} - a_1\right) + b_1\, \left(\frac{\dot{a}_1}{\Omega} + b_1\right) - 2\, a_0^2 - \frac{b_1^2}{2} - \frac{3}{2}\, a_1^2\right) \\
\left. \left. - \frac{a_1}{4}\, \left(1-\varepsilon^2\right)\, \left(\frac{p_H}{\Omega}\, \cos\beta_w + \frac{q_H}{\Omega}\, \sin\beta_w\right) - \frac{b_1}{4}\, \left(1-\varepsilon^2\right)\, \left(-\frac{p_H}{\Omega}\, \sin\beta_w + \frac{q_H}{\Omega}\, \cos\beta_w\right) \right] \right\}
\end{aligned}
\tag{2.23}
$$

$$
\begin{aligned}
Y_w = \frac{1}{2} N_b \rho C_{l_\alpha} c R (\Omega R)^2 \Bigg\{ & -\frac{1}{4}(\theta_0 - K_1 a_0) \left[\left(\left(\varepsilon - \frac{2}{3} \right) \left(\frac{\dot{a}_1}{\Omega} + b_1 \right) - \frac{2}{3} b_1 \right) + 3 a_0 \left(1 - \varepsilon^2\right) \mu \right. \\
& \left. -2 b_1 (1 - \varepsilon) \mu^2 - \frac{2}{3} \left(-\frac{p_H}{\Omega} \sin\beta_w + \frac{q_H}{\Omega} \cos\beta_w \right) \right] - \frac{\theta_t}{4} \left[\left(\left(\frac{2}{3}\varepsilon - \frac{1}{2} \right) \left(\frac{\dot{a}_1}{\Omega} + b_1 \right) - \frac{b_1}{2} \right) \right. \\
& \left. +2 a_0 \mu - b_1 \left(1 - \varepsilon^2\right) \mu^2 - \frac{1}{2} \left(-\frac{p_H}{\Omega} \sin\beta_w + \frac{q_H}{\Omega} \cos\beta_w \right) \right] \\
& - \frac{1}{4} (A_{1c} - K_1 a_1) \left[\left(\left(\varepsilon - \frac{2}{3} \right) \frac{\dot{a}_0}{\Omega} + \lambda \left(1 - \varepsilon^2\right) \right) + \mu \left(\frac{5}{4} a_1 \left(1 - \varepsilon^2\right) \right. \right. \\
& \left. \left. + \frac{1}{4} (1 - \varepsilon)^2 \left(\frac{\dot{b}_1}{\Omega} - a_1 \right) \right) + \frac{\mu}{4} \left(1 - \varepsilon^2\right) \left(\frac{p_H}{\Omega} \cos\beta_w + \frac{q_H}{\Omega} \sin\beta_w \right) \right] \\
& - \frac{1}{4} (B_{1c} - K_1 b_1) \left[-\frac{2}{3} a_0 + \mu \left(\frac{7}{4} b_1 \left(1 - \varepsilon^2\right) + \frac{1}{4} (1 - \varepsilon)^2 \left(\frac{\dot{a}_1}{\Omega} + b_1 \right) \right) \right. \\
& \left. + \frac{1}{4} \left(-\frac{p_H}{\Omega} \sin\beta_w + \frac{q_H}{\Omega} \cos\beta_w \right) - \mu^2 \left(2 a_0 (1 - \varepsilon)\right) \right] \\
& - \frac{1}{4} \left[4 \left(\frac{1}{3} - \varepsilon + \varepsilon^2 \right) \frac{\dot{a}_0}{\Omega} \left(\frac{\dot{a}_1}{\Omega} + b_1 \right) - 2 \lambda (1 - \varepsilon)^2 \left(\frac{\dot{a}_1}{\Omega} + b_1 \right) \right. \\
& + \frac{2}{3} a_0 \left(\frac{p_H}{\Omega} \cos\beta_w + \frac{q_H}{\Omega} \sin\beta_w \right) + 2 a_0 \left(\frac{1}{3} - \frac{\varepsilon}{2} \right) \left(\frac{\dot{b}_1}{\Omega} - a_1 \right) - 2 b_1 \left(\frac{\lambda}{2} \left(1 - \varepsilon^2\right) \right. \\
& \left. \left. - \frac{\dot{a}_0}{\Omega} \left(\frac{1}{3} - \frac{\varepsilon}{2} \right) \right) + \left(4 \left(\frac{1}{3} - \frac{\varepsilon}{2} \right) \frac{\dot{a}_0}{\Omega} - 2 \left(1 - \varepsilon^2\right) \lambda \right) \left(-\frac{p_H}{\Omega} \sin\beta_w + \frac{q_H}{\Omega} \cos\beta_w \right) \right] \\
& - \frac{\mu}{4} \left[6 a_0 \lambda (1 - \varepsilon) - a_1 \frac{b_1}{2} \left(1 - \varepsilon^2\right) - 3 (1 - \varepsilon)^2 a_0 \frac{\dot{a}_0}{\Omega} \right. \\
& - \frac{7}{4} (1 - \varepsilon)^2 a_1 \left(\frac{\dot{a}_1}{\Omega} + b_1 \right) - \frac{5}{4} b_1 \left(1 - \varepsilon^2\right) \left(\frac{p_H}{\Omega} \cos\beta_w + \frac{q_H}{\Omega} \sin\beta_w \right) + \\
& \left. \left. - \frac{7}{4} a_1 \left(1 - \varepsilon^2\right) \left(-\frac{p_H}{\Omega} \sin\beta_w + \frac{q_H}{\Omega} \cos\beta_w \right) - \frac{5}{4} (1 - \varepsilon)^2 b_1 \left(\frac{\dot{b}_1}{\Omega} - a_1 \right) \right] - \mu^2 \left[a_0 a_1 (1 - \varepsilon) \right] \right\}
\end{aligned}
\tag{2.24}
$$

The aerodynamic moments around the hub, in the hub-wind axis are:

$$M_w = \frac{N_b}{2}\left[K_\beta\, a_1 - \frac{e\, M_\beta}{g}\left(\ddot{a}_1 + 2\,\dot{b}_1\,\Omega - a_1\,\Omega^2\right)\right] - \frac{N_b}{2}\, I_\beta\,\Omega^2\,\gamma\,\varepsilon\left\{\left[-\frac{1}{6} + \frac{\mu^2}{8}\,(1-\varepsilon)\right](A_{1c} - K_1\, a_1)\right.$$
$$\left. -\frac{\mu}{4}\left(1-\varepsilon^2\right)\, a_0 + \frac{\mu^2}{8}\,(1-\varepsilon)\, b_1 + \left(\frac{1}{6} - \frac{\varepsilon}{4}\right)\left(\frac{\dot{a}_1}{\Omega} + b_1\right) + \frac{1}{6}\left(-\frac{p_H}{\Omega}\,\sin\beta_w + \frac{q_H}{\Omega}\,\cos\beta_w\right)\right\} \tag{2.25}$$

$$L_w = \frac{N_b}{2}\left[K_\beta\, b_1 - \frac{e\, M_\beta}{g}\left(\ddot{b}_1 - 2\,\dot{a}_1\,\Omega - b_1\,\Omega^2\right)\right] - \frac{N_b}{2}\, I_\beta\,\Omega^2\,\gamma\,\varepsilon\left\{\frac{\mu}{2}\left(1-\varepsilon^2\right)\,(\theta_0 - K_1\, a_0)\right.$$
$$-\left[\frac{1}{6} + \frac{3}{8}\,\mu^2\,(1-\varepsilon)\right](B_{1c} - K_1\, b_1) + \frac{\mu}{3}\,\theta_t + \frac{\mu}{2}\,(1-\varepsilon)\,\lambda + \frac{\mu^2}{8}\,(1-\varepsilon)\, a_1$$
$$\left. -\frac{\mu}{4}\,(1-\varepsilon)^2\,\frac{\dot{a}_0}{\Omega} + \left(\frac{1}{6} - \frac{\varepsilon}{4}\right)\left(\frac{\dot{b}_1}{\Omega} - a_1\right) + \frac{1}{6}\left(\frac{p_H}{\Omega}\,\cos\beta_w + \frac{q_H}{\Omega}\,\sin\beta_w\right)\right\} \tag{2.26}$$

$$
\begin{aligned}
Q = \frac{N_b}{2}\,\rho\,C_{l_\alpha}\,c\,R^2\,(\Omega\,R)^2 \Bigg\{ & \frac{\delta}{4\,C_{l_\alpha}}\,\left[1+\left(1-\varepsilon^2\right)\,\mu^2\right] - (\theta_0 - K_1\,a_0)\,\left[\frac{\lambda}{3}+\left(\frac{\varepsilon}{3}-\frac{1}{4}\right)\,\frac{\dot{a}_0}{\Omega}+\frac{\mu}{6}\,\frac{\dot{b}_1}{\Omega}\right. \\
& \left. -\frac{\mu\varepsilon}{4}\,\left(\frac{\dot{b}_1}{\Omega}-a_1\right)+\frac{\mu}{6}\,\left(\frac{p_H}{\Omega}\,\cos\beta_w+\frac{q_H}{\Omega}\,\sin\beta_w\right)\right] + (A_{1c}-K_1\,a_1)\,\left[\left(\frac{1}{8}-\frac{\varepsilon}{6}\right)\,\left(\frac{\dot{a}_1}{\Omega}+b_1\right)\right. \\
& \left. -\frac{\mu}{6}\,a_0+\frac{b_1}{16}\,\left(1-\varepsilon^2\right)\,\mu^2+\frac{1}{8}\,\left(-\frac{p_H}{\Omega}\,\sin\beta_w+\frac{q_H}{\Omega}\,\cos\beta_w\right)\right] \\
& + (B_{1c}-K_1\,b_1)\,\left[\left(\frac{1}{8}-\frac{\varepsilon}{6}\right)\,\left(\frac{\dot{b}_1}{\Omega}-a_1\right)+\left(\frac{\varepsilon}{4}-\frac{1}{6}\right)\,\mu\,\frac{\dot{a}_0}{\Omega}+\frac{1}{2}\,\left(1-\varepsilon^2\right)\,\left(\mu\,\frac{\lambda}{2}+\frac{a_1}{8}\,\mu^2\right)\right. \\
& \left. +\frac{1}{8}\,\left(\frac{p_H}{\Omega}\,\cos\beta_w+\frac{q_H}{\Omega}\,\sin\beta_w\right)\right] - \theta_t\,\left[\frac{\lambda}{4}+\left(\frac{\varepsilon}{4}-\frac{1}{5}\right)\,\frac{\dot{a}_0}{\Omega}+\frac{\mu}{8}\,\frac{\dot{b}_1}{\Omega}-\frac{\varepsilon\mu}{6}\,\left(\frac{\dot{b}_1}{\Omega}-a_1\right)\right] \\
& -\frac{1}{2}\,\left(1-\varepsilon^2\right)\,\left[\lambda^2+\lambda\,\mu\,a_1+2\,\lambda\,\varepsilon\,\frac{\dot{a}_0}{\Omega}+\mu\,\varepsilon\,\left(a_1\,\frac{\dot{a}_0}{\Omega}+a_0\,\left(\frac{\dot{a}_1}{\Omega}+b_1\right)\right)\right. \\
& \left. +\mu^2\,\left(\frac{a_0^2}{2}+\frac{3}{8}\,a_1^2+\frac{b_1^2}{8}\right)\right] + \frac{\mu}{3}\,\left[a_1\,\left(\frac{\dot{a}_0}{\Omega}\right)+a_0\,\left(\frac{\dot{a}_1}{\Omega}+b_1\right)\right] + \frac{2}{3}\,\lambda\,\left(\frac{\dot{a}_0}{\Omega}\right) \\
& -\left[-\frac{\mu}{3}\,a_0+\left(\frac{1}{4}-\frac{\varepsilon}{3}\right)\,\left(\frac{\dot{a}_1}{\Omega}+b_1\right)\right]\,\left(-\frac{p_H}{\Omega}\,\sin\beta_w+\frac{q_H}{\Omega}\,\cos\beta_w\right) \\
& -\left(\frac{1}{4}-\frac{\varepsilon}{3}\right)\,\left(\frac{\dot{b}_1}{\Omega}-a_1\right)\,\left(\frac{p_H}{\Omega}\,\cos\beta_w+\frac{q_H}{\Omega}\,\sin\beta_w\right) - \frac{1}{8}\,\left(-\frac{p_H}{\Omega}\,\sin\beta_w+\frac{q_H}{\Omega}\,\cos\beta_w\right)^2 \\
& -\frac{1}{8}\,\left(\frac{p_H}{\Omega}\,\cos\beta_w+\frac{q_H}{\Omega}\,\sin\beta_w\right)^2 - \left(\frac{1}{4}-\frac{2}{3}\,\varepsilon+\frac{\varepsilon^2}{2}\right)\,\left[\left(\frac{\dot{a}_0}{\Omega}\right)^2+\frac{1}{2}\,\left(\left(\frac{\dot{a}_1}{\Omega}+b_1\right)^2+\left(\frac{\dot{b}_1}{\Omega}-a_1\right)^2\right)\right]\Bigg\}
\end{aligned}
\tag{2.27}
$$

In the latter expression the equivalent rotor drag coefficient δ is introduced. It can be evaluated as:

$$\delta = 0.009 + 0.3\,\left(\frac{6\,C_T}{C_{l_\alpha}\,\sigma}\right)^2$$

The terms a_0, a_1, b_1 and their time derivatives $\dot{a}_0$, $\dot{a}_1$, $\dot{b}_1$ refer to the flapping coeffi-

cients. Flapping dynamics is detailed in section 2.7.

The longitudinal and lateral pitch appear in the aerodynamic forces in hub-wind coordinates:

$$A_{1c} = \chi A_{1s} \cos\beta_w - B_{1s} \sin\beta_w \tag{2.28}$$

$$B_{1c} = \chi A_{1s} \sin\beta_w + B_{1s} \cos\beta_w \tag{2.29}$$

To obtain the main rotor forces and moments in the body axis reference frame, starting from the previous results, three transformations need to be done:

- rotation from the hub-wind to the hub-body frame
- rotation from the hub-body to the body frame
- transport moments from the hub-body to the body frame

Forces and moments in the hub-wind frame are:

$$F_{hw} = [-H_w \quad Y_w \quad -T]^t \tag{2.30}$$

$$M_{hw} = [L_w \quad M_w \quad -\xi Q]^t \tag{2.31}$$

where ξ is the free-wheel coefficient which is null during autorotation and 1 during the normal flight. It is added to takes into account that, thanks to the free wheel mechanism no aerodynamic torque is discharged on the fuselage when the engine is

slower than the rotor. Main rotor forces and moments in the body frame are then:

$$F_{b,mr} = \Pi_1 \, T_{bh} \, T_{hw} \, F_{hw} \tag{2.32}$$

$$M_{b,mr} = \Pi_2 \, T_{bh} \, T_{hw} \, M_{hw} + M_{GH} \, F_{b,mr} \tag{2.33}$$

where the transformation matrices have already been defined in section 2.3 and

$$M_{GH} = \begin{bmatrix} 0 & -z_h & y_h \\ z_h & 0 & -x_h \\ -y_h & x_h & 0 \end{bmatrix} \tag{2.34}$$

2.6.3 Tail rotor moments and forces

The air velocity hitting the tail rotor is

$$V_{tr} = \Pi_1 \left(V_b^{air} + \omega_b \times GH_{tr} \right) = [\, u_{tr}; v_{tr}; w_{tr} \,] \tag{2.35}$$

where $GH_{tr} = r_{tr}$ is the tail rotor position in the body frame. The tail rotor advance ratio μ_{tr} and the inflow ratio $\lambda_t r$ are defined as:

$$\mu_{tr} = \frac{\sqrt{u_h^2 + w_h^2}}{\Omega_{tr} \, R_{tr}} \tag{2.36}$$

$$\lambda_{tr} = \frac{-v_{tr} - v_{i,tr}}{\Omega_{tr} \, R_{tr}} \tag{2.37}$$

The local sideslip angle is intead:

$$\beta_{tr} = \arctan \frac{w_{tr}}{u_{tr}} \tag{2.38}$$

We also define:

$$p_{tr} = \chi \left(p \, \cos \beta_{tr} + r \, \sin \beta_{tr} \right) \tag{2.39}$$

$$q_{tr} = \chi \left(r \, \cos \beta_{tr} - p \, \sin \beta_{tr} \right) \tag{2.40}$$

The flapping angles, which are static variables in the case of the tail rotor, can now be evaluated as:

$$a_{1,tr} = \frac{1}{\Delta_{tr}} \left[K_{1,tr} \left(1 + \frac{3}{2} \mu_{tr}^2 \right) f_{1,tr} - \left(1 + \frac{\mu_{tr}^2}{2} \right) f_{2,tr} \right] \tag{2.41}$$

$$b_{1,tr} = \frac{1}{\Delta_{tr}} \left[\left(1 - \frac{\mu_{tr}^2}{2} \right) f_{1,tr} + K_{1,tr} \left(1 + \frac{\mu_{tr}^2}{2} \right) f_{2,tr} \right] \tag{2.42}$$

where we have:

$$\Delta_{tr} = 1 - \frac{\mu_{tr}^4}{4} + K_{1,tr}^2 \left(1 + \frac{\mu_{tr}^2}{2} \right) \left(1 + \frac{3}{2} \mu_{tr}^2 \right) \tag{2.43}$$

$$f_{1,tr} = \frac{4}{3} \mu_{tr} \, a_{0,tr} - \frac{16}{\gamma_{tr} \, \Omega_{tr}} \, p_{tr} - \frac{q_{tr}}{\Omega_{tr}} \tag{2.44}$$

$$f_{2,tr} = \frac{8}{3} K_{1,tr} \, \mu_{tr} \, a_{0,tr} + \frac{16}{\gamma_{tr} \, \Omega_{tr}} \, q_{tr} - \mu_{tr} \left(\frac{8}{3} \, \theta_{tR} + 2 \, \theta_{t,tr} + 2 \, \lambda_{tr} - \frac{p_{tr}}{\Omega_{tr}} \right) \tag{2.45}$$

The tail rotor thrust and the thrust coefficient are:

$$T_{tr} = \rho\, Cl_{\alpha,tr}\, c_{tr}\, R_{tr}\, \left(\Omega_{tr}\, R_{tr}\right)^2 \left\{ \frac{\lambda_{tr}}{2} + \theta_{tr} \left(\frac{1}{3} + \frac{\mu_{tr}^2}{2}\right) + \frac{\theta_{t,tr}}{4}\, \left(1 + \mu_{tr}^2\right) + \mu_{tr}\, \frac{K_{1,tr}}{2}\, b_{1,tr} \right.$$
$$\left. - a_{0,tr} \left(\frac{1}{3} + \frac{\mu_{tr}^2}{2}\right) K_{1,tr} + \frac{\mu_{tr}}{4}\, \frac{p_{tr}}{\Omega_{tr}} \right\} \tag{2.46}$$

$$C_{t,tr} = \frac{T_{tr}}{\rho\, \pi\, R_{tr}^2\, \left(\Omega_{tr}\, R_{tr}\right)^2} \tag{2.47}$$

They depend on the inflow ratio λ_{tr} which is again a function of $C_{t,tr}$

$$\lambda_{tr} = -\frac{v_{tr}}{\Omega_{tr}\, R_{tr}} + \frac{C_{t,tr}}{2\, \sqrt{\mu_{tr}^2 + \lambda_{tr}^2}} \tag{2.48}$$

To obtain both the thrust and the inflow ratio a numeric iterative procedure need to be implemented. The horizontal and lateral forces in the tail rotor hub-wind axes are:

$$H_{w,tr} = \rho\, Cl_{\alpha,tr}\, c_{tr}\, R_{tr}\, \left(\Omega_{tr}\, R_{tr}\right)^2 \left\{ \frac{\delta_{tr}\, \mu_{tr}}{2\, Cl_{\alpha,tr}} - \frac{1}{4}\, \left(\theta_{tr} - K_{1,tr}\, a_{0,tr}\right) \left(2\, \lambda_{tr}\, \mu_{tr} - \frac{4}{3}\, a_{1,tr}\right) \right.$$
$$- \frac{\theta_{t,tr}}{4}\, \left(\mu_{tr}\, \lambda_{tr} - a_{1,tr}\right) - \frac{1}{4}\, K_{1,tr} \left[\frac{2}{3}\, a_{0,tr}\, a_{1,tr} + b_{1,tr}\, \left(\lambda_{tr} - a_{1,tr}\, \mu_{tr}\right)\right]$$
$$+ \frac{3}{4}\, \lambda_{tr}\, a_{1,tr} - a_{0,tr}\, \frac{b_{1,tr}}{6} + \frac{\mu_{tr}}{4}\, \left(a_{0,tr}^2 + a_{1,tr}^2\right)$$
$$- \left[\frac{1}{6}\, \left(\theta_{tr} - K_{1,tr}\, a_{0,tr}\right) + \frac{\theta_{t,tr}}{8} + \frac{3}{16}\, K_{1,tr}\, b_{1,tr}\, \mu_{tr} + \frac{\lambda_{tr}}{2} + a_{1,tr}\, \frac{\mu_{tr}}{16}\right]\, \frac{p_{tr}}{\Omega_{tr}}$$
$$\left. - \left[\frac{1}{16}\, K_{1,tr}\, a_{1,tr}\, \mu_{tr} + \frac{a_{0,tr}}{6} + b_{1,tr}\, \frac{\mu_{tr}}{16}\right]\, \frac{q_{tr}}{\Omega_{tr}} \right\} \tag{2.49}$$

$$
\begin{aligned}
Y_{w,tr} = \rho\, Cl_{\alpha,tr}\, c_{tr}\, R_{tr}\, (\Omega_{tr}\, R_{tr})^2 \left\{ -\frac{1}{4}\, (\theta_{tr} - K_{1,tr}\, a_{0,tr}) \left(-\frac{4}{3}\, b_{1,tr} + 3\, a_{0,tr}\, \mu_{tr} - 2\, b_{1,tr}\, \mu_{tr}^2 \right) \right. \\
- \frac{\theta_{t,tr}}{4}\, \left(-b_{1,tr} + 2\, a_{0,tr}\, \mu_{tr} - b_{1,tr}\, \mu_{tr}^2 \right) + \frac{K_{1,tr}}{4}\, \left[a_{1,tr}\, (\lambda_{tr} + a_{1,tr}\, \mu_{tr}) \right. \\
\left. \left. + b_{1,tr} \left(-\frac{2}{3}\, a_{0,tr} + 2\, b_{1,tr}\, \mu_{tr} - 2\, a_{0,tr}\, \mu_{tr}^2 \right) \right] + \frac{3}{4}\, b_{1,tr}\, \lambda_{tr} + \frac{1}{6}\, a_{0,tr}\, a_{1,tr} \right. \\
- \frac{\mu_{tr}}{4}\, (6\, a_{0,tr}\, \lambda_{tr} - a_{1,tr}\, b_{1,tr}) - \mu_{tr}^2\, a_{0,tr}\, a_{1,tr} + \left(\frac{1}{16}\, K_{1,tr}\, a_{1,tr}\, \mu_{tr} - \frac{a_{0,tr}}{6} \right. \\
\left. \left. + \frac{5}{16}\, b_{1,tr}\, \mu_{tr} \right)\, \frac{p_{tr}}{\Omega_{tr}} + \left[\frac{1}{6}\, (\theta_{tr} - K_{1,tr}\, a_{0,tr}) + \frac{\theta_{t,tr}}{8} + \frac{1}{16}\, K_{1,tr}\, b_{1,tr}\, \mu_{tr} \right. \right. \\
\left. \left. + \frac{1}{2}\, \lambda_{tr} + \frac{7}{16}\, a_{1,tr}\, \mu_{tr} \right]\, \frac{q_{tr}}{\Omega_{tr}} \right\}
\end{aligned}
\tag{2.50}
$$

The tail rotor torque is

$$
\begin{aligned}
Q_{tr} = \rho\, Cl_{\alpha,tr}\, c_{tr}\, R_{tr}^2\, (\Omega_{tr}\, R_{tr})^2 \left\{ \frac{\delta_{tr}}{4\, Cl_{\alpha,tr}}\, \left(1 + \mu_{tr}^2 \right) - \frac{\lambda_{tr}}{3}\, (\theta_{tr} - K_{1,tr}\, a_{0,tr}) - \theta_{t,tr}\, \frac{\lambda_{tr}}{4} + \right. \\
- K_{1,tr} \left[a_{1,tr} \left(\frac{b_{1,tr}}{8} - \frac{\mu_{tr}}{6}\, a_{0,tr} + \frac{b_{1,tr}}{16}\, \mu_{tr}^2 \right) + b_{1,tr} \left(-\frac{a_{1,tr}}{8} + \mu_{tr}\, \frac{\lambda_{tr}}{4} + \frac{a_{1,tr}}{16}\, \mu_{tr}^2 \right) \right] + \\
- \frac{1}{2} \left[\lambda_{tr}^2 + \lambda_{tr}\, \mu_{tr}\, a_{1,tr} + \mu_{tr}^2 \left(\frac{a_{0,tr}^2}{2} + \frac{3}{8}\, a_{1,tr}^2 + \frac{b_{1,tr}^2}{8} \right) \right] + \frac{\mu_{tr}}{3}\, a_{0,tr}\, b_{1,tr} - \frac{1}{8}\, \left(a_{1,tr}^2 + b_{1,tr}^2 \right) \\
- \left[\frac{\mu_{tr}}{6}\, (\theta_{tr} - K_{1,tr}\, a_{0,tr}) + \frac{1}{8}\, K_{1,tr}\, b_{1,tr} - \frac{a_{1,tr}}{4} \right]\, \frac{p_{tr}}{\Omega_{tr}} \\
\left. - \left(\frac{1}{8}\, K_{1,tr}\, a_{1,tr} + \frac{b_{1,tr}}{4} - \mu_{tr}\, \frac{a_{0,tr}}{3} \right)\, \frac{q_{tr}}{\Omega_{tr}} - \frac{1}{8} \left[\left(\frac{p_{tr}}{\Omega_{tr}} \right)^2 + \left(\frac{q_{tr}}{\Omega_{tr}} \right)^2 \right] \right\}
\end{aligned}
\tag{2.51}
$$

In the latter expression δ_{tr} is the equivalent tail rotor blade profile drag coefficient which can be obtained as:

$$
\delta_{tr} = 0.009 + 0.3 \left(\frac{6\, C_{t,tr}}{\sigma_{tr}\, Cl_{\alpha,tr}} \right)^2 \tag{2.52}
$$

In the body fram,e the forces and moments can be rewritten as:

$$F_{b,tr} = \begin{bmatrix} -Y_{w,tr}\,\sin\beta_{tr} - H_{w,tr}\,\cos\beta_{tr} \\ \chi\,T_{tr} \\ Y_{w,tr}\,\cos\beta_{tr} - H_{w,tr}\,\sin\beta_{tr} \end{bmatrix} \tag{2.53}$$

$$M_{b,tr} = M_{GH_{tr}}\,F_{b,tr} + [0 \quad -\xi\,Q_{tr} \quad 0]^t \tag{2.54}$$

where ξ is the free-wheel coefficient which is 1 during normal flight and 0 in autorotation and

$$M_{GH_{tr}} = \begin{bmatrix} 0 & -z_{tr} & y_{tr} \\ z_{tr} & 0 & -x_{tr} \\ -y_{tr} & x_{tr} & 0 \end{bmatrix} \tag{2.55}$$

2.6.4 Fuselage

For the fuselage a simple aerodynamic model is adopted. The velocity of the air felt by the fuselage, written in the body frame is:

$$V_f = V_b^{air} + [0 \quad 0 \quad w_{i,f}]^t = [u_f \quad v_f \quad w_f]^t \tag{2.56}$$

where $w_{i,f}$ is the downwash induced by the rotor on the fuselage. It can be evaluated as a polynomial function of the rotor wake angle χ and the induced velocity v_i

$$w_{i,f} = P_f(\chi)\cdot v_i \tag{2.57}$$

$$\chi = \arctan\frac{\mu}{-\lambda} \tag{2.58}$$

The angle of attack and sideslip of the fuselage are:

$$\alpha_f = \arctan \frac{w_f}{u_f} \tag{2.59}$$

$$\beta_f = \arctan \frac{v_f}{||V_f||} \tag{2.60}$$

Finally the fuselage aerodynamic forces and moments, in the local wind reference frame centered in the fuselage pressure center can be written as:

$$F_{w,f} = \begin{bmatrix} -D_f \\ Y_f \\ -L_f \end{bmatrix} = \frac{1}{2}\,\rho\, V_f^2\, S_{ref} \begin{bmatrix} -C_D(\alpha_f, \beta_f) \\ C_Y(\alpha_f, \beta_f) \\ -C_L(\alpha_f, \beta_f) \end{bmatrix}$$

where the aerodynamic coefficients have been taken from Ref. [40].

Forces and moments in the body frame are:

$$F_{b,f} = \boldsymbol{T_f}\,(\alpha_f, \beta_f)\; F_{w,f}$$

$$M_{b,f} = GP_f \times F_{b,f}$$

with $GP_f = r_f$ indicating the fuselage pressure center in the body reference frame

and the matrix $\boldsymbol{T_f}$ is defined as:

$$\boldsymbol{T_f}\left(\alpha_f, \beta_f\right) = \begin{bmatrix} -\cos\alpha_f \cos\beta_f & -\sin\alpha_f \sin\beta_f & \sin\alpha_f \\ -\sin\beta_f & \cos\beta_f & 0 \\ -\sin\alpha_f \cos\beta_f & -\sin\alpha_f \sin\beta_f & -\cos\alpha_f \end{bmatrix}$$

2.7 Flapping dynamics

Flapping motion of the rotor blades is due to the effect of the aerodynamic force on every single blade. These forces, depending on the air-velocity hitting each blade, and the pitch commands, are therefore a function of the blade position around the rotor shaft (blade azimuth ψ_{bl}). The resultant flapping angle will then change itself during the blade rotation. A first harmonic series is often used to describe the flapping angle distribution around the rotor shaft. This kind of representation takes the name of tip-path-plane representation:

$$\beta(\psi_{bl}, t) = a_0(t) + a_1(t)\cos\psi_{bl} + b_1(t)\sin\psi_{bl} \tag{2.61}$$

The time-variant flapping coefficients correspond to the coning angle a_0, and the longitudinal and lateral flapping angles a_1, b_1 as shown in Fig. 2.1. The dynamic equation for the flapping coefficient is a second-order linear dynamics given by:

$$\ddot{a} = f - D\,\dot{a} - K\,a \tag{2.62}$$

where the matrices D, K and f are reported in the following. A complete derivation of the flapping dynamics can be found in Ref. [12].

$$D = \Omega \begin{bmatrix} \frac{\gamma}{2}\left(\frac{1}{4} - \frac{2}{3}\varepsilon + \frac{\varepsilon^2}{2}\right) & 0 & -\frac{\gamma\mu}{4}\left(\frac{1}{3} - \varepsilon + \varepsilon^2\right) \\ 0 & \frac{\gamma}{2}\left(\frac{1}{4} - \frac{2}{3}\varepsilon + \frac{\varepsilon^2}{2}\right) & 2 \\ -\frac{\gamma\mu}{2}\left(\frac{1}{3} - \varepsilon + \varepsilon^2\right) & -2 & \frac{\gamma}{2}\left(\frac{1}{4} - \frac{2}{3}\varepsilon + \frac{\varepsilon^2}{2}\right) \end{bmatrix} \tag{2.63}$$

$$K = \Omega^2 \begin{bmatrix} p^2 + \gamma K_1 \frac{\mu^2}{4}(\frac{1}{2} - \varepsilon + \frac{\varepsilon^2}{2}) & -\frac{\gamma\mu}{4}(\frac{\varepsilon}{2} - \varepsilon^2) & -\frac{\gamma K_1 \mu}{4}(\frac{2}{3} - \varepsilon) \\ -\frac{\gamma\mu}{2}(\frac{1}{3} - \frac{\varepsilon}{2}) & p^2 - 1 + \gamma K_1 \frac{\mu^2}{8}(\frac{1}{2} - \varepsilon + \frac{\varepsilon^2}{2}) & \frac{\gamma}{2}(\frac{1}{4} - \frac{2}{3}\varepsilon + \frac{\varepsilon^2}{2}) \\ & & +\frac{\gamma\mu^2}{8}(\frac{1}{2} - \varepsilon + \frac{\varepsilon^2}{2}) \\ \frac{K_1}{2}\gamma\mu\left(\varepsilon - \frac{2}{3}\right) & \frac{\gamma\mu^2}{8}\left(\frac{\varepsilon^2}{2} - \varepsilon + \frac{1}{2}\right) & \frac{3}{8}K_1\gamma\mu^2\left(\frac{\varepsilon^2}{2} - \varepsilon + \frac{1}{2}\right) \\ & -\frac{\gamma}{2}\left(\frac{\varepsilon^2}{2} - \frac{2\varepsilon}{3} + \frac{1}{4}\right) & + p^2 - 1 \end{bmatrix} \tag{2.64}$$

$$p^2 = 1 + \frac{K_\beta}{I_\beta \Omega^2} + \frac{e\, M_\beta}{g\, I_\beta} + \frac{\gamma\, K_1}{8}\left(1 - \frac{4}{3}\varepsilon\right) \tag{2.65}$$

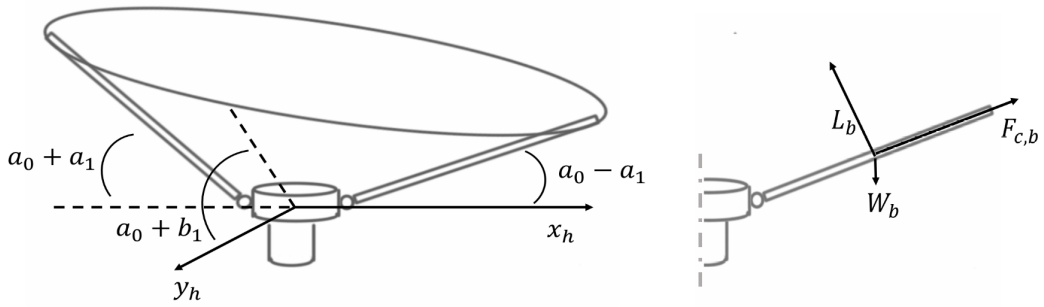

Figure 2.1: Flapping coefficients and equilibrium around the blade hinge

$$
f = \Omega^2 \left[\begin{array}{l}
-\frac{M_b}{I_b\,\Omega^2} + \frac{\gamma}{2}\left[\left(\frac{1}{4}-\frac{\varepsilon}{3}\right) + \frac{\mu^2}{2}\left(\frac{1}{2}-\varepsilon+\frac{\varepsilon^2}{2}\right)\right]\theta_0 - \frac{\gamma}{2}\mu\left(\frac{1}{3}-\frac{\varepsilon}{2}\right) B_{1c} \\
+\frac{\gamma}{2}\left[\left(\frac{1}{5}-\frac{\varepsilon}{4}\right) + \frac{\mu^2}{2}\left(\frac{1}{3}-\frac{\varepsilon}{2}\right)\right]\theta_t + \frac{\gamma}{2}\left(\frac{1}{3}-\frac{\varepsilon}{2}\right)\lambda + \frac{\gamma}{8}\mu\left(\frac{2}{3}-\varepsilon\right)\left(\frac{p_h}{\Omega}\cos\beta_w + \frac{q_h}{\Omega}\sin\beta_w\right) \\
\\
-2\left(1 + e\,\frac{M_b}{g\,I_b}\right)\left(\frac{p_h}{\Omega}\cos\beta_w + \frac{q_h}{\Omega}\sin\beta_w\right) + \left(\frac{\dot{p}_H}{\Omega^2}\sin\beta_w - \frac{\dot{q}_H}{\Omega^2}\cos\beta_w\right) \\
+\frac{\gamma}{2}\left[\left(\frac{1}{4}-\frac{\varepsilon}{3}\right) + \frac{\mu^2}{4}\left(\frac{1}{2}-\varepsilon+\frac{\varepsilon^2}{2}\right)\right] A_{1c} + \frac{\gamma}{2}\left(\frac{1}{4}-\frac{\varepsilon}{3}\right)\left(\frac{p_h}{\Omega}\sin\beta_w - \frac{q_h}{\Omega}\cos\beta_w\right) \\
\\
-2\left(1 + \frac{e\,M_b}{g\,I_b}\right)\left(\frac{p_h}{\Omega}\,sin\,(\beta_w) - \frac{q_h}{\Omega}\cos\beta_w\right) - \left(\frac{\dot{p}_H}{\Omega^2}\cos\beta_w + \frac{\dot{q}_H}{\Omega^2}\sin\beta_w\right) - \frac{\gamma}{2}\mu\left(\frac{2}{3}-\varepsilon\right)\theta_0 \\
-\frac{\gamma}{2}\mu\left(\frac{1}{2}-\frac{2}{3}\varepsilon\right)\theta_t + \frac{\gamma}{2}\left[\left(\frac{1}{4}--\frac{\varepsilon}{3}\right) + 3\,\frac{\mu^2}{4}\left(\frac{1}{2}-\varepsilon+\frac{\varepsilon^2}{2}\right)\right] B_{1c} - \gamma\,\frac{\mu}{2}\left(\frac{1}{2}-\varepsilon+\frac{\varepsilon^2}{2}\right)\lambda \\
-\frac{\gamma}{2}\left(\frac{1}{4}-\frac{\varepsilon}{3}\right)\left(\frac{p_h}{\Omega}\cos\beta_w + \frac{q_h}{\Omega}\sin\beta_w\right)
\end{array} \right] \tag{2.66}
$$

Refers to nomenclature and section 2.6.2 for the main rotor inner variables definition and symbols. Complete derivation of the flapping equations can be found in Ref. [11, 12].

2.8 Inflow dynamics

The rotor inflow is the name given to the flowfield induced by the rotor at the rotor disc. It contributes to the local blade incidence and dynamic pressure, then also to the aerodynamic forces. This makes it considerably important in the helicopter dynamics modeling. The real inflow distribution depends on several aerodynamic effects which are difficult to model unless very complex and computationally demanding techniques are involved. It is commonly assumed that for flight dynamics analysis it is sufficient to consider only the normal component of inflow (the induced downwash). In Fig. 2.2 the air velocity components on the rotor are illustrated. Here it is possible to distinguish two in-plane components u_h, v_h, and two vertical components w_h and v_i. While u_h,v_h and w_h depends on the helicopter motion and the wind velocity, v_i represents the properly said induced inflow rate or induced velocity. The adimensional form of the induced velocity is given by the induced inflow ratio:

$$\lambda_{i,0} = \frac{v_i}{\Omega R} \tag{2.67}$$

while we call total inflow λ the following variable:

$$\lambda = \frac{w_h - v_i}{\Omega R} = \mu_z - \lambda_{i,0} \tag{2.68}$$

The advance ratio is instead defined as in Eq. (2.36). The physical origin of the induced velocity can be explained by the traditional momentum theory. According to this theory the thrust delivered by the rotor is due to the mass flow induced by the rotor. The momentum theory also evaluates the relationship between the induced

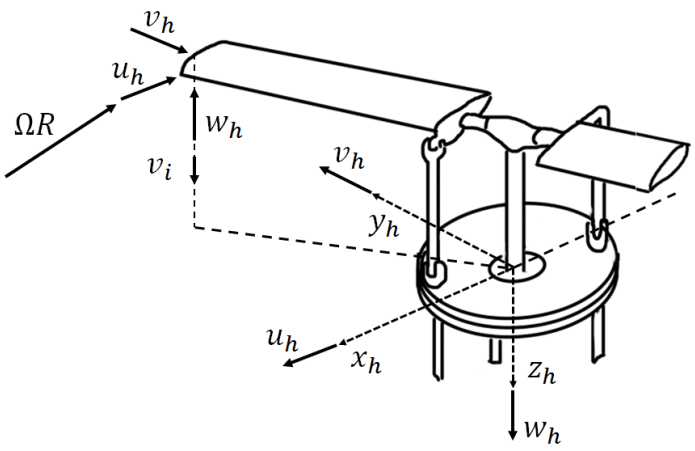

Figure 2.2: Velocity components at the blade

velocity and the rotor thrust under the following hypothesis:

- inviscid and incompressible flow
- monodimensional steady flow across the rotor
- the rotor determines a discontinuity on the air velocity (disc actuator theory)
- well-defined slipstream between the flowfield generated by the rotor and the external air

Writing the momentum conservation equation for such a system, a static relation between the thrust coefficient C_T and the induced inflow ratio is obtained in steady conditions:

$$\lambda_{i,0} = \frac{C_T}{2\sqrt{\mu^2 + (\lambda_{i,0} - \mu_z)^2}} \tag{2.69}$$

Previous equations are related to the mean induced inflow ratio around the rotor disc. A slightly more complex model assumes an induced flow field of the form:

$$\lambda_i(\psi_{bl}, r) = \lambda_{i,0} + \lambda_{i,s}\frac{r}{R}\sin\psi_{bl} + \lambda_{i,c}\frac{r}{R}\cos\psi_{bl} \tag{2.70}$$

where r is the position along the blade span while ψ_{bl} is the azimuth around the rotor shaft. The coefficient $\lambda_{i,0}$ is the mean inflow ratio while $\lambda_{i,c}$ and $\lambda_{i,s}$ correspond to the longitudinal and lateral inflow coefficients. Assuming time-dependent inflow coefficients, a dynamic system has been developed by Peters at al [38]:

$$\begin{pmatrix} \dot{\lambda}_{i,0} \\ \dot{\lambda}_{i,s} \\ \dot{\lambda}_{i,c} \end{pmatrix} = \Big[\mathbf{M}\Big]^{-1} \left\{ \begin{pmatrix} C_T \\ -C_{l_h} \\ -C_{m_h} \end{pmatrix} - \Big[\mathbf{L}\Big]^{-1} \begin{pmatrix} \lambda_{i,0} \\ \lambda_{i,s} \\ \lambda_{i,c} \end{pmatrix} \right\} \tag{2.71}$$

where C_T is the thrust coefficient, C_{l_h} and C_{m_h} are the roll and pitch moment coefficients in hub-body frame whereas the detailed matrices $\mathbf{M}$, $\mathbf{L}$ can be found in Ref. [38].

A simplified dynamic-uniform model, derived from the previous one, has been adopted for the autorotation steady descent calculation, for the flare optimization algorithm, and for the inflow ratio estimation. This model is given below:

$$\dot{\lambda}_{i,0} = f_{\lambda_i}(x, \dot{x}, u) = \frac{3\,\pi}{4}\left\{\frac{C_T}{2} - \lambda_{i,0}\sqrt{\mu^2 + \lambda^2}\right\} \tag{2.72}$$

2.9 Ground effect

When the helicopter flies close to the ground, some special characteristics in the flight dynamic behavior appear. The most significant is the effect on the induced velocity at the rotor and hence the rotor thrust and power required. In Ref. [10], Cheeseman and Bennett modeled this effect according to the potential flow theory and calculated the reduction of the induced velocity as:

$$\delta v_i = \frac{A_d \, v_i}{16 \, \pi \, z_g^2} \tag{2.73}$$

where A_d is the disc area and z_g is the distance of the ground below the rotor disc. Ground effect is most significant in hover, and, below heights of the order of a rotor radius, thrust increments of between 5 and 15% are predicted.

2.10 Rotor dynamics

Rotor dynamics can be derived from the kinetic energy theorem applied to the helicopter main rotor and the tail rotor velocity:

$$\frac{dT_{rot}}{dt} = P_{active} \tag{2.74}$$

Where P_{active} is the power of the system, which is given by:

$$P_{active} = [M_{engine} - Q] \cdot \Omega - Q_{tr} \cdot \Omega_{tr} \tag{2.75}$$

Considering the constant velocity ratio, due to the mechanical transmission between the main rotor and tail rotor $\tau = \Omega_{tr}/\Omega$ we can rewrite the previous equation as:

$$P_{active} = [M_{engine} - Q - \tau Q_{tr}] \cdot \Omega \tag{2.76}$$

The kinetic energy can now be written as:

$$T_{rot} = \frac{1}{2} I_{mr} \Omega^2 + \frac{1}{2} I_{tr} \Omega_{tr}^2 = \frac{1}{2} \left[I_{mr} + I_{tr}\, \tau^2 \right] \Omega^2$$

Deriving the kinetic energy and considering the previous equations the following is obtained:

$$\dot{\Omega} = \frac{M_{engine} - (Q + Q_{tr}\, \tau)}{I_{mr} + I_{tr}\, \tau^2}$$

In normal flight, the aerodynamic torque is compensated by the engine and the kinetic energy of the rotors is kept constant. During autorotation the engine is no more able to deliver its power and the angular rate of the rotors changes. Tail rotor contributions for the rotational dynamics are second-order terms and can therefore be neglected obtaining the following equation for autorotation:

$$\dot{\Omega} = -\frac{Q}{I_{mr}} \tag{2.77}$$

Chapter 3

Autorotation maneuver design

3.1 Introduction

Helicopter autorotation landing is an emergency maneuver performed in the case of a total loss of engine power. It can be divided into three phases: (i) an initial transient after engine failure; (ii) a quasi-steady descent, and (iii) the flare and touch–down. When the engine fails, the rotor aerodynamic torque is no longer balanced by the engine shaft torque. If the rotor rate drops below a critical value, blades stall, rotor thrust drops rapidly to zero and the vehicle falls along a quasi-ballistic trajectory. Nevertheless, if the rotor collective is rapidly reduced after engine failure, a descent trajectory is started because of thrust reduction, without the rotor losing too much rpm. The airflow impinging on the rotor disk from below during a descent allows the rotor to reach an autorotation condition, such that the net aerodynamic torque vanishes, while rotor thrust can still balance helicopter weight. Depending on airspeed magnitude and direction, it is possible to evaluate rotor rate at autorotation Ω for each value of θ_0.

By properly choosing collective pitch, constant rotor velocity and sink rate are maintained along an almost rectilinear, quasi-steady descent in autorotation. The most critical part is the third one, that is, the final flare and touch-down, during which the sink rate must be reduced as close as possible to zero, prior to landing the helicopter, while minimizing the residual forward speed component. During this last phase, the reduction of the sink rate is obtained by increasing rotor thrust, acting on the main rotor collective, while pulling up the helicopter, for reducing forward speed. Such a control action also increases rotor aerodynamic torque, which, in turn, causes rotor rate to decrease. On one side, if the collective pitch increment is too large or too early, the rotor rate drops too much before the helicopter touches the ground, the rotor stalls, and the helicopter crashes. If, on the other hand, the control action on θ_0 is too mild or delayed, the sink rate at touch-down remains too high, and the helicopter crashes for the opposite reason. At this stage, the rotor kinetic energy is the only energy source available for performing the final flare and deceleration maneuver. Hence maintaining an adequate level of rotor rpm during the steady descent, while maintaining a sink rate and forward speed as small as possible, is a crucial aspect of the whole autorotation maneuver design.

A large forward velocity component is also dangerous, provided that the helicopter can crash into an obstacle, while skidding on the ground, after touch-down. Hence, the control action on longitudinal cyclic pitch needs to be phased well with respect to collective pitch variation. Moreover, the pitch-up attitude required for deceleration needs to be bounded at lower altitudes, immediately prior to touch-down, to avoid the risk of a tail-strike.

In the next sections, the starting hypothesis and constraints, and the maneuver design are described in detail.

Here a summary of the main steps followed for the autorotation maneuver design is given:

- calculation of all the helicopter steady descent conditions using a trim algorithm;
- design of a suitable robust flare profile easily to be implemented for on-board systems;
- optimization of the maneuver parameters.

3.2 Maneuver definition

Some simplifications and methodological choices are introduced in the design of the autorotation maneuver:

- the whole maneuver is assumed to be purely longitudinal and there is no constraint on the final position, as if the landing field is infinite;
- the design of the maneuver is performed by analyzing separately the second steady descent phase and the final flare;
- the overall desired autorotation path is obtained by joining the trajectories followed during these two phases;
- the initial transient is neglected, in the sense that it is assumed that the helicopter can achieve the required steady descent autorotation condition required

for the second part of the maneuver simply by the application of the corresponding controls at trim.

Letting u_{td}, v_{td}, and w_{td} the inertial forward, lateral, and vertical speed components at touch-down, respectively, considered bounds on terminal values of all relevant variables are reported in the following

$$\begin{aligned} |u_{td}| &\leq u_{max} = 0.25\,\mathrm{m/s} \\ |v_{td}| &\leq v_{max} = 0.25\,\mathrm{m/s} \\ |w_{td}| &\leq w_{max} = 0.20\,\mathrm{m/s} \\ \theta_{td} &\leq \arctan(h_{hel}/l_t) \end{aligned} \tag{3.1}$$

where l_t is the length of the tail boom and h_{hel} is the distance between the center of mass and landing gear waterlines.

3.3 Steady descent conditions

All the possible steady descent conditions have been evaluated considering the whole helicopter mathematical model and calculating the equilibrium conditions for imposed values of advancing velocity u_e and sink rate w_e.

The following conditions are imposed for a longitudinal flight in steady state:

$$\begin{cases} V_e = [u_e \quad 0 \quad w_e]^T \rightarrow V_b = T_{be}\, V_e \\ \omega_b = [0 \quad 0 \quad 0]^T \\ \dot{a} = [0 \quad 0 \quad 0]^T \end{cases} \tag{3.2}$$

The resulting problem is given by:

$$\begin{cases} \dot{V}_b = \frac{F_b}{m} - \omega_b \times V_b = 0 \\ \dot{\omega}_b = I^{-1}(M_b - \omega_b \times I\omega_b) = 0 \\ \ddot{a} = -D\,\dot{a} - K\,a + f = 0 \\ \dot{\lambda}_i = \frac{3\,\pi}{4}\left(\frac{C_T}{2} - \lambda_i \sqrt{\mu^2 + \lambda^2}\right) = 0 \\ \dot{\Omega} = -\frac{Q}{I_{mr}} = 0 \end{cases} \tag{3.3}$$

which can be written as:

$$\begin{cases} F_b(V_e, a, u, \phi, \theta, \lambda, \Omega) = 0 \\ M_b(V_e, a, u, \phi, \theta, \lambda, \Omega) = 0 \\ f_a(V_e, a, u, \phi, \theta, \lambda, \Omega) = 0 \\ f_\lambda(V_e, a, u, \phi, \theta, \lambda, \Omega) = 0 \\ Q(V_e, a, u, \phi, \theta, \lambda, \Omega) = 0 \end{cases} \tag{3.4}$$

The problem is a nonlinear system of 11 equations in 11 unknowns and it has

been numerically solved using a Newton-like gradient method.

The resulting value of the rotor angular rate Ω, for steady descent conditions in autorotation, over a grid of imposed advancing and vertical velocities, is reported in Fig. 3.1 and Fig. 3.2. Here clearly appears how the resulting rotor angular rate largely depends on the vertical velocity, while a weaker correlation exists with the advancing velocity. Nevertheless, fixing the target rotor rate, a minimum sink rate exists for a proper advancing velocity which corresponds to the minimum power velocity.

In Fig. 3.3 it is possible to see how the sink rate and the rotor speed vary as a function of the collective for a fixed advancing speed. More precisely, sink rate and rotor angular rate decrease when high values of collective are chosen. This effect can be easily explained by considering how the three key variables (collective, vertical velocity, and rotor angular rate) take part in the vertical and rotational equilibrium during autorotation. In the steady descent conditions, we have $T \approx W$ and it is also $T \propto \theta_0, \Omega^2, w_e$. The thrust needed to equilibrate the weight force can therefore be obtained in two conditions:

- For low values of collective and high values of rotor rate and sink rate
- For high values of collective and low values of rotor speed and rate of descent

Moreover, increasing the collective, Ω decreases faster than w_e because the thrust and the aerodynamic torque on the main rotor largely depend on the angular rate. For the same reason, advisable values of collective to be set during the steady descent, are lower values: losing rotor energy to keep a slightly lower vertical speed, is in general

worse than saving rotor speed (and its thrust generation capability) and obtaining higher steady vertical velocity.

As visible in Fig. 3.1, for certain values of low vertical and horizontal speeds no steady descent conditions are considered. This region must be avoided because it corresponds to the vortex ring state condition which is a very critical aerodynamic condition. After the power loss, the helicopter passes from traction condition to windmill condition. Between these two, lays the vortex ring state which is obtained when the rotor-induced velocity and the vertical velocity are similar: $\frac{1}{2}v_i < w_h < 2v_i$ [41]. To be out of the vortex ring state during the steady descent it is necessary to set $w_h > 2v_i$.

The exit vortex ring state curve $w_h = 2v_i$ can be calculated in the $u_e \times w_e$ plane. The steady-state solution of the inflow dynamics equation in Eq. (2.72) gives:

$$\lambda_i = \frac{C_T}{2\sqrt{\mu^2 + \lambda^2}} \tag{3.5}$$

From the vortex ring state condition, we can rewrite the induced inflow rate as

$$\lambda_i = \frac{v_i}{\Omega R} = \frac{1}{2}\frac{w_h}{\Omega R} \tag{3.6}$$

and the inflow rate as:

$$\lambda = \frac{w_h - v_i}{\Omega R} = \frac{1}{2}\frac{w_h}{\Omega R} \tag{3.7}$$

Considering the following simplifications:

$$\begin{aligned} \theta &\approx 0 \\ T &\approx m\,g \\ w_h &\approx w_e \\ u_h &\approx u_e \rightarrow \mu \approx \frac{u_e}{\Omega R} \end{aligned} \tag{3.8}$$

and putting all together we finally have:

$$u_{e,min} = \begin{cases} \sqrt{\left(\frac{mg}{\rho A}\right)^2 \frac{1}{w_e^2} - \frac{w_e^2}{4}} & \text{if} \quad w_e < \sqrt{\frac{2\,m\,g}{\rho\,A}} \\ -\infty & \text{if} \quad w_e \geq \sqrt{\frac{2\,m\,g}{\rho\,A}} \end{cases} \tag{3.9}$$

So to be out of the vortex ring state during the steady descent we have to set $u_e(w_e) > u_{e,min}(w_e)$

3.4 Flare profile

The flare represents the most critical phase for autorotation. During the flare, collective and longitudinal commands need to be managed to exploit rotor kinetic energy to reduce advancing and descent velocities at touch-down. A critical issue is the evaluation of the proper altitude at which the flare should start. An early flare can be catastrophic since the rotor energy and its capability of delivering a thrust can run out before touch-down leaving the helicopter in a free fall. On the other side, a late flare hasn't got the time necessary to decelerate the rotorcraft with a similar

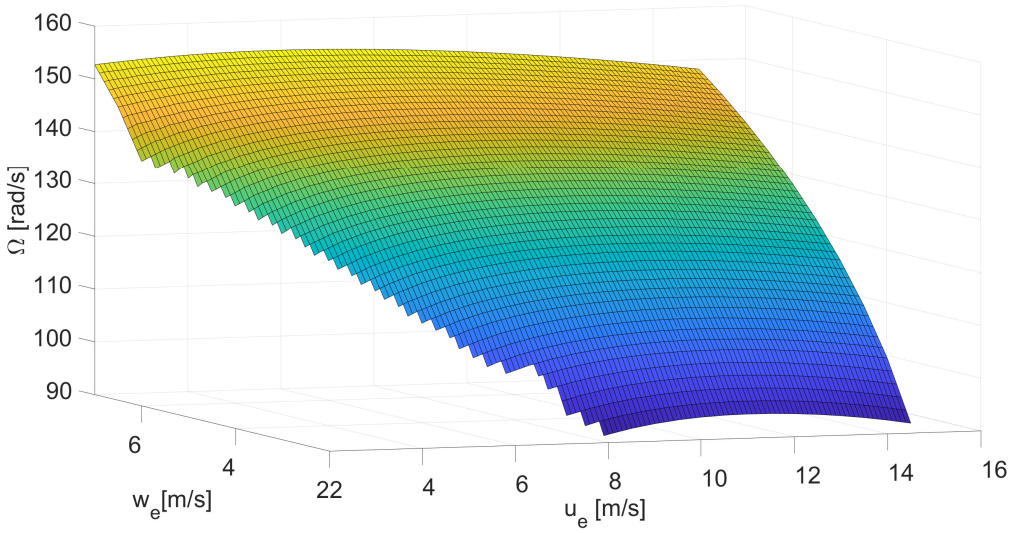

Figure 3.1: Rotor angular rate for different autorotation steady descent conditions

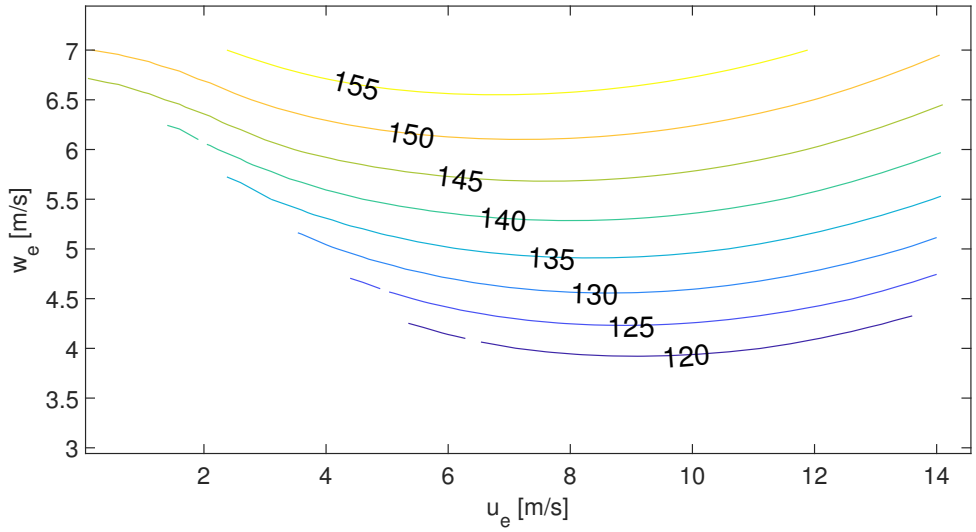

Figure 3.2: Contour of rotor angular rates (rad/s) for different autorotation steady descent conditions

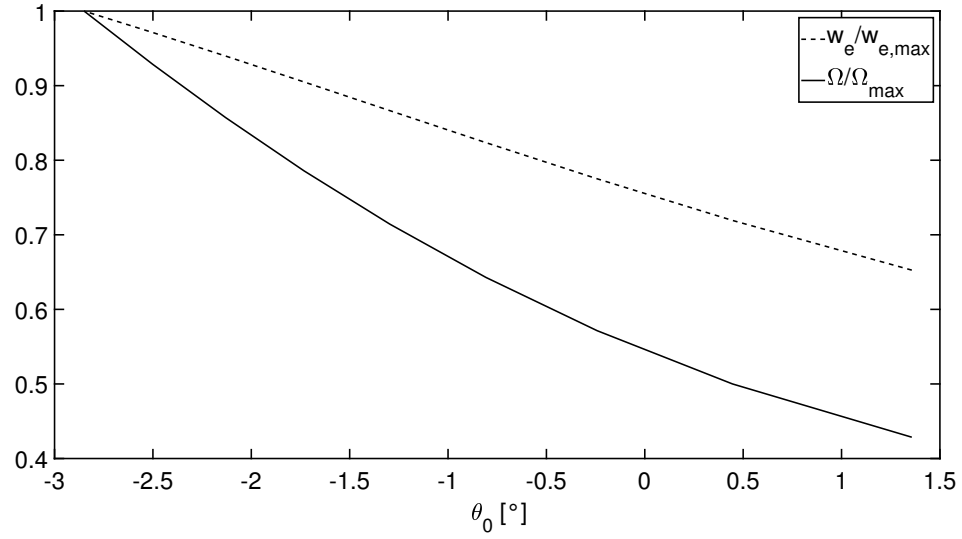

Figure 3.3: Sink rate and rotor angular rate as function of collective for fixed $u_e = 7.5\,m/s$

bad result.

For the design of the flare, these main points have been considered:

- the flare must follow a simple trajectory where the velocity decreases getting a minimum value at touch-down;
- the flare trajectory must be easily planned and corrected in real-time;
- a tracking system should be able to follow the path easily.

For the second and third tasks, the idea is to calculate at every time step, a reference horizontal and vertical velocity to follow. This reference has to be a function of the measured state. In particular, it is chosen to be a 2nd-order polynomial function of

the altitude such as:

$$u_{e,des} = \alpha_u\, h^2 + \beta_u\, h + \gamma_u \tag{3.10}$$

$$w_{e,des} = \alpha_w\, h^2 + \beta_w\, h + \gamma_w \tag{3.11}$$

The initial and final conditions on the velocity we need to consider are:

$$\begin{cases} u_{e,des} = u_0 & \text{when} \quad h = h_0 \\ w_{e,des} = w_0 & \text{when} \quad h = h_0 \\ u_{e,des} = 0 & \text{when} \quad h = 0 \\ w_{e,des} = 0 & \text{when} \quad h = 0 \end{cases} \tag{3.12}$$

Where u_0 and w_0 are the steady descent conditions and h_0 is the altitude at which the flare starts. To ensure a better continuity between the steady descent condition and the flare, zero accelerations are imposed at the initial point of the flare:

$$\begin{cases} \dot{u}_{e,des} = 0 & \text{when} \quad h = h_0 \\ \dot{w}_{e,des} = 0 & \text{when} \quad h = h_0 \end{cases} \tag{3.13}$$

Imposing the mentioned conditions to the desired form in Eq. (3.10)-(3.11) we have:

$$\begin{cases} \gamma_u = 0 \\ \gamma_w = 0 \\ \alpha_u = -\frac{u_0}{h_0^2} \\ \alpha_w = -\frac{w_0}{h_0^2} \\ \beta_u = \frac{2\,u_0}{h_0} \\ \beta_w = \frac{2\,w_0}{h_0} \end{cases} \tag{3.14}$$

and the trajectory can be rewritten as:

$$u_{e,des}(h) = -\frac{u_0}{h_0^2}\,h^2 + 2\,\frac{u_0}{h_0}\,h \tag{3.15}$$

$$w_{e,des}(h) = -\frac{w_0}{h_0^2}\,h^2 + 2\,\frac{w_0}{h_0}\,h \tag{3.16}$$

$$u_{e,des} = w_{e,des}\,\frac{u_0}{w_0} \tag{3.17}$$

The trajectory depends only on three parameters to be chosen: the initial altitude for the flare h_0, and the steady descent conditions u_0 and w_0. The time-law of the trajectory can be calculated considering that:

$$w_{e,des} = -\frac{dh_{des}}{dt} = \alpha_w\,h^2 + \beta_w\,h \tag{3.18}$$

Integrating we obtain:

$$h_{des}(t) = \frac{2\,h_0\,e^{-\beta_w\,t}}{1+e^{-\beta_w\,t}} \tag{3.19}$$

For the resulting trajectory, altitude is asymptotically zero for $t \to \infty$. What we will have in practice, is that the helicopter will touch down at finite time with a residual minimum value of velocity.

3.5 Parameters Optimization

All the autorotation maneuver, as designed here, only depends on three variables:

- the steady descent conditions: u_0 and w_0 (or Ω_0);
- the flare initial altitude h_0.

The steady descent velocities represent the kinetic energy we need to dissipate, the rotor rate is the energy storage to be used for the braking, and the flare altitude gives the gravitational potential energy and, at the same time, the spatial limits in which the maneuver has to be performed. The choice is crucial and must guarantee the maneuver success and the trajectory feasibility for the real system. Some constraints, such as the limits on the thrust deliverable by the rotor during the flare, must therefore be considered.

The criterion here proposed for the choice of the autorotation parameters consists of the solution of an optimal problem. As already said, from Eq. (3.19) we have

that zero altitude (and zero velocity) would be reached at infinite time. In reality, at finite time the helicopter will touch down with residual velocity. The idea is to set the final vertical velocity equal to the target velocity w_{td} in Eq. (3.1) and to minimize the residual horizontal velocity imposing some constraint to guarantee the dynamical feasibility of the trajectory. The residual vertical velocity corresponds to a residual theoretical altitude h_{td} and a time step t_{td} which can be calculated by Eq. (3.19) as:

$$h_{td} = h_0 \left(1 - \sqrt{1 - \frac{w_{td}}{w_0}}\right) \tag{3.20}$$

$$t_{td} = \frac{h_0}{2\,w_0} \log\left(\frac{2\,h_0}{h_{td}} - 1\right) \tag{3.21}$$

At this point, the maneuver is considered terminated.

A simplified model of the dynamics is proposed for a faster resolution of the optimization problem. The dynamic equations written in body axes are reported below:

$$\dot{u}_b = \frac{1}{m}\left(X_{fus} + T\sin i_s\right) - g\sin\theta \tag{3.22}$$

$$\dot{v}_b = \frac{Y_{fus}}{m} + g\sin\phi\cos\theta \tag{3.23}$$

$$\dot{w}_b = \frac{1}{m}\left(Z_{fus} - T\cos i_s\right) + g\cos\theta\cos\phi \tag{3.24}$$

$$\dot{\Omega} = -\frac{Q}{I_{mr}} \tag{3.25}$$

Simplified thrust and torque models are taken from [7]:

$$T = \rho\sigma A(\Omega R)^2 \frac{Cl_\alpha}{4}\left\{\frac{2}{3}\theta_0 \frac{1-\mu^2+9\mu^4/4}{1+3\mu^2/2} + \lambda\frac{1-\mu^2/2}{1+3\mu^2/2}\right\} \tag{3.26}$$

$$Q = \rho\sigma RA\,(\Omega\,R)^2\left\{\frac{\delta}{8}\,(1+3\mu^2) - \frac{\lambda\,C_T}{\sigma}\right\} \tag{3.27}$$

Moreover the rotor dynamics Eq. (2.77) and the inflow dynamics Eq. (2.72) are considered.

For the solution of the optimization problem, we consider a discrete time series $\{k\cdot\delta t\}_{k=0,1,\dots N_t}$ with $\delta t = t_{td}/N_t$. In the optimization algorithm, at every iteration, fixed values of u_0, w_0, and h_0 are taken and a known flare trajectory is obtained. Then accelerations are known and a dynamic inversion can be done to evaluate the attitude and the thrust for every time step. Inverting the thrust equation it is possible to obtain the necessary collective pitch. Finally, from these values, the time series of the rotor angular rate is given numerically integrating the discretized rotor dynamics Eq. (2.77). Added constraints on maximum pull-up angle and velocity are considered to ensure a smooth trajectory.

The optimal problem can be written as:

$$\underset{u_0, w_0, h_0}{\text{minimize}} \quad u_{td} = w_{td} \frac{u_0}{w_0} \tag{3.28a}$$

subject to

$$\text{imposed trajectory of Eq. (3.15)-(3.17)}, \tag{3.28b}$$

$$\text{low order dynamics of Eq. (3.22)-(3.27)}, \tag{3.28c}$$

$$\text{inflow and rotor dynamics Eq. (2.72), (2.77)}, \tag{3.28d}$$

$$\text{final velocity and attitude (3.1)}, \tag{3.28e}$$

$$[u_0, w_0, \Omega_0] \in \text{surface of steady descent conditions}, \tag{3.28f}$$

$$\theta \in [-\theta_{max}, \theta_{max}], \tag{3.28g}$$

$$\delta\theta = \theta_{k+1} - \theta_k < \delta\theta_{max} \quad \forall k \in [0, N_t - 1], \tag{3.28h}$$

$$\theta_0 \in [\theta_{0,min}, \theta_{0,max}], \tag{3.28i}$$

$$\delta\theta_0 = \theta_{0,k+1} - \theta_{0,k} < \delta\theta_{0,max} \quad \forall k \in [0, N_t - 1], \tag{3.28j}$$

$$\Omega_{td} = \Omega_0 - \int_0^{t_{td}} \frac{Q}{I_{mr}}\, dt > \Omega_{td,min} \tag{3.28k}$$

From the previous equations, it is clear that the solution is reached by minimizing the velocity ratio u_0/w_0. By the way, by adding the constraints, the obtained solution is not simply given by choosing the largest vertical velocity and the smallest horizontal velocity. In particular, constraints 3.28f and 3.28h limit the maximum value of w_0 and the minimum value of u_0 imposing to be out of the vortex ring state. The altitude h_0 is mainly affected by the constraints 3.28g and 3.28k which limit the minimum and maximum value respectively. The optimization problem has been

Table 3.1: Optimization parameters and results

Algorithm parameters	value	unit
δt	0.01	s
Θ_{max}	30	°
$\theta_{0,min}$	-5	°
$\theta_{0,max}$	10	°
$\delta\Theta_{max}$	1	°
$\delta\theta_{0,max}$	1	°
$\Omega_{td,min}$	60	rad/s
Optimal solution	**value**	**unit**
u_0	5	m/s
w_0	6	m/s
h_0	10	m
Ω_0	143	rad/s
$J = u_{td}$	0.17	m/s

solved using the Matlab function *fmincon* which exploits an improved sequential-quadratic optimization algorithm with trust region [9]. A trapezoidal quadrature has been considered for the discrete-time integration and derivation of the trajectories. The robustness of the solution has been tested for different initial guesses and time step sizes. Negligible differences are obtained, in the optimization results, when the time step is $\delta t < 0.05$ s, the initial guess for $h_0 < 20$ m, and the initial guess for u_0 and w_0 is in the domain of Fig. 3.1. Settings and results are reported in Tab. 3.1, while Fig. 3.4 shows the resulting nominal optimal flare profile. As expected, an increasing collective is adopted to exploit the rotor kinetic energy allowing the reduction of the vehicle velocity. A pitch-up is also obtained to reduce the advancing speed.

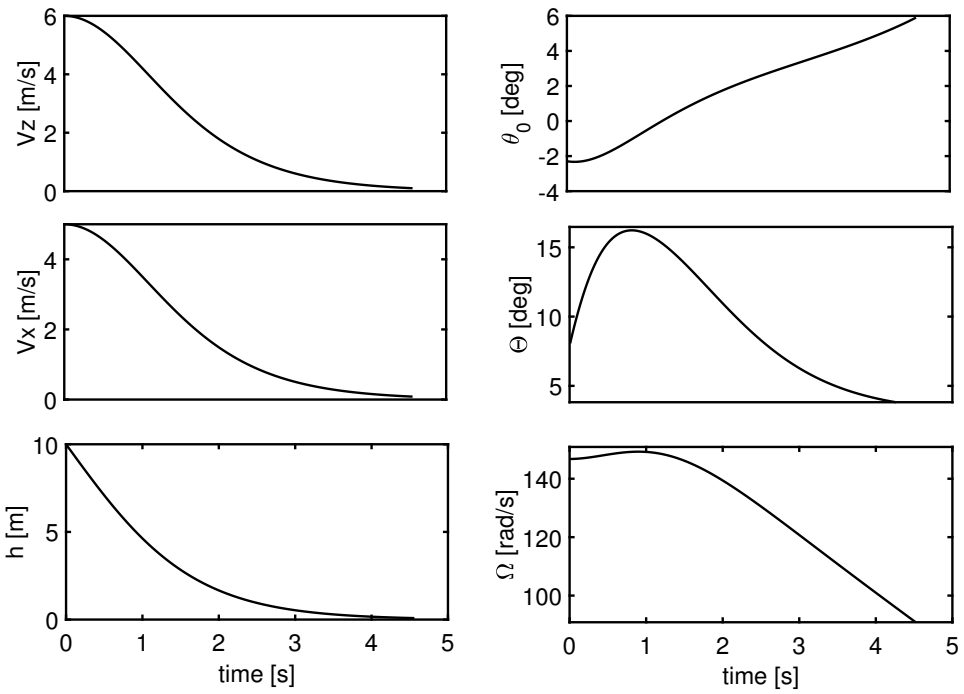

Figure 3.4: Off-line optimal flare profile

Chapter 4

Design of the control system

4.1 Introduction

Controlling a dynamic system means ensuring its stability and driving it to new flight conditions using a correct command law. Several intermediate levels usually exists between the pilot (for piloted systems) and the physical commands received by the helicopter. In the command chain, the inner level, for the helicopter, is represented by the pitch angles of the main rotor and tail rotor blades. Changing the blade pitch, the angle of incidence is changed and new aerodynamic forces and moments are established at the rotors. The command vector, as already defined, is then given by the main rotor collective pitch θ_0, the lateral and longitudinal cyclic pitches A_{1s} and B_{1s}, and the tail rotor pitch θ_{tr}.

To control the helicopter, the first task is represented by its stabilization. Stabilizing a helicopter is of paramount importance since, unlike fixed-wing aircraft, helicopters are naturally unstable. This means that, for a stable flight, in manual mode, a pilot should continuously compensate for oscillations occurring for every

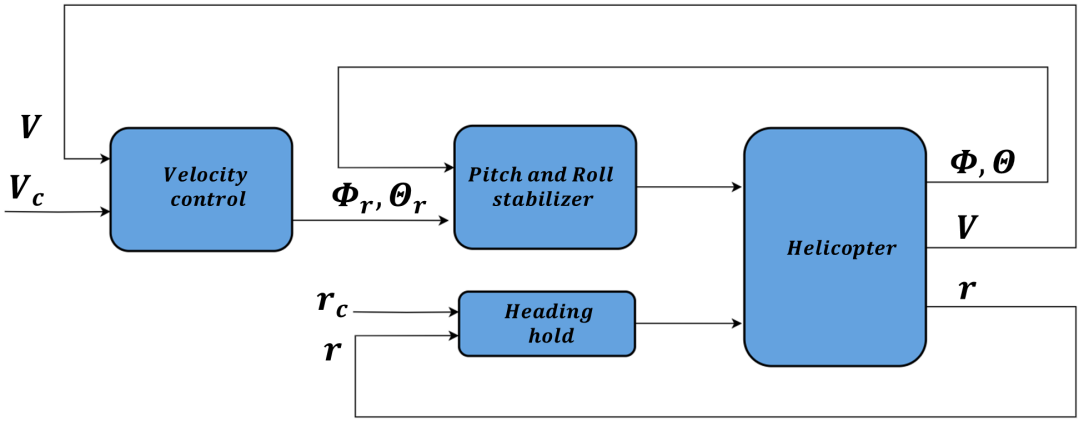

Figure 4.1: Global control architecture

small disturbance. The helicopter stabilization is traditionally done by stability augmentation systems (SAS) which are usually based on an artificial damping obtained giving a continuous command that is proportional to the measured angular rate and in the opposite direction. This ensures roll and pitch stability. Once the stabilization has been achieved, further control loops can be added so that a desired attitude or desired velocity can be commanded to the helicopter. In Fig. 4.1 the global architecture of a traditional control system is reported. Here, an inner loop stabilizes the pitch and roll modes and is used to follow the reference attitude, whereas an outer velocity controller is used to follow a reference velocity. The inner structure of these modules, together with the automatic autorotation control logic, are described in detail in the following sections.

4.2 Attitude control with PID

A basic stabilizer, based on PID technique is used in normal flight conditions for pitch and roll control. The scheme is reported in Fig. 4.2. In both cases, an inner loop controls pitch/roll rates ensuring a stabilizing artificial damping, while in the outer loop, a desired pitch/roll angle is compared with the actual attitude and the error generated becomes a reference for the inner loop. Finally, a proportional mixing logic is added to reduce couplings between the two axes. The stabilizer can receive the reference attitude from a pilot or from a velocity autopilot. The cyclic commands generated by the pitch and roll stabilizers are mathematically described by:

$$\begin{cases} A_{1s} &= A'_{1s} + K_{qp}\, B'_{1s} \\ B_{1s} &= B'_{1s} + K_{pq}\, A'_{1s} \\ A'_{1s} &= P_p\, e_p + D_p\, \dot{e}_p + I_p \int_0^\tau e_p\, dt \\ B'_{1s} &= P_q\, e_q + D_q\, \dot{e}_q + I_q \int_0^\tau e_q\, dt \\ e_p &= P_\phi\, e_\phi - p \\ e_q &= P_\theta\, e_\theta - q \\ e_\phi &= \phi_{des} - \phi \\ e_\theta &= \theta_{des} - \theta \end{cases} \tag{4.1}$$

4.3 Heading hold

The Heading Hold logic is shown in Fig. 4.3. The desired yaw rate, from the pilot or from a outer guidance loop, is compared with the actual yaw rate and the error is

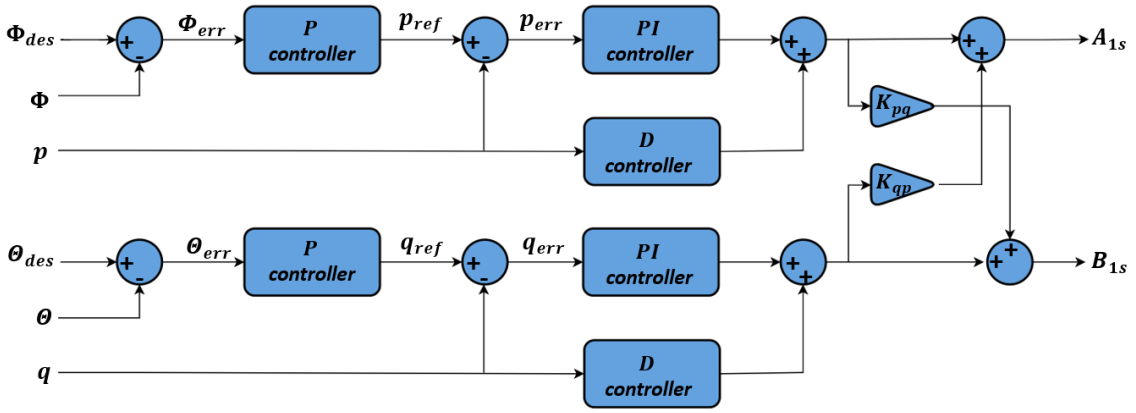

Figure 4.2: Roll and pitch stabilizer

integrated to obtain an estimation of the yaw error. The latter is used to elaborate a desired yaw rate with a proportional gain. Compared to the actual yaw rate, this one generates the error used to elaborate the tail pitch. A fixed contribution $\theta_{0,tr}$ is added to consider the tail rotor thrust needed to balance the main rotor torque at hovering. Another contribution is finally proportional to the main rotor collective and takes into account how, for equilibrium, tail rotor thrust needs to modulate as a function of the main rotor torque, and then as a function of the collective command. This latter contribution is set to zero when the control logic switches from the Engine ON to the autorotation controller, since in autorotation the rotor torque is no longer transmitted to the fuselage thanks to the free-wheel mechanism. Mathematical description of the tail rotor pitch elaborated by the heading hold is

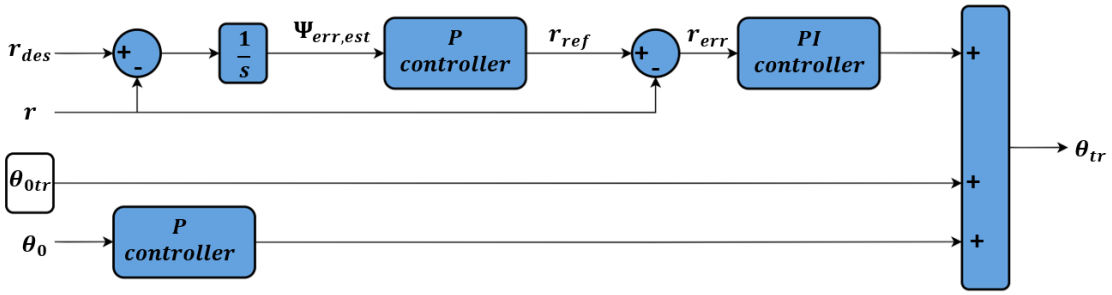

Figure 4.3: Heading hold

reported below:

$$\begin{cases} \theta_{tr} &= \theta'_{tr} + \theta_{0,tr} + P_{\theta_0}\,\theta_0 \\ \theta'_{tr} &= P_r\,e_r + I_r\,\int_0^\tau e_r\,dt \\ e_r &= P_\psi\,e_{\psi,est} - r \\ e_{\psi,est} &= \int_0^\tau (r_{des} - r)\,dt \end{cases} \tag{4.2}$$

4.4 Autorotation phases management

The control logic adopted for the automatic autorotation maneuver needs to change during the main phases of the maneuver. In particular, a first logic needs to be considered to recognize the failure of the powerplant and to start the autorotation maneuver. This logic consists of checking the measured rotor rate and triggering the maneuver when $\Omega < 0.95\,\Omega_{nom}$. A second logic is responsible for starting the flare: this is possible by measuring the altitude and triggering the flare controller when the proper nominal altitude is reached.

4.5 Steady descent control logic

During the steady descent, the system needs to be driven to a chosen steady state condition, namely u_0, w_0, Ω_0. This is done by implementing a control on the rotor angular rate and the vertical velocity as shown in Fig. 4.4. In the first phase, the collective pitch is set to the nominal value $\theta_{0,sd}$ evaluated with the trim algorithm for autorotation. When the rotor speed decreases under the nominal value, a PID feedback control on Ω elaborates the collective pitch to reset it to its nominal steady descent value $\Omega = \Omega_0$. At the same time, the error on the advancing velocity $u_e - u_0$ generates the reference pitch angle given to the pitch stabilizer which elaborates the longitudinal control B_{1s}. Similar control is done for A_{1s} where a desired zero lateral velocity is adopted to elaborate a reference roll angle for the roll stabilizer. Finally, the tail is controlled by the heading hold logic. In autorotation, the tail loses its normal role because thanks to the free-wheel mechanism the rotor torque is no longer discharged to the fuselage. Small tail contributions are necessary only at touch down and in the first phase, just after the engine failure.

4.6 Flare controller

The flare control logic (Fig. 4.5) is made up of two main modules: a trajectory planner, and a trajectory tracker. The first one evaluates, at every time step, a desired vertical and horizontal velocity while the tracker is an autopilot which evaluates the errors on velocities and calculates a reference attitude and a collective command. The desired attitude is given to the stabilizer which generates the cyclic commands.

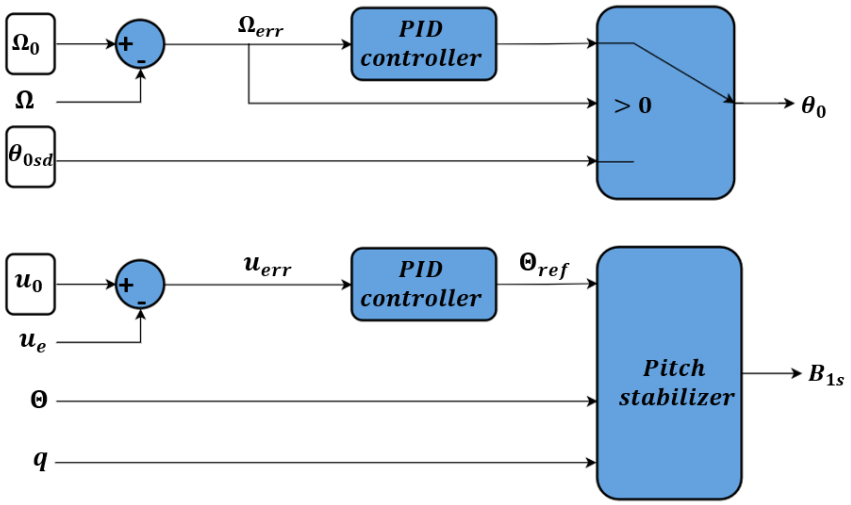

Figure 4.4: Steady descent controllers

According to what has been seen in section 3.4 the desired velocities are polynomial functions of the altitude, and depend on the initial conditions u_0, w_0, and h_0. To ensure that the reference trajectory meets the initial and final conditions on the velocities, even in case of small errors between the nominal steady descent velocities and the actual values, when the helicopter reaches h_0 and the control logic switches from steady descent to flare controller, the actual initial velocities u_0 and w_0 are saved and used to calculate the reference velocity profile for the maneuver.

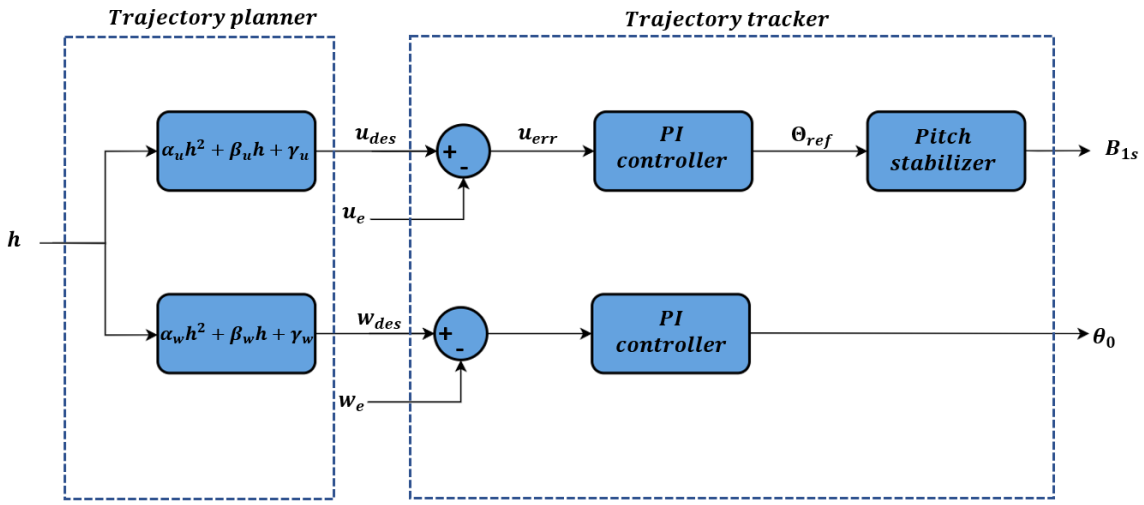

Figure 4.5: Flare controller

Chapter 5

Non-linear dynamic inversion control

5.1 Non-linear dynamic inversion control theory

Part of the project work has been dedicated to the study and implementation of advanced control techniques for the helicopter in both powered flight and autorotation conditions. A particular interest has been put in the nonlinear dynamic inversion control NDI, which is generally classified among the control allocation techniques.

The complete NDI controller architecture is reported in Fig. 5.1. Here the outer loop (velocity controller) generates the desired attitude and collective pitch. The former is sent to the inner loop which generates the necessary command action to the plant. The nonlinear dynamic inversion is a control technique based on the idea that it is possible to control a system by imposing a reference dynamic and inverting the equations of motion of the system in order to follow that dynamic. A brief description of the main algorithm is here reported. Let's consider the dynamic

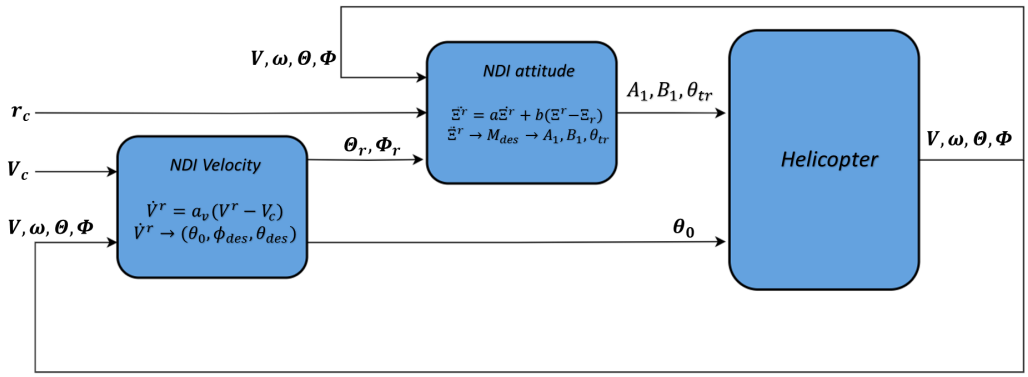

Figure 5.1: NDI global control architecture

equations of a generic system:

$$\begin{cases} \dot{x} &= f(x,u) \\ y &= g(x) \end{cases} \tag{5.1}$$

and a model of the same system, affected by uncertainties $\Delta\cdot$ assumed to be small:

$$\begin{cases} \dot{x}_m &= f_m(x,u) &= f(x,u) + \Delta f \\ y_m &= g_m(x) &= g(x) + \Delta g \end{cases} \tag{5.2}$$

If a reference output $y_r(t)$, and its reference dynamics $\dot{y}_r(t)$, $\ddot{y}_r(t)$, ... want to be followed, the necessay command action $u(x)$ can be obtained inverting the model dynamics. The first step is to derive the output until an explicit dependency on u appears. The number of the needed derivations r is the degree of the output w.r.t the input and represents the output time derivative which can directly be commanded.

Let's consider a first-degree $r = 1$ case, for simplicity. We will have:

$$\begin{cases} \dot{y} &= g'(x)\,\dot{x} &= g'(x)\; f(x,u) \\ \dot{y}_m &= g'_m(x)\,\dot{x}_m &= g'_m(x)\; f_m(x,u) \end{cases} \tag{5.3}$$

with $g'(x) \neq 0$ and $g'_m(x) \neq 0$. For $r = 1$ we will be able to directly command the output first-order time derivative. Thus a first-order reference dynamics need to be considered. Usually, the reference dynamics is linear and stable:

$$\dot{y}_r = -a\,(y_r - y_c) \tag{5.4}$$

where y_c is the commanded output and $a > 0$ is an imposed stiffness factor.

Now, calling pseudo-control the term $\nu = \dot{y}_r$, and imposing $\dot{y}_m = \dot{y}_r = \nu$ we can invert the dynamic equation of the model obtaining:

$$u = f_m^{-1}\left(g_m^{-1}(\nu)\right) \tag{5.5}$$

Giving this input to the output dynamics in Eq. (5.3) we have:

$$\begin{cases} \dot{y} &= \nu + \Delta &= \dot{y}_r + \Delta \\ \dot{y}_m &= \nu &= \dot{y}_r \end{cases} \tag{5.6}$$

The model system follows the desired output, while the real plant output is affected by an error Δ. Defining the output error as $e = y_r - y$, the error dynamics

is:

$$\dot{e} = \Delta \tag{5.7}$$

The stability of this error dynamics is not guaranteed since it depends on the accuracy of the model and the value of $\frac{\partial \Delta}{\partial e}$ which is the eigenvalue of the system. It is possible to ensure the error dynamics stability by correcting the pseudo control. A desirable stable error dynamics can be obtained by adding terms that are proportional to the error and its time derivatives until the $(r-1)$th. An integrative term is also usually added:

$$\dot{e} = \Delta + p_e\, e + i_e \int_0^\tau e dt \tag{5.8}$$

To obtain such a corrected error dynamics, a correction on the pseudo-control is added:

$$\nu = y_r + p_e\, e + i_e \int_0^\tau e dt \tag{5.9}$$

The right choice of the control parameters p_e, i_e and a feasible reference dynamics (through the choice of a) ensure the stability and a good control of the system.

5.2 Static estimation of the flapping angles

For the dynamic inversion of the helicopter model, most of the system state variables should be known during the flight. While linear and angular velocities, as the Euler angles, can be directly measured or estimated with integrated filters of the sensors unit which the rotorcraft is commonly equipped with, other inner variables need custom algorithms to be estimated during the flight. Between these variables, we have the flapping angles and the inflow ratio. For the flapping angles, a static estimation is

adopted here. Considering the time-scale separation between the flapping dynamics and the attitude and velocity dynamics, especially in the case of a hinge-less small-scale helicopter, a negligible effect is assumed for the time derivatives of the flapping coefficients and a steady state solution a_{ss} of Eq. (2.62) is calculated to estimate the flapping coefficients:

$$a_{ss} = K^{-1} f \tag{5.10}$$

The flapping coefficients are then a static function of the commands. It is useful for the NDI, also the calculation of

$$\frac{\partial a_{ss}}{\partial u_{att}} = K^{-1} f_{u_{att}} \tag{5.11}$$

where $u_{att} = [A_{1s};\, B_{1s};\, \theta_{tr}]$ and $f_{u_{att}}$ defined as:

$$f_{u_{att}} = \begin{bmatrix} f_{A_{1s}} & f_{B_{1s}} & f_{\theta_{tr}} \end{bmatrix} = \begin{bmatrix} \frac{\partial f_1}{\partial A_{1s}} & \frac{\partial f_1}{\partial B_{1s}} & 0 \\ \frac{\partial f_2}{\partial A_{1s}} & \frac{\partial f_2}{\partial B_{1s}} & 0 \\ \frac{\partial f_3}{\partial A_{1s}} & \frac{\partial f_3}{\partial B_{1s}} & 0 \end{bmatrix} \tag{5.12}$$

$$f_{u_{att}} = \Omega^2 \begin{bmatrix} \frac{\chi\gamma\mu\sin\beta_w\left(\frac{\varepsilon}{2}-\frac{1}{3}\right)}{2} & \frac{\gamma\mu\cos\beta_w\left(\frac{\varepsilon}{2}-\frac{1}{3}\right)}{2} & 0 \\ \frac{\chi\gamma\cos\beta_w}{2}\left(\frac{\mu^2}{4}\left(\frac{\varepsilon^2}{2}-\varepsilon+\frac{1}{2}\right)-\frac{\varepsilon}{3}+\frac{1}{4}\right) & -\frac{\gamma\sin\beta_w}{2}\left(\frac{\mu^2}{4}\left(\frac{\varepsilon^2}{2}-\varepsilon+\frac{1}{2}\right)-\frac{\varepsilon}{3}+\frac{1}{4}\right) & 0 \\ \frac{\chi\gamma\sin\beta_w}{2}\left(\frac{3\mu^2}{4}\left(\frac{\varepsilon^2}{2}-\varepsilon+\frac{1}{2}\right)-\frac{\varepsilon}{3}+\frac{1}{4}\right) & \frac{\gamma\cos\beta_w}{2}\left(\frac{3\mu^2}{4}\left(\frac{\varepsilon^2}{2}-\varepsilon+\frac{1}{2}\right)-\frac{\varepsilon}{3}+\frac{1}{4}\right) & 0 \end{bmatrix} \tag{5.13}$$

5.3 Extended Kalman filter for the inflow estimation

For the implementation of a non-linear dynamic inversion control, the inflow ratio, as the flapping angles, needs to be estimated. For this purpose, an extended Kalman filter is adopted here. The dynamics of the inflow is given by Eq. (2.72) where the actual C_t can be calculated from the thrust, which is in turn estimated as:

$$\hat{T} \approx ||m\left(a_{e,m} - g\right) - \hat{F}_{tr}|| \tag{5.14}$$

where $\hat{F}_{tr}$ is a model-based estimation of the tail rotor force and $a_{e,m}$ is the measured acceleration of the helicopter. The filter consists of two steps:

Time propagation: prediction

$$\hat{x}_{k+1}^{-} = \Phi_k \hat{x}_k \tag{5.15}$$

$$P_{k+1}^{-} = \Phi_k P_k \Phi_k^t + Q \tag{5.16}$$

Measurement update: correction

$$K_k = P_k^{-} H_k^t \left(H_k P_k^{-} H_k^t + R\right)^{-1} \tag{5.17}$$

$$\hat{x}_k = \hat{x}_k^{-} + K_k \left(z_k - H_k \hat{x_k}^{-}\right) \tag{5.18}$$

$$P_k = \left(1 - K_k H_k\right) P_k^{-} \tag{5.19}$$

where

$$\Phi_k = 1 + \left(\frac{df_{\lambda_i}}{d\lambda_i}\right)_k \Delta t \tag{5.20}$$

is the transition matrix, $H_k = 1$ is the measurement matrix, P is the error covariance matrix, and Q, and R are the process and measurement matrices respectively. The measure z_k is a fictitious measure obtained inverting the simplified thrust model of Eq. (3.26) where the value of the thrust is calculated as in Eq. (5.14) while the collective, the vertical velocity in hub frame and the rotor speed are known/measured.

$$\hat{\lambda} = \frac{1+3\mu^2/2}{1-\mu^2/2}\left\{\frac{4\hat{T}}{\rho\sigma A(\Omega R)^2\, Cl_\alpha} - \frac{2}{3}\theta_0\,\frac{1-\mu^2+9\mu^4/4}{1+3\mu^2/2}\right\} \tag{5.21}$$

$$z = \lambda_i = \frac{w_h}{\Omega\, R} - \hat{\lambda} \tag{5.22}$$

5.4 Attitude control with NDI

For the helicopter attitude controller, the output we want to command is given by the roll and pitch angles, and the yawrate. We consider the rotational dynamics and kinematics equations to obtain the output dynamics:

$$\begin{cases} \dot{\omega}_b = I^{-1}\left(M_b\left(x, u_{att}\right) - \omega_b \times \left(I\,\omega_b\right)\right) \\ \dot{\Xi} = R\omega_b \end{cases} \tag{5.23}$$

Deriving the second equation and substituting the first one, we find an explicit relation between $\ddot{\Xi}$ and the input vector for the attitude control $u_{att} = [A_{1s};\, B_{1s};\, \theta_{tr}]$

$$\ddot{\Xi} = \dot{R}\,\omega_b + R\,\dot{\omega}_b = \dot{R}\,\omega_b + R\,I^{-1}\left(M_b\left(x, u_{att}\right) - \omega_b \times \left(I\,\omega_b\right)\right) \tag{5.24}$$

Now, a second order reference linear dynamics is chosen for the roll and pitch, while a first-order reference dynamics is sufficient for the yaw rate:

$$\ddot{\Xi}_r = \begin{pmatrix} \ddot{\phi}_r \\ \ddot{\theta}_r \\ \ddot{\psi} \end{pmatrix} = \begin{pmatrix} -2\,\xi_\phi \omega_\phi \dot{\phi}_r + \omega_\phi^2\,(\phi_c - \phi_r) \\ -2\,\xi_\theta \omega_\theta \dot{\theta}_r + \omega_\theta^2\,(\theta_c - \theta_r) \\ \frac{1}{\tau_\psi}\left(\dot{\psi}_c - \dot{\psi}_r\right) \end{pmatrix} \tag{5.25}$$

where ω_ϕ, ξ_ϕ, ω_θ, ξ_θ, τ_ψ are gains to be properly tuned. The pseudo control is defined as:

$$\nu = \begin{pmatrix} \nu_\phi \\ \nu_\theta \\ \nu_\psi \end{pmatrix} = \begin{pmatrix} p_\phi\,(\phi_r - \phi) + d_\phi\left(\dot{\phi}_r - \dot{\phi}\right) + i_\phi \int_0^\tau (\phi_r - \phi)\,dt \\ p_\theta\,(\theta_r - \theta) + d_\theta\left(\dot{\theta}_r - \dot{\theta}\right) + i_\theta \int_0^\tau (\theta_r - \theta)\,dt \\ d_\psi\left(\dot{\psi}_r - \dot{\psi}\right) \end{pmatrix} \tag{5.26}$$

where a PID logic, with its tunable gains, is used to stabilize the error dynamics. It is possible to notice that no proportional and integral terms are used for the yaw since we are commanding a yaw rate.

Imposing $\ddot{\Xi} = \nu$ in Eq. (5.24) and inverting for M_b we obtain:

$$M_b^{des} = I\,R^{-1}\left(\nu - \dot{R}\,\omega_b\right) + \omega_b \times (I\,\omega_b) \tag{5.27}$$

To calculate $u_{att} = [A_{1s};\, B_{1s};\, \theta_{tr}]$ is now necessary to invert the expression of the total moment as given in Eq. (2.9) and reported below:

$$M_b^{des} = M_{b,mr} + M_{b,tr} + M_{b,f}$$

For the sake of control, a simplification can be made of the previous equation, lin-

earizing w.r.t the command vector u_{att}:

$$M_b^{des} \approx M_{b,0} + B\,\Delta u_{att} \tag{5.28}$$

where the effectiveness command matrix B is the jacobian of M_b w.r.t. u_{att}. Now, since the moment depends on the flapping angles in steady state $M_b = M_b(a_{ss}, u_{att})$ and $a_{ss} = a_{ss}(u_{att})$, to obtain B we need to consider even the matrix $f_{u_{att}}$ as defined in Eq. (5.12). So we have:

$$B = \begin{pmatrix} \frac{dM_b}{dA_{1s}} \\ \frac{dM_b}{dB_{1s}} \\ \frac{dM_b}{d\theta_{tr}} \end{pmatrix} = \begin{pmatrix} \frac{\partial M_b}{\partial A_{1s}} + \frac{\partial M_b}{\partial a_{ss}}\frac{\partial a_{ss}}{\partial A_{1s}} \\ \frac{\partial M_b}{\partial B_{1s}} + \frac{\partial M_b}{\partial a_{ss}}\frac{\partial a_{ss}}{\partial B_{1s}} \\ \frac{\partial M_b}{\partial \theta_{tr}} \end{pmatrix} = \frac{\partial M_b}{\partial u_{att}} + \frac{\partial M_b}{\partial a_{ss}} K^{-1} f_{u_{att}} \tag{5.29}$$

All the components of the matrix B have been calculated using the Matlab symbolic toolbox and implemented for the control. A schematic recap is reported below to understand how the command law is determined:

- the commanded/desired attitude ϕ_c, θ_c and yaw rate $\dot{\psi}_c$ are used to elaborate a reference dynamics $\ddot{\Xi}_r$ as in Eq. (5.25)
- the reference is used to generate the pseudo command ν in Eq. (5.26) which also control the error
- a desired moment is generated inverting the dynamic equation Eq. (5.27)
- comparing the desired moment to the estimated actual one $M_{b,0}$ we obtain the

command action

$$u_{att} = u_{att,0} + B^{-1}\left(M_b^{des} - M_{b,0}\right) \tag{5.30}$$

5.5 Velocity control with NDI

For the velocity control, a similar structure, with a simplified model, is considered. The velocity controller receives commanded velocities which must be used to generate a reference attitude for the inner loop controller and the collective pitch. So we have the commanded velocity in the local vertical frame $V_c = [V_x;\, V_y;\, V_z;]$ which is used to generate a reference first order dynamics:

$$\dot{V}_r = K_V\ (V_c - V) \tag{5.31}$$

with K_v matrix of the desired time constants

$$K_v = \begin{bmatrix} \frac{1}{\tau_x} & 0 & 0 \\ 0 & \frac{1}{\tau_y} & 0 \\ 0 & 0 & \frac{1}{\tau_z} \end{bmatrix} \tag{5.32}$$

The pseudo control vector is given by:

$$\nu = \dot{V}_r + P_v\, e_V + I_v \int_0^\tau e_V\, dt \tag{5.33}$$

where $e_V = V - V_r$ and P_v and I_v are the diagonal gain matrices. The dynamic equations to be inverted are obtained considering the folllwing low order system

written in the local vertical frame:

$$\begin{cases} \dot{V}_x &= \frac{1}{m}\left(T\sin i_s\cos\theta - T\cos i_s\cos\phi\sin\theta + \xi T_{tr}\sin\phi\sin\theta\right) \\ \dot{V}_y &= \frac{1}{m}\left(T\cos i_s\sin\phi + \xi T_{tr}\cos\phi\right) \\ \dot{V}_z &= g - \frac{1}{m}\left(T\sin i_s\sin\theta + T\cos i_s\cos\phi\cos\theta - \xi T_{tr}\sin\phi\cos\theta\right) \end{cases} \tag{5.34}$$

The previous system can be contracted in the vectorial form:

$$\dot{V} = g + \frac{F_{mr} + F_{tr}}{m} \tag{5.35}$$

A simplified model for the main rotor thrust (Eq. (3.26)) has been considered:

$$T = \rho\sigma A(\Omega R)^2\frac{Cl_\alpha}{4}\left\{\frac{2}{3}\theta_0\frac{1-\mu^2+9\mu^4/4}{1+3\mu^2/2} + \lambda\frac{1-\mu^2/2}{1+3\mu^2/2}\right\} \tag{5.36}$$

Putting $\dot{V} = \nu$ and neglecting the effect of the tail rotor, an estimation of the main rotor thrust can be evaluated from the previous equation as:

$$\hat{T} \approx ||F_{mr}|| \approx m||\nu - g|| \tag{5.37}$$

the estimated value of the thrust can be now used to invert the thrust model obtaining the collective pitch:

$$\theta_0 = \frac{3}{2}\left(\frac{1+3\mu^2/2}{1-\mu^2+9\mu^2/4}\right)\left\{\frac{4\,\hat{T}}{\rho\,\sigma\,A\,(\Omega\,R)^2\,C_{l_\alpha}} - \lambda\frac{1-\mu^2/2}{1+3\mu^2/2}\right\} \tag{5.38}$$

From the first equation of the dynamic system Eq. 5.34, under the hypothesis of

small attitude angles, and again putting $\dot{V} = \nu$ we obtain the desired roll angle:

$$\phi_{des} = \frac{m\nu_y + \hat{T}_{tr}}{\hat{T}\cos\imath_s} \tag{5.39}$$

where $\hat{T}_{tr}$ is an estimation of the tail rotor which can be done with simple models as the one proposed in Ref. [7]. Finally, rewriting the first line of Eq. (5.34) in the body frame we can obtain the desired pitch angle:

$$\theta_{des} = \frac{\hat{T}\sin i_s - m\nu_x}{m\left(g - \nu_z\right)} \tag{5.40}$$

5.6 Automatic autorotation with NDI

The NDI controller has also been texted for autorotation. The maneuver is designed as in chapter 3. The control logic changes when the system passes from the normal flight to the autorotation. Even during the two phases of autorotation, the control logic is different. More in detail, during the steady descent phase, the nominal advancing velocity is followed by the NDI velocity controller, while the collective is calculated in order to control the angular rate instead of the vertical velocity. So, a constant low collective (resulting from the trim) and then a PI logic on the rotor rate error are used to generate a collective to keep the angular rate nominal steady descent value. For the flare, the trajectory planner calculates the reference velocity which represents a command for the NDI velocity controller. For all the phases the NDI attitude controller receives reference pitch and roll angles from the velocity controller.

Chapter 6

Numerical results

6.1 Helicopter model validation

The mathematical model of the helicopter dynamics has been numerically validated. A static validation of the helicopter model has been performed by comparing the trim curves related to the model described in chapter 2, and the simulation results of a higher-order model implemented in Flightlab, and available from the literature [43]. The small-scale helicopter Align T-REX has been considered for the sake of trim validation, and relevant parameters within the model. Main results are depicted in Figs. 6.1-6.3, showing pilot inputs, roll and pitch angles. Results show a good agreement. A summary of trim variables error is reported in Tab. 6.1 for each trim curve (V_N, V_{up}, V_E). Here, the errors on the roll and pitch angles are the maximum absolute errors, while the error considered for the inputs is normalized on every input

range:

$$\%e_{\theta_0} = \frac{|\theta_{0,FL} - \theta_{0,M}|_{max}}{\Delta\theta_0} \cdot 100 \quad (6.1)$$

$$\%e_{\theta_{tr}} = \frac{|\theta_{tr,FL} - \theta_{tr,M}|_{max}}{\Delta\theta_{tr}} \cdot 100 \quad (6.2)$$

$$\%e_{\theta_0} = \frac{|A_{1s,FL} - A_{1s,M}|_{max}}{\Delta A_{1s}} \cdot 100 \quad (6.3)$$

$$\%e_{\theta_0} = \frac{|B_{1s,FL} - B_{1s,M}|_{max}}{\Delta B_{1s}} \cdot 100 \quad (6.4)$$

where M stands for model and FL for Flightlab. Small errors are obtained for the most important variables, namely the roll and pitch angles, and the collectives. Slightly bigger but acceptable are the errors on the cyclic commands which are due to the difficulties related to the dynamic modeling of the internal main rotor dynamics (flapping and inflow dynamics). These errors don't prevent a good description of the main dynamic behavior of the helicopter and have a reduced importance when the model is used for guidance, navigation and control systems design.

6.2 Autorotation results

This section addresses the main results of the complete automatic autorotation maneuver. The designed maneuver has been simulated by means of the complete helicopter model described in chapter 2 with the controllers seen in chapter 4. The main helicopter parameters for the Goblin Saab 700 used here, can be found in Tab. 6.2. Several simulations have been performed. For all of them, the following assumptions have been considered:

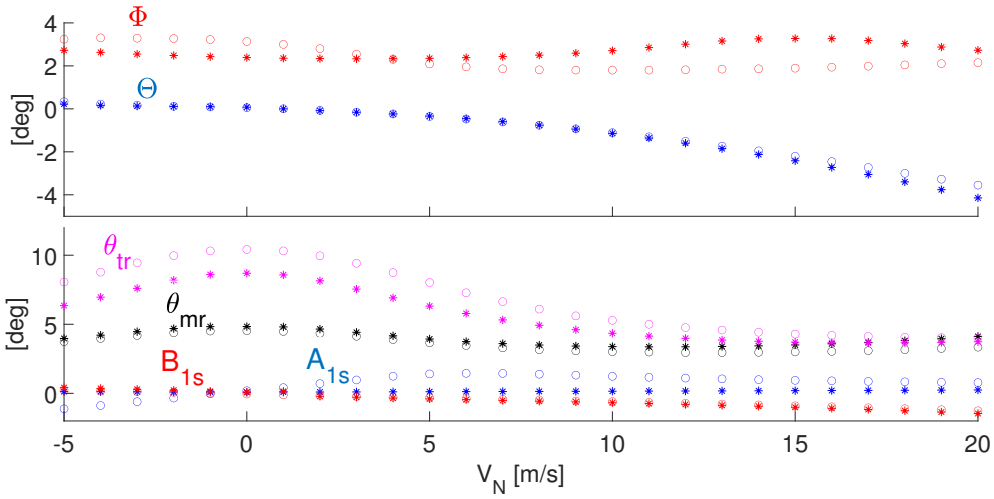

Figure 6.1: Trim results comparison for different advancing velocities.
$\circ$ = Model, $*$ = Flightlab

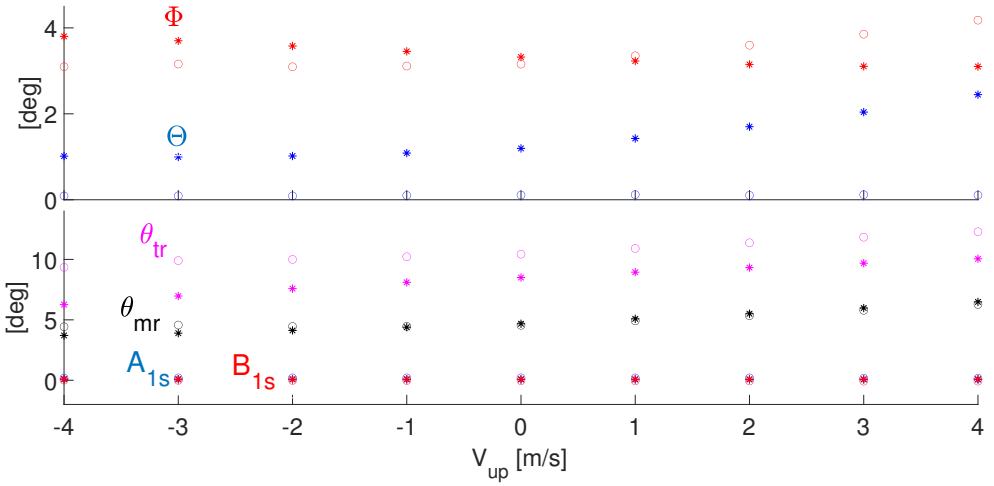

Figure 6.2: Trim results comparison for different vertical velocities.
$\circ$ = Model, $*$ = Flightlab

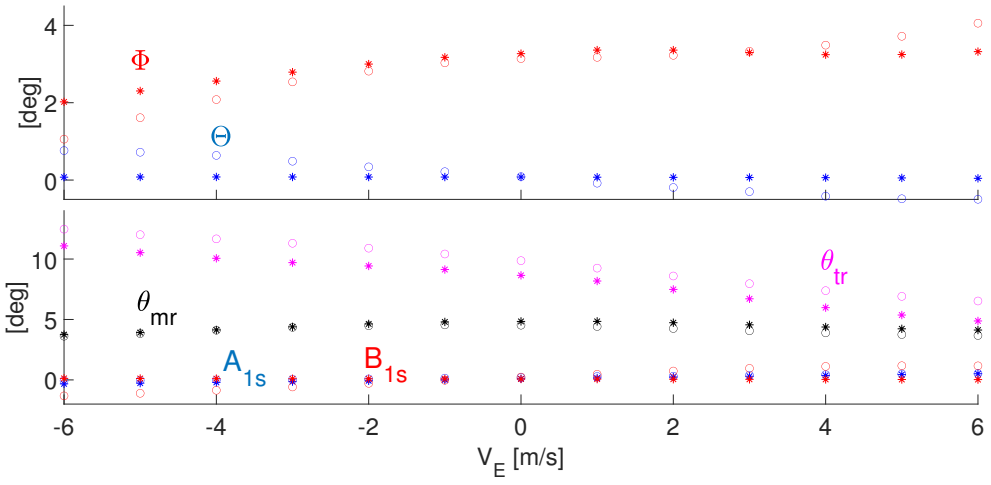

Figure 6.3: Trim results comparison for different lateral velocities.
$\circ$ = Model, $*$ = Flightlab

Table 6.1: Maximum trim errors

Maximum errors on roll and pitch angles deg

	V_N	V_{up}	V_E
Φ	0.59	2.33	0.68
Θ	0.64	0.38	2.26

Maximum normalized errors on trim commands %

	V_N	V_{up}	V_E
θ_0	6.45	5.98	4.12
θ_{tr}	3.12	5.15	2.75
A_{1s}	14.75	1.35	2.82
B_{1s}	2.83	1.81	16.06

- unlimited extended landing field and no constraints on the final position;
- engine failure happens after 2 s of a stable forward flight;
- the control system recognizes the engine failure and starts the autorotation when $\Omega < \Omega_{decision}$ which is set to 95% of the value for the nominal condition.

The optimal flare parameters are obtained from the flare optimization and are reported in Tab. 3.1. The nominal initial condition is a forward flight with initial velocity $u_i = u_0$, initial altitude $h_i = 100$ m, and rotor angular rate $\Omega_i = \Omega_0$. The simulation campaign addressed the following main tasks:

- test the optimized automatic autorotation in nominal conditions;
- test the influence of the flare altitude on the maneuver;
- compare simulations done at different initial altitudes, different initial cruise velocities, and different initial rotor angular rates.
- check the robustness of guidance and control law against model parametric uncertainties

All the controller gains, reported in Tab. 6.3 have been chosen by trial and error.

6.2.1 Results for nominal initial conditions

The first simulation is conducted considering an initial altitude of 100 m and an initial velocity equal to that allowing the steady descent u_0. Steady descent velocities and the flare altitude h_0 are provided by Tab. 3.1. In Fig. 6.4-6.6, the simulation results

Table 6.2: Helicopter data

Inertial parameters			
Parameter	Symbol	Value	Unit
Mass	m	4.8	kg
Moments of inertia	I_{xx}	0.0465	kg/m^2
	I_{yy}	0.2971	kg/m^2
	I_{zz}	0.2567	kg/m^2
Products of inertia	I_{xy}	0.0079	kg/m^2
	I_{xz}	0.0033	kg/m^2
	I_{yz}	-0.0006	kg/m^2
Main rotor			
Parameter	Symbol	Value	Unit
Rotor direction	χ	-1	—
Rotor radius	R	0.79	m
Rotor inertia	I_{mr}	0.0689	kg/m^2
Number of blades	N_b	2	—
Hinge offest ratio	ε	0.0314	—
Profile lift slope	C_{l_α}	2π	—
Profile chord	c	0.06	m
Blade mass	m_b	0.2057	kg
Blade flapping inertia	I_β	0.0344	kg/m^2
Equivalent rotor hinge stiffness	K_β	162.69	Nm/rad
Pitch-flap coupling ratio	K_1	0	—
Linear blade twist	θ_t	0	rad/m
Solidity	σ	0.0479	—
Rotor forward tilt angle	i_s	0.0524	rad
Precone	a_0	0	rad
Hub position in body axes	x_h	0.0095	m
	y_h	0	m
	z_h	-0.1810	m
Tail rotor			
Parameter	Symbol	Value	Unit
Rotor	R_{tr}	0.115	m
Rotor inertia	I_{mr}	0.0689	kg/m^2
Number of blades	$N_{b,tr}$	2	—
Solidity	σ_{tr}	0.1716	—
Hub position in body axes	x_{tr}	-1.045	m
	y_{tr}	0.052	m
	z_{tr}	-0.031	m

Table 6.3: Controllers gains

Roll stabilizer gains	value	unit
P_Φ	2π	$1/s$
P_p	$7.1628e-3$	—
I_p	$5.3721e-4$	—
D_p	0	—
K_{pq}	$-3.50e-1$	—
Pitch stabilizer gains	**value**	**unit**
P_Θ	2π	$1/s$
P_q	$8.3409e-3$	—
I_q	$6.2556e-4$	—
D_q	0	—
K_{qp}	$1e-3$	—
Heading hold gains	**value**	**unit**
P_Ψ	5.01	$1/s$
P_r	$6.70e-2$	—
I_r	$1.411e-3$	—
P_{θ_0}	$2.0614e1$	—
$\theta_{0,tr}$	$8.590e-2$	rad
Steady descent control gains	**value**	**unit**
P_u	$-6.3662e-1$	—
I_u	$-1.2732e-2$	—
D_u	$1.2732e-2$	—
P_v	$-6.3662e-1$	—
I_v	$1.2732e-2$	—
D_v	$1.2732e-2$	—
P_Ω	$-9.00e-3$	—
I_Ω	$-5.00e-4$	—
Flare control gains	**value**	**unit**
P_w	$8.00e-1$	—
I_w	$2e-2$	—
D_w	0	—

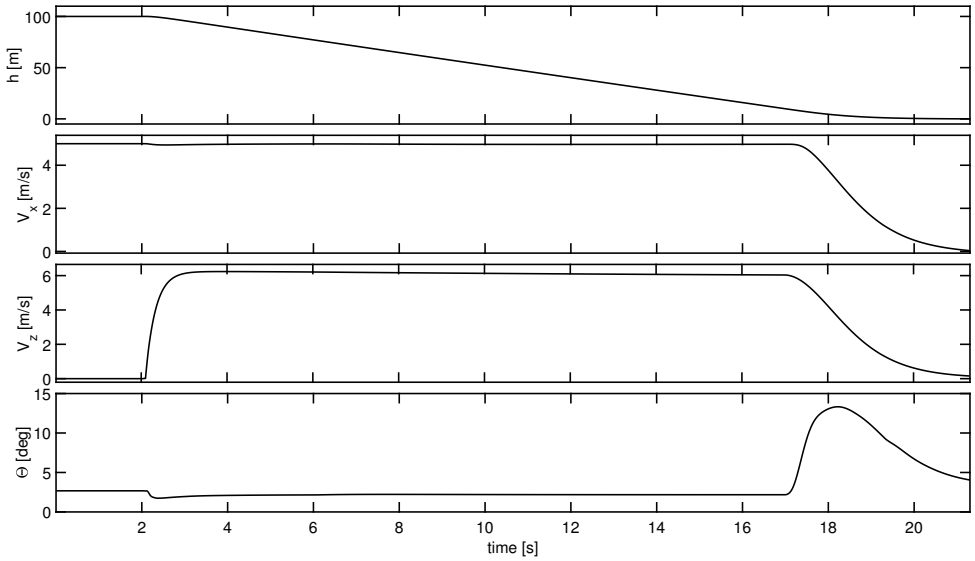

Figure 6.4: Nominal autorotation maneuver: longitudinal variables

are reported. After 2 s of level flight, the engine fails, the rotor rate decreases, and the helicopter follows a descent trajectory. The collective pitch input in Fig. 6.6 is set to the steady descent trim value and the control system allows the rotor speed to reach the target steady descent conditions. At $t \approx 17$ s, when the helicopter reaches the flare altitude h_0, the flare phase starts: the collective pitch increases exploiting the rotor energy to decelerate the helicopter, and around the pitch axis, a smooth pull-up input reduces the advancing velocity. At touch down, velocities and attitude are below the desired limits, and the maneuver is considered concluded successfully. It's clear from Fig. 6.5 that lateral-directional variables are controlled by roll and yaw autopilots to obtain a quasi-purely longitudinal maneuver. Fig. 6.7 shows the exact tracking of the velocity during the flare.

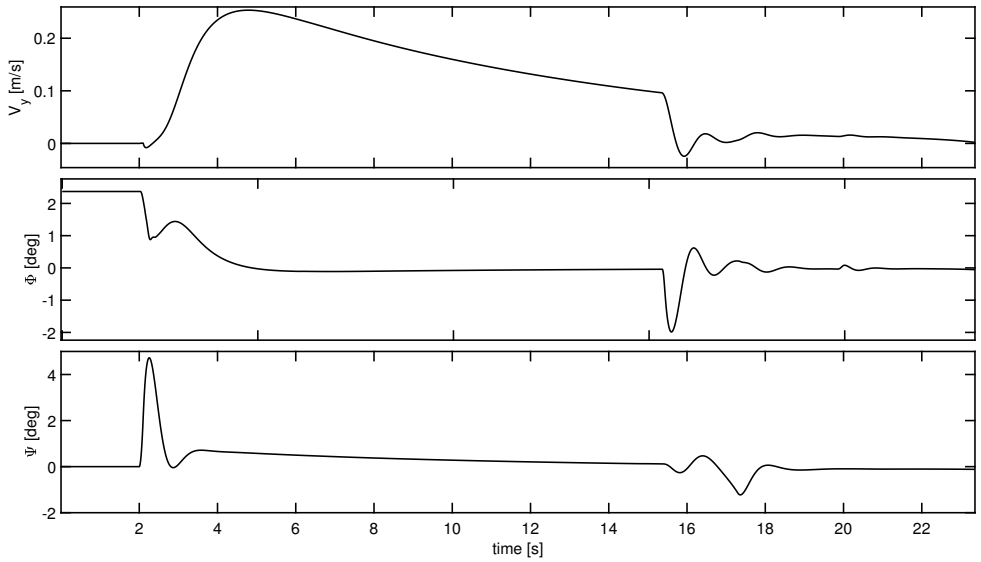

Figure 6.5: Nominal autorotation maneuver: lateral variables

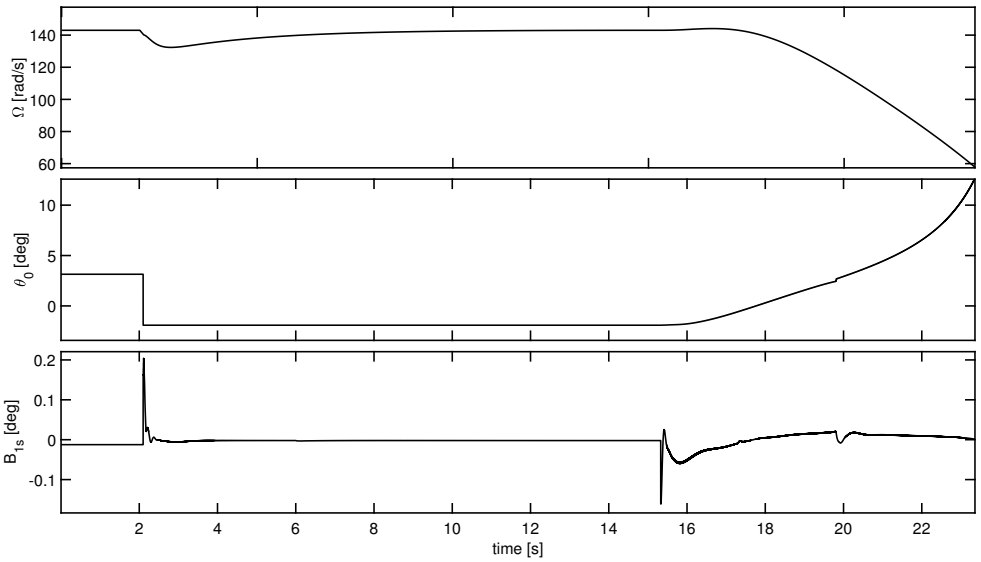

Figure 6.6: Nominal autorotation maneuver: main rotor angular rate and main commands

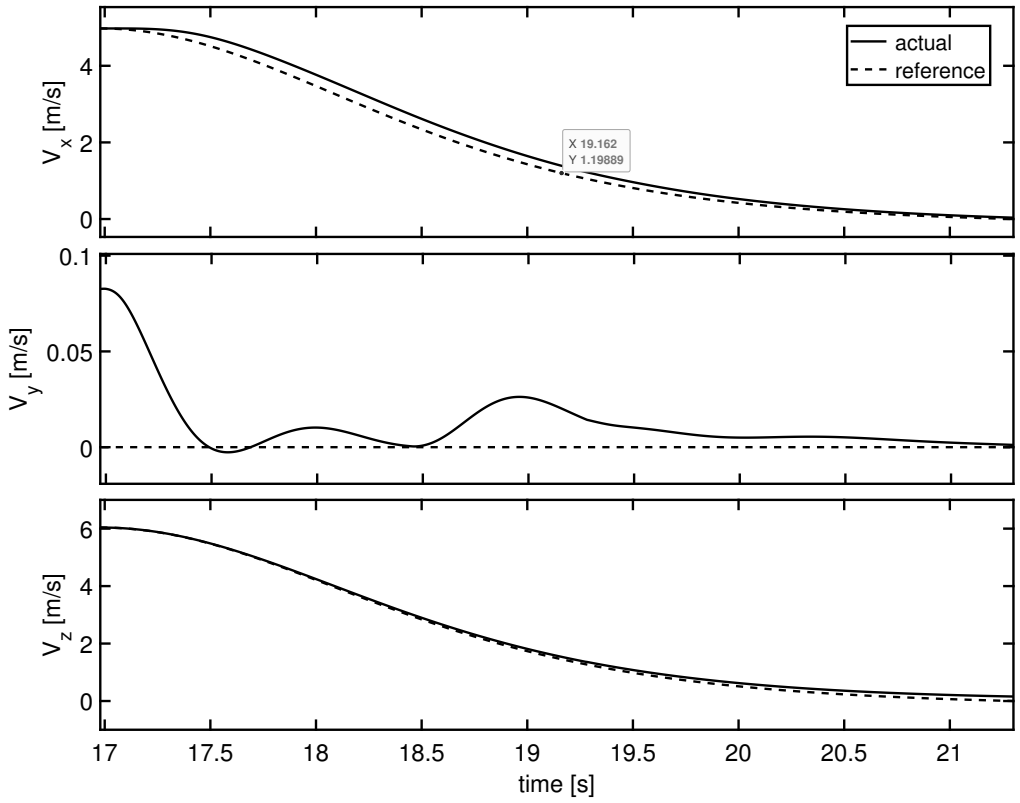

Figure 6.7: Nominal autorotation maneuver: velocity tracking during the flare

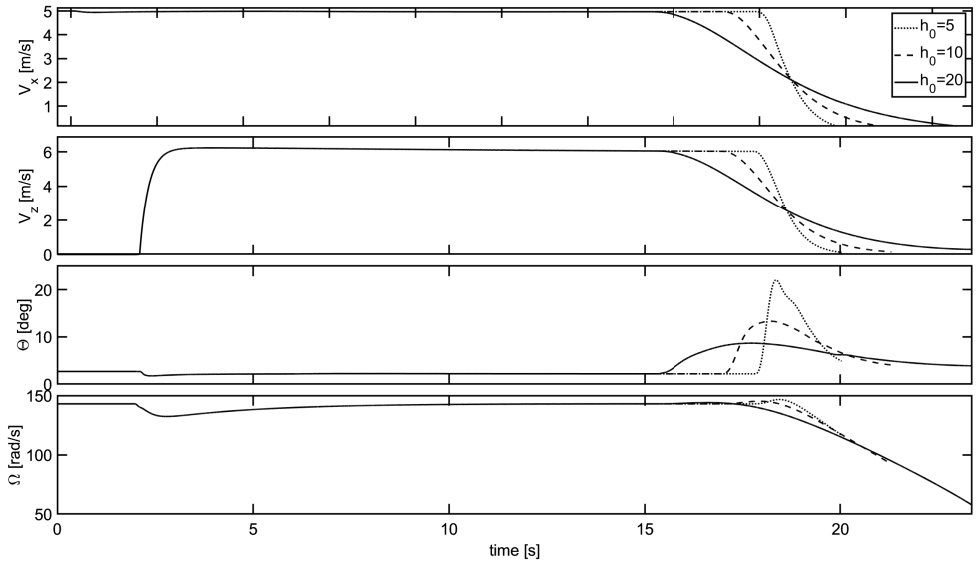

Figure 6.8: Autorotation for three different flare altitudes

6.2.2 Effect of different altitude for the flare

In Fig.6.8 it is shown what happens when, considering the nominal initial and steady descent conditions, different values of h_0 are adopted. What appears clearly is that the higher the flare altitude, the longer and smoother the maneuver. Then, increasing h_0 the maximum pull-up angle is reduced but also the rotor rate at touch-down reaches reduced values. It means that a lower limit on h_0 is imposed by the maximum pitch angle and pitch rate while a higher limit is given by the stall of the rotor. As expected, since the altitude stays between these two limits, there is no practical influence of h_0 on the final velocity. Optimization in section 3.5 is then useful to find optimal values of u_0 and w_0 and a suitable value of h_0.

6.2.3 Effect of different initial velocity and altitude

Two groups of simulations are conducted in order to test the robustness of the maneuver over the initial level flight conditions. Different initial velocities and altitudes are then considered.

The effect of the initial advancing velocity on the autorotation maneuver is reported in Fig. 6.9. Three different values of u_i are chosen. In every case, since u_i is not so far from the steady descent value, the helicopter can get the steady descent conditions and then correctly perform the flare. The effect of the pitch angle on the first phase of the maneuver (when the helicopter passes from u_i to u_0) produces a slight shift between the vertical velocity for the different cases, giving a slightly different time for the flare.

Different initial altitudes are instead considered for simulations reported in Fig. 6.10. Here it is possible to see that all the simulations have good results and it is clear that the lower the initial altitude, the shorter the steady descent phase. In particular, for $h_i = 15$ m this phase is practically absent.

6.2.4 Effect of different initial rotor angular rate

The effect of the initial rotor angular rate is investigated and reported in Fig. 6.11. Again the control system demonstrates the capability of getting the steady descent nominal angular rate, performing a good manoeuvre.

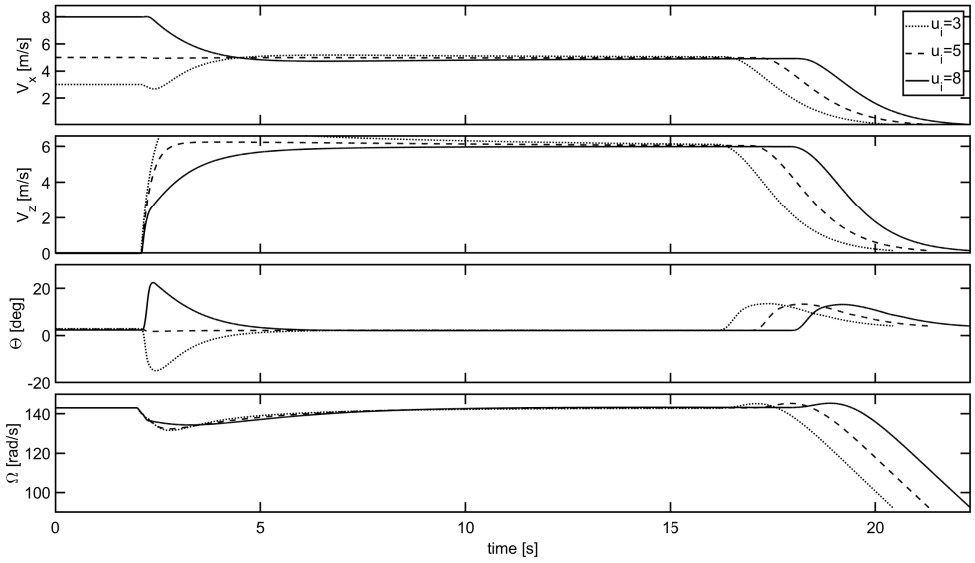

Figure 6.9: Autorotation for three different initial velocities

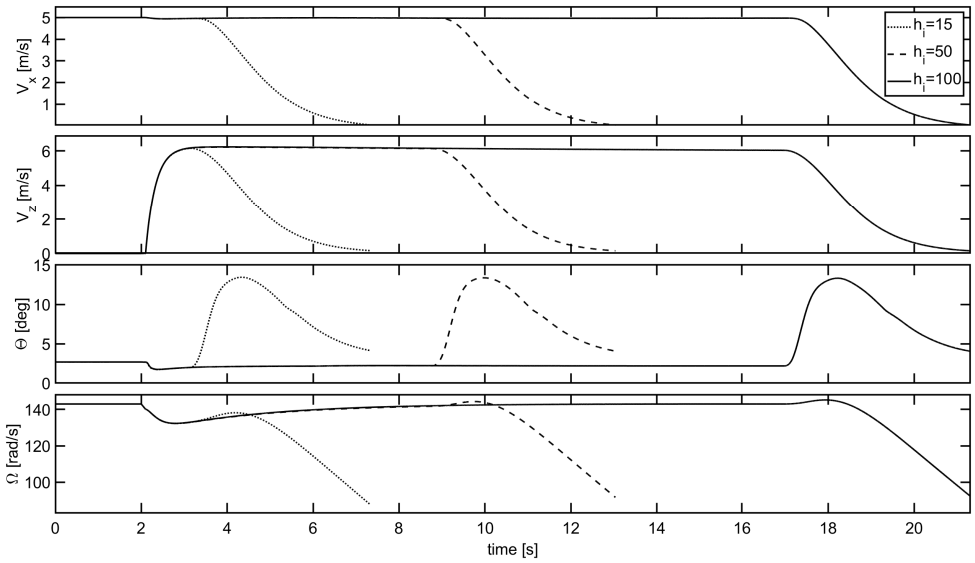

Figure 6.10: Autorotation for three different initial altitudes

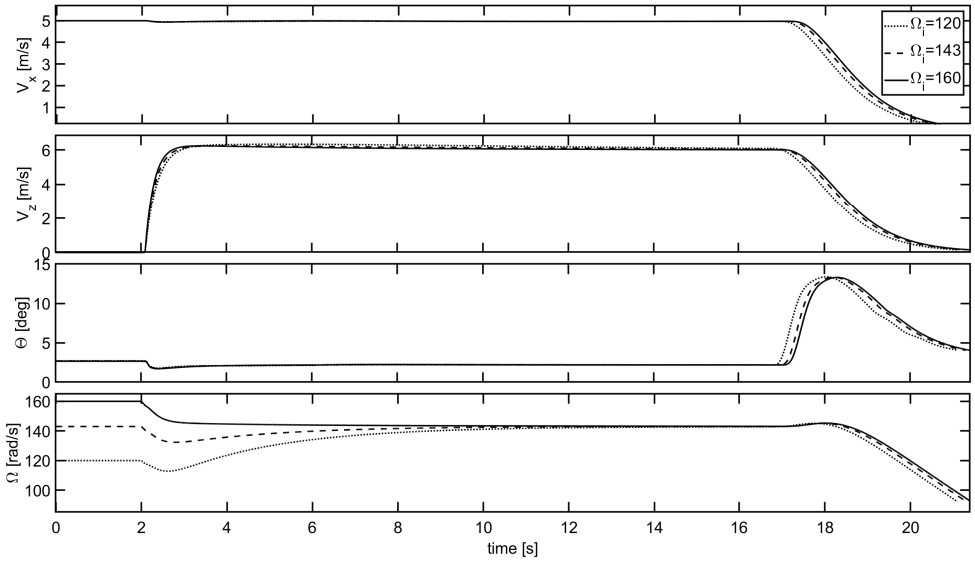

Figure 6.11: Autorotation for three different initial angular rates

6.2.5 Effect of parameters uncertainties and altitude sensor error

The robustness of the designed maneuver has been tested by conducting a Monte Carlo simulation campaign, where a normal distribution of random uncertainties on main helicopter parameters has been considered. The key parameters taken into account are:

- inertial parameters: total mass M_{tot}, inertia moment about the pitch axis I_{yy};
- aerodynamic parameters: main rotor blade lift slope C_{l_α}, blade parasite drag coefficient δ_0, fuselage drag coefficient C_D.

To enrich the simulation's meaningfulness, a random uncertainty on the measured altitude has also been introduced to test its effect on the final flare. The range of uncertainty, for every parameter, can be found in Tab. 6.4, while the results of the

500 simulations are reported in Tab. 6.5. The value of 0.1 m as maximum error on the measured altitude, is compatible with the accuracy of the most common Lidar sensors used for UAVs. The results refer to the touch-down conditions (velocity, attitude, and angular rate), the total time, the total range, and the maximum pitch angle during the flare. The most important result regards the touch-down velocity, which is under the threshold of acceptable values even in the worse conditions (maximum value of u_{td} and w_{td}). Acceptable values are obtained also for the Euler angles at touch-down and the maximum pitch angle during the flare. The low values of the standard deviation suggest the low influence of the parameters on the maneuver effectiveness. Slightly more variable results are obtained for the rotor angular rate. Preliminary simulation tests showed that the final velocity and angular rate are mostly affected by the error on the measured altitude, while a reduced effect is given by the other parameters. Analytic estimation of this error can be done by applying the small perturbation theory on Eq. (3.16). Deriving the latter w.r.t. the altitude we obtain:

$$\delta w_{td} = \left.\frac{\partial w(h)}{\partial h}\right|_{h=0} \delta h = \frac{2\, w_0}{h_0} \delta h \tag{6.5}$$

In our case, considering a maximum error on the measured altitude of 0.1m, we obtain a maximum variation on the final touch down velocity of 0.12 m/s which is approximately equal to the difference between the maximum and mean value of w_{td} in Tab. 6.5.

Table 6.4: Uncertainties ranges

Parameters	Symbol	Value	Unit
Mass	δM_{tot}	5	%
Pitch inertia	δI_{yy}	10	%
Blade lift slope	δC_{l_α}	10	%
Blade parasite drag	$\delta\delta_0$	10	%
Fuselage drag	δC_D	10	%
Measured altitude	δh	0.1	m

Table 6.5: Monte Carlo results

Symbol	Mean	Min	Max	St. deviation	Unit
t_f	20.338	18.748	22.073	0.62778	s
S_f	85.953	80.529	91.139	2.1737	m
u_{td}	0.117	-0.00076573	0.23998	0.066143	m/s
v_{td}	0.0029415	0.00012312	0.0061101	0.0014016	m/s
w_{td}	0.15632	0.070825	0.26801	0.057433	m/s
ϕ_{td}	-0.0087451	-0.046025	0.10858	0.014204	°
θ_{td}	4.017	3.4409	4.735	0.37321	°
θ_{max}	12.218	11.783	12.524	0.13227	°
ψ_{td}	0.55999	-1.4009	2.1083	0.55641	°
Ω_{td}	94.887	74.616	111.13	8.5593	rad/s

6.3 Simulations with NDI control

In the following subsections, the results for four different simulations performed with the NDI controllers are reported. A first test, for the NDI controller, was performed to investigate how the controller follows symmetrical step inputs on the desired velocity along the three local-vertical axes. A second simulation considers a circular maneuver to see how the system responds to a commanded constant yaw rate. As a third point, a lateral slalom maneuver is simulated for the lateral response and finally, the automatic autorotation is performed as a longitudinal maneuver. The velocity controller capabilities are tested by comparing the simulated velocities and attitudes with their corresponding reference/desired signals. Also, the extended Kalman filter behavior for the mean inflow angle estimation has been investigated during these simulations. All the simulation results reported in the following were obtained after an initialization phase where an advancing flight in steady condition is reached.

6.3.1 Response on step inputs

Starting from a steady level powered flight at $V_x = 5$ m/s, three symmetric step inputs with a magnitude of 1 m/s are given to the desired velocity along the three local-vertical axes, starting at time 2 s. The velocity response is given in Fig. 6.12, where it is shown that the simulated velocity correctly follows the reference dynamics reaching the commanded values after around 2 s. Looking at Fig. 6.13, it is possible to notice how the pitch and roll angles are connected respectively to the advancing and lateral velocity, and the good decoupling obtained between the longitudinal and lateral axes. A certain coupling is still present between the pitch and yaw axes. In

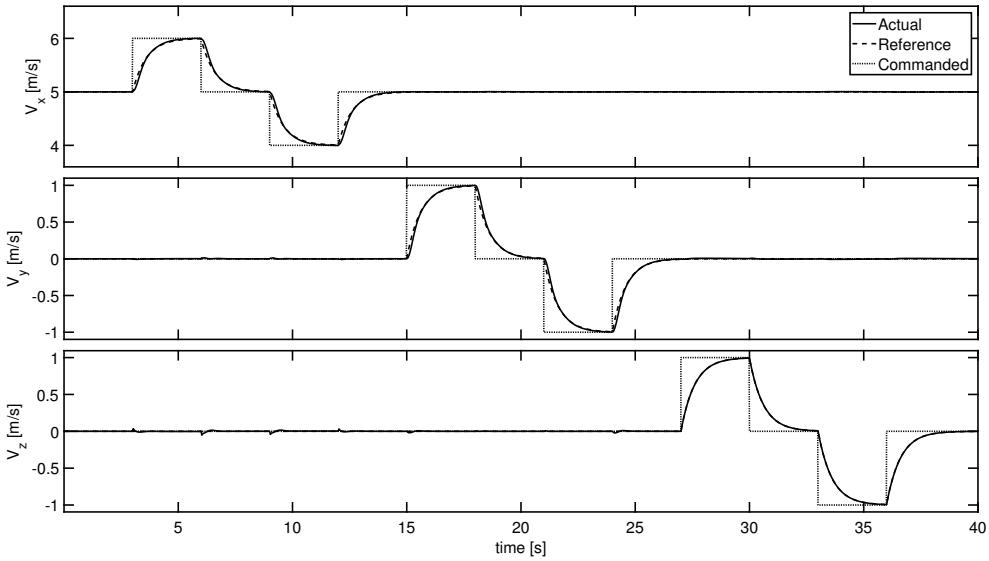

Figure 6.12: Velocity response for step input velocity with NDI control

Fig. 6.14 the behavior of the inflow estimation is reported: here it is visible how the filter manages to properly estimate the mean inflow keeping an error bounded under the 5% for all the simulation time.

6.3.2 Circular maneuver

A circular maneuver with a turn rate of 6 deg/s and a radius of 48 m has been commanded and simulated. During the simulation, the commanded yaw rate corresponds to the turn rate while an advancing constant velocity of 5 m/s is commanded to the x_{lv} axis. The results are shown in Fig. 6.15-6.18 where it is visible how the velocity controller, as the attitude controller and the yaw rate controller properly follow the reference signals. Even the inflow estimation error is small during all the simulation. Finally a comparison between the ideal desired circular trajectory and

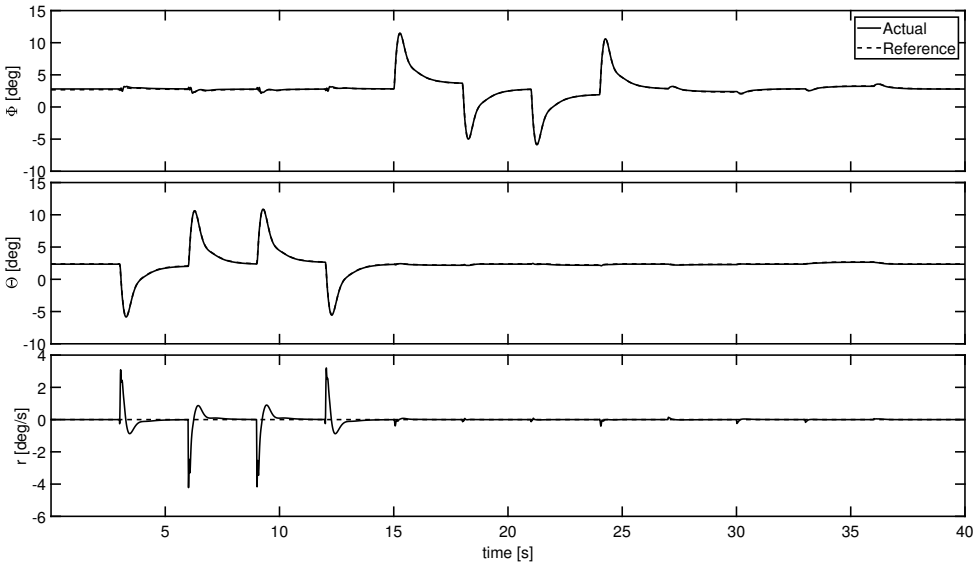

Figure 6.13: Attitude response for step input velocity with NDI control

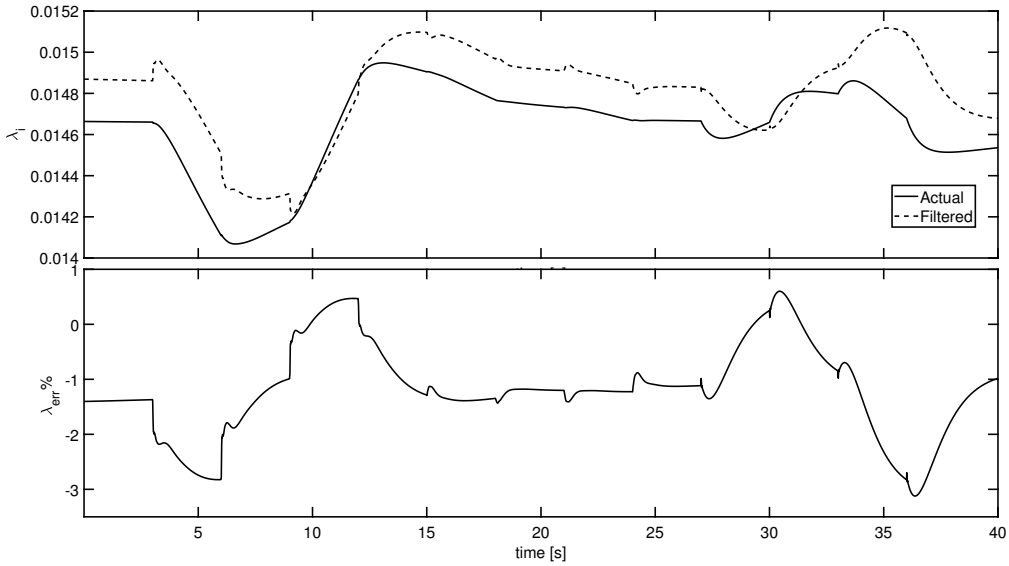

Figure 6.14: Inflow filter behavior for step input velocity with NDI control

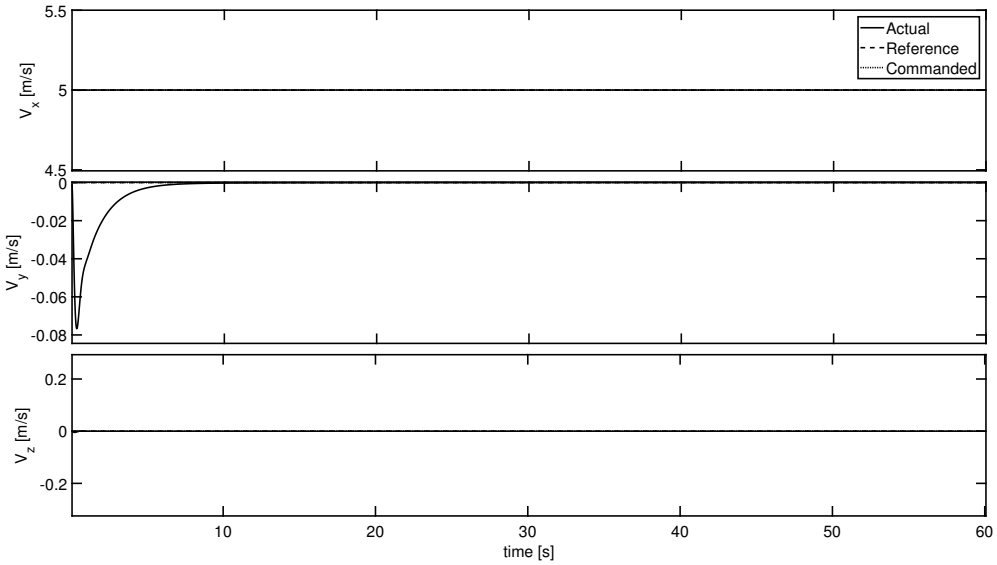

Figure 6.15: Velocities for a circular maneuver with NDI control

the obtained trajectory in Fig. 6.18 reveals the good performance of the controller.

6.3.3 Lateral maneuver

The simulation results for a slalom maneuver are reported in Figs. 6.20-6.20. In this simulation a constant velocity is commanded along the x_{lv} axis while a the desired lateral velocity has a sinusoidal time law. As can be seen in the plots, the system adequately follows the reference velocities and attitude. In particular, an oscillating roll angle (and a low amplitude oscillating pitch angle) are necessary for the velocity tracking. A neglegible yaw rate is also obtained. Again, a very good estimation of the inflow ratio is obtained and shown in Fig. 6.21.

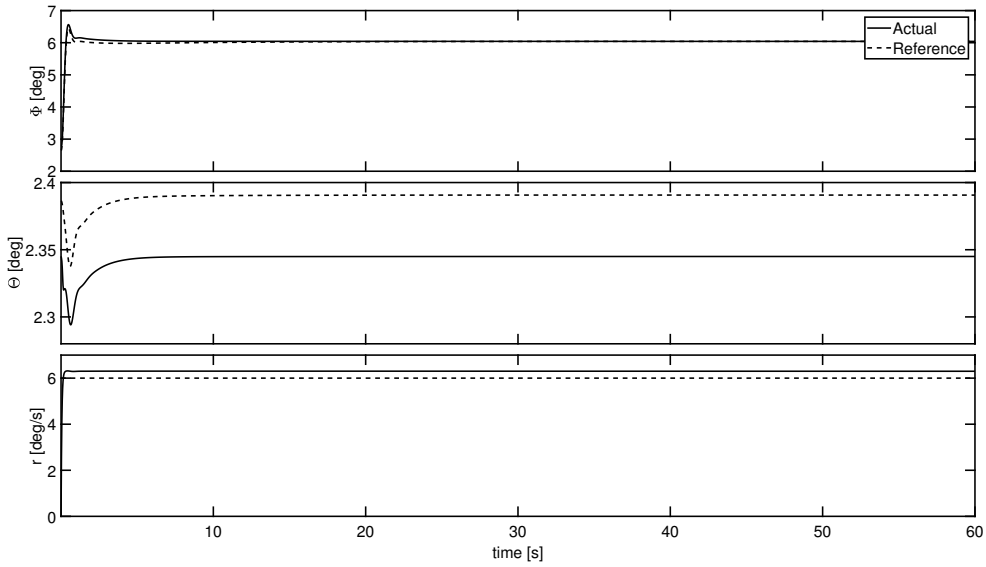

Figure 6.16: Euler angles and yawrate for a circular maneuver with NDI control

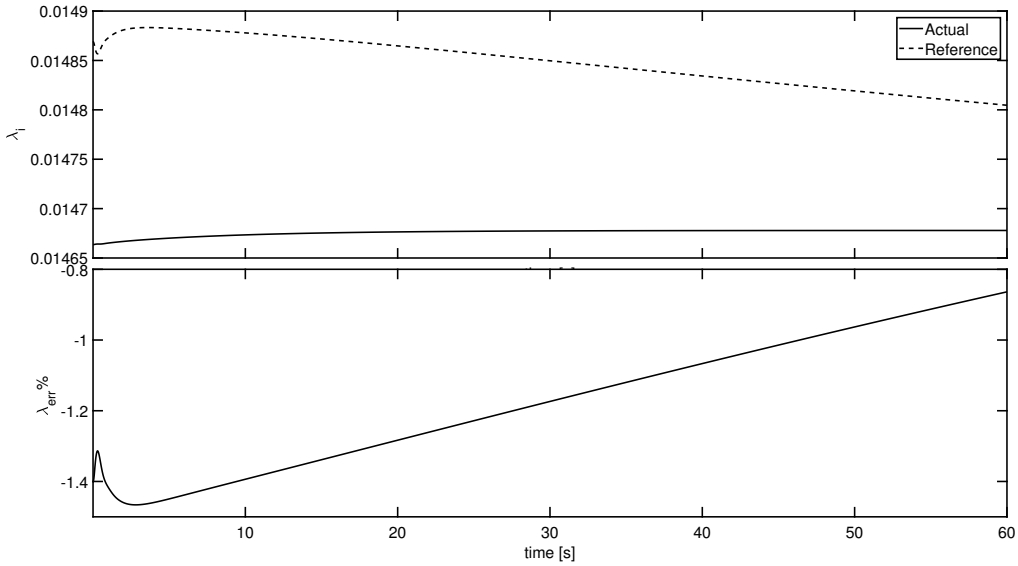

Figure 6.17: Inflwo filter behavior for a circular maneuver with NDI control

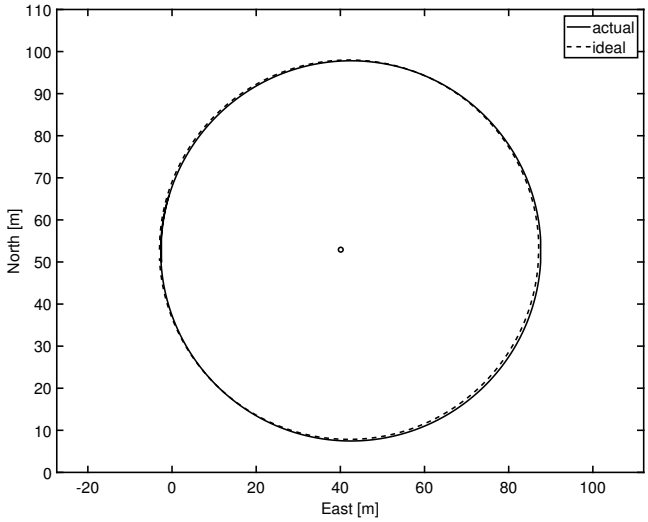

Figure 6.18: Trajectory for a circular maneuver with NDI control

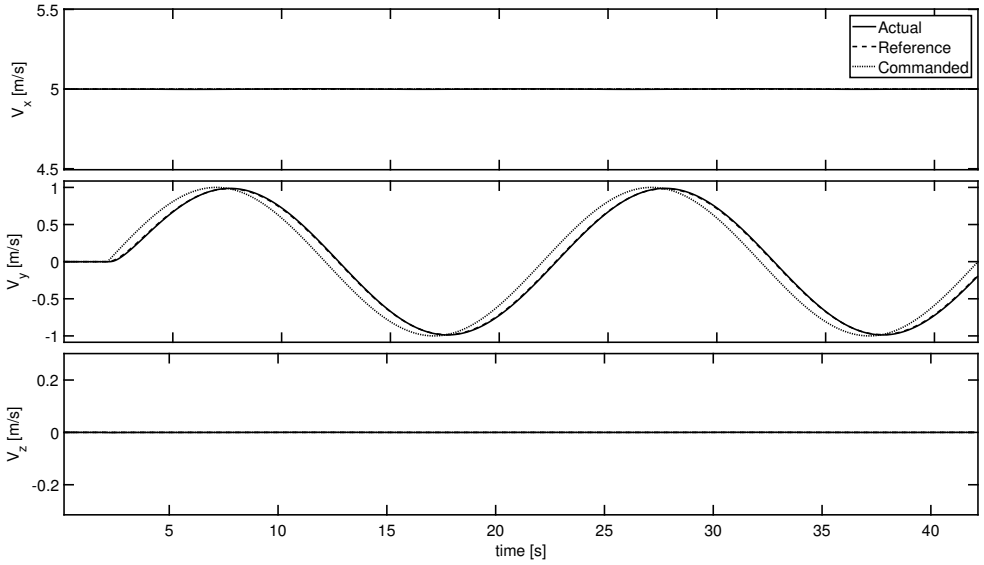

Figure 6.19: Velocities for a slalom maneuver with NDI control

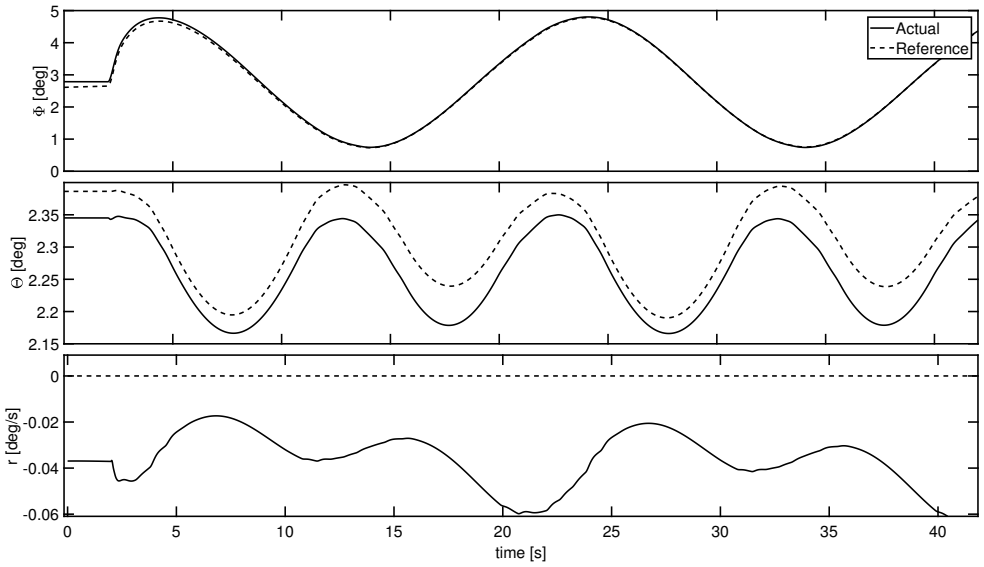

Figure 6.20: Euler angles and yaw rate for a slalom maneuver with NDI control

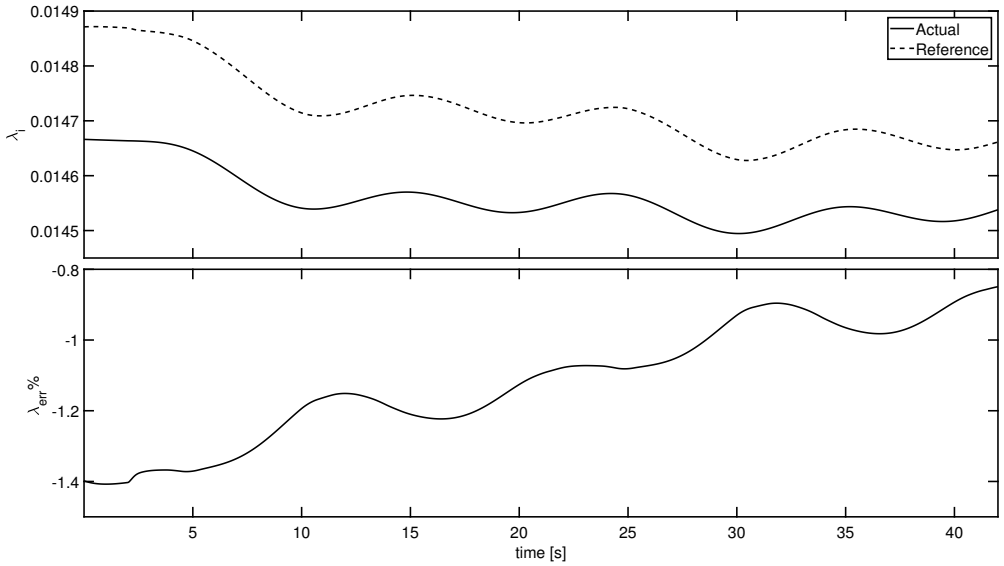

Figure 6.21: Inflwo filter behavior for a slalom maneuver with NDI control

6.3.4 Autorotation with NDI

A further test on the NDI velocity and attitude controller has been done considering the autorotation maneuver. The initial conditions are again given by a stationary-level flight at 5 m/s at an initial altitude of 100 m. After 2 s the engine fails, the system recognizes the failure and the automatic autorotation maneuver starts. The nominal steady descent conditions and flare altitude h_0 are adopted in this simulation. As specified already in section 5.6, during the steady descent the NDI velocity controller is used to follow the nominal advancing velocity while the collective is elaborated controlling the rotor angular rate, whereas during the flare, the reference velocity from the trajectory planner, is tracked by the NDI controller. Results for the velocity and the attitude are reported in Figs. 6.22-6.23 where it is possible to see that the controller correctly drives the system through the steady descent conditions and then the flare. In Fig. 6.24 it is possible to see the trajectory (altitude), the magnitude of the velocity and the rotor angular rate. Here it is clear how the main energy contributions change during the maneuver: in particular the rotor rate and the velocity are taken almost constant during the steady descent, while during the flare the rotor kinetic energy is used to reduce the velocity. Finally in Fig.6.26 it is possible to see the inflow filter behavior, which results to be less accurate than in other cases. This is probably due to the neglected effect of the fuselage which is significantly higher for longitudinal maneuver, and especially for high vertical speed conditions.

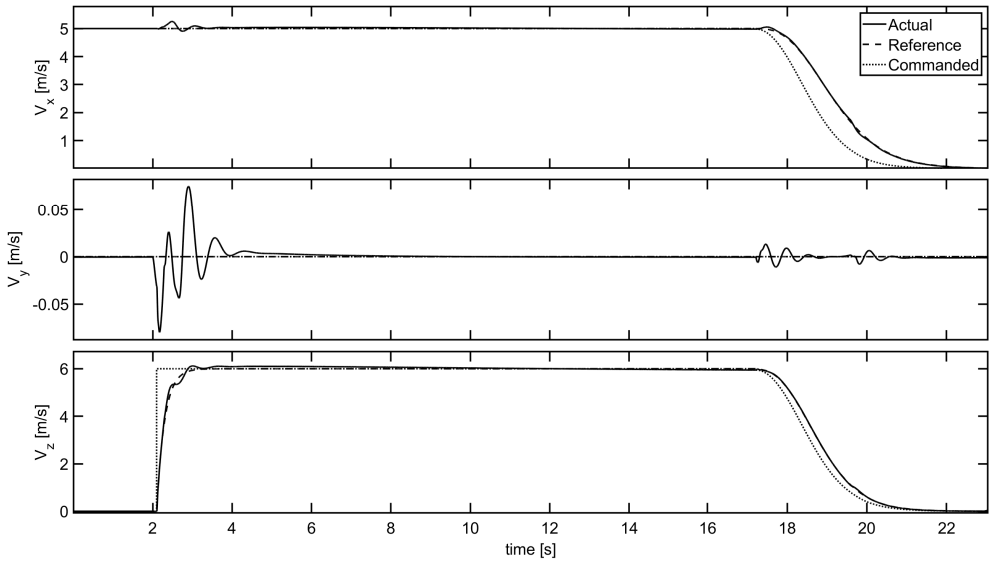

Figure 6.22: Velocities during autorotation maneuver with NDI control

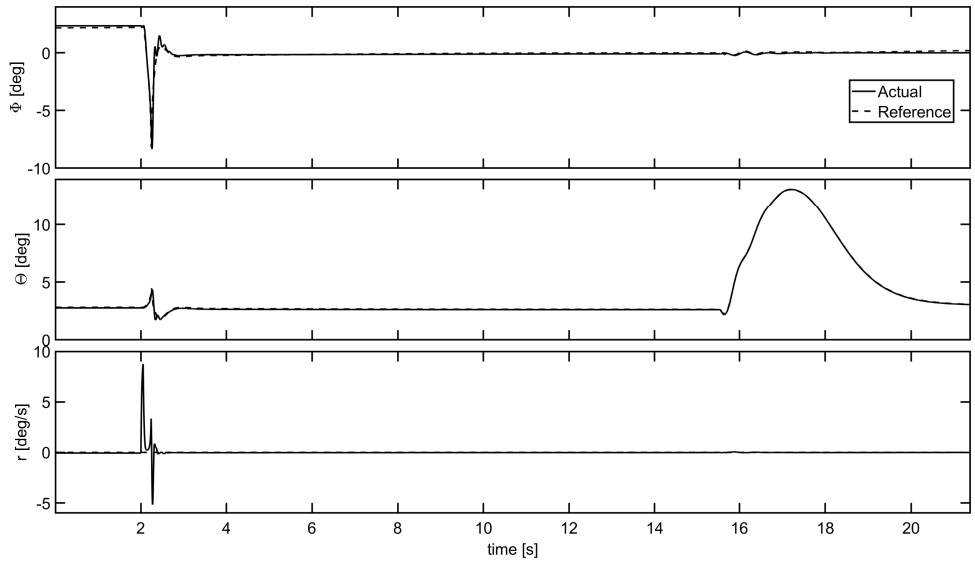

Figure 6.23: Euler angles and yawrate during autorotation maneuver with NDI control

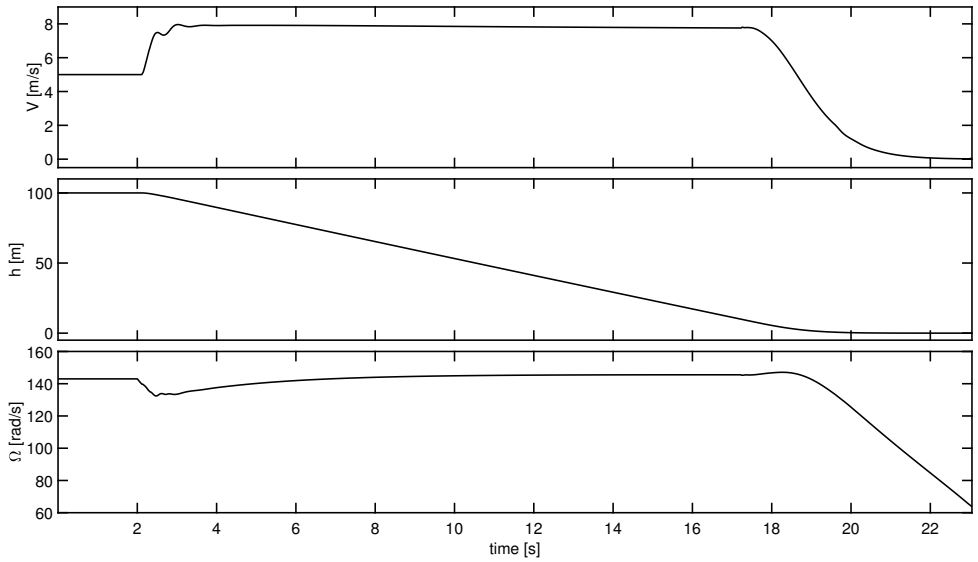

Figure 6.24: Velocity, altitude and rotor angular rate during autorotation maneuver with NDI control

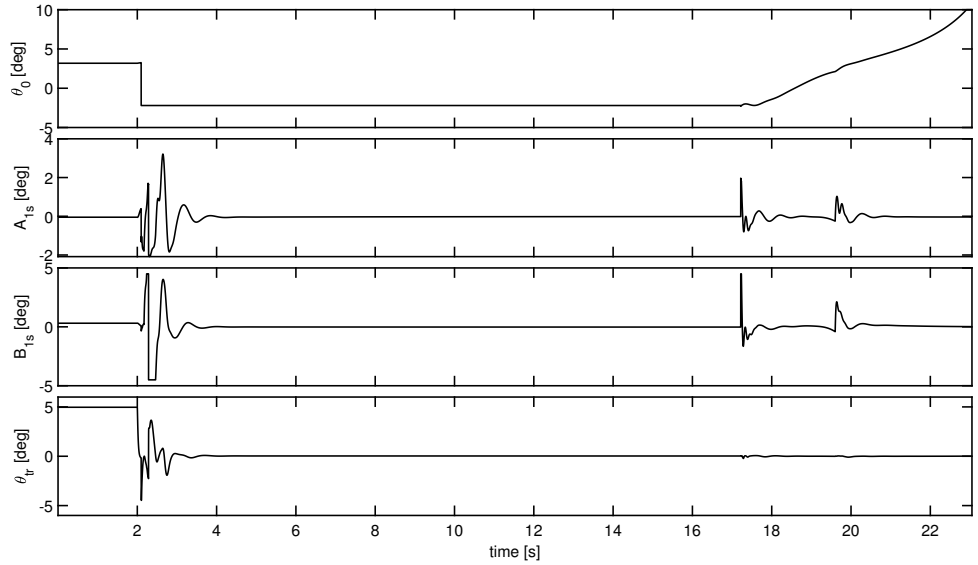

Figure 6.25: commands during autorotation maneuver with NDI control

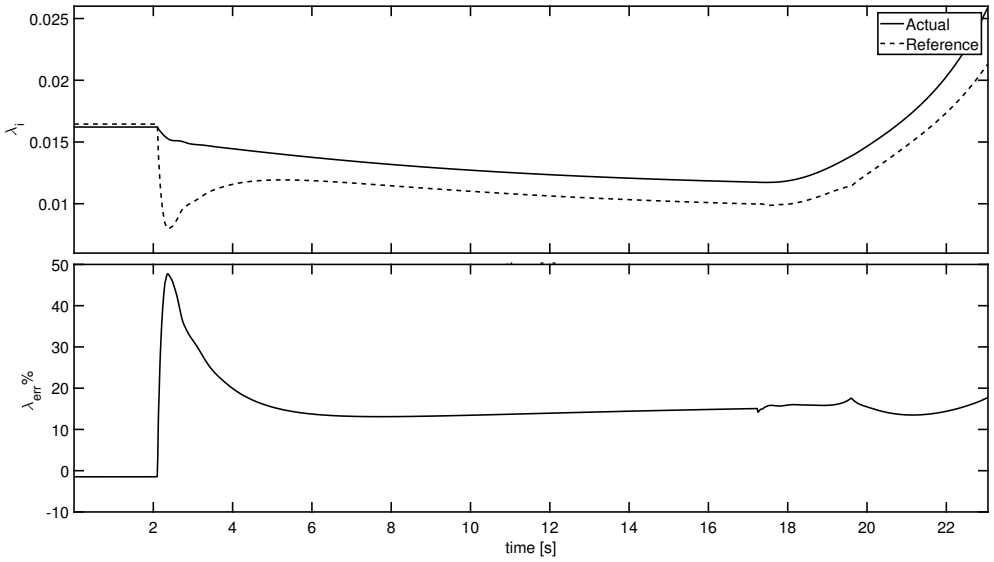

Figure 6.26: Inflwo filter behavior during autorotation maneuver with NDI control

6.4 Conclusions and future work

Two main research objectives have been addressed in this work: the development of the automatic autorotation maneuver, and the development of a nonlinear dynamic inversion controller for the helicopter.

The autorotation has been studied first, to keep its physical insight, and in the second part, the desig of a suitable automatic maneuver has been addressed. In particular, a trim algorithm, based on a medium-level order dynamic model, has been developed to calculate all the possible steady descent conditions. An analysis of these conditions, in terms of collective, angular rate, and velocities, has been done to clarify the role of these variables for the equilibrium. For the design of a suitable maneuver, the starting hypothesis is to consider three main phases: the initial transitory, the steady descent, and the flare. The design of the flare has been

conducted, trying to follow simplicity criteria, and defining a trajectory profile easily implementable on real-time systems. An optimization algorithm has also been proposed for the choice of the maneuver parameters. Finally, a linear PID based control has been adopted to perform the autorotation in a simulation environment. The simulation results have shown that the control system correctly manages to perform a safe landing in autorotation for a wide range of initial conditions (altitude, advancing velocity, and rotor angular rate). The effect of a different flare altitude has also been investigated, showing that a range of suitable altitudes can be defined for a safe landing. Strictly related to h_0 is the pitch angle maneuver, thus a correct choice of this parameter should ensure a good pitch profile. A Monte Carlo simulation campaign was also conducted to test the effect of model uncertainties on the algorithm. A 5% uncertainty has been considered for the total mass while a 10% uncertainty has been taken for the longitudinal inertia, the blades lift slope and drag coefficient, and the fuselage drag coefficient. A random error of maximum 0.1 m has also been considered for the measured altitude. After 500 simulations, the recorded results for the touch-down velocity, attitude, and rotor angular rate, demonstrated the robustness of the maneuver and the control system w.r.t. helicopter parameters uncertainties.

To improve helicopter maneuverability, a NDI controller has been developed. The system has a nested structure with an inner attitude controller and an outer velocity controller. For the attitude control, the inversion is made on the rotational dynamics of the medium-order helicopter model, while a simpler model has been considered for the translational dynamics inversion of the velocity controller. An

extended Kalman filter has also been implemented for the inflow ratio estimation. The simulation results have shown good control performance for various maneuvers, in the longitudinal plane, as in the lateral one. The automatic autorotation maneuver has also been addressed with good results.

An important enrichment of the research will be the validation of the previous numerical results, with flight tests. The first step should be the validation of the steady descent conditions. For this purpose, a safe flight test could be done by performing short descents at high altitudes with the engine running a reduced angular rate for recovery.

Another important task is the control implementation on real flight hardware. An intermediate step will be the hardware-in-the-loop simulation, where the dynamic behavior of the helicopter will be simulated, while the elaboration of the controls, will be done by the real hardware.

Bibliography

[1] Ahmadi, K., Asadi, D., Nabavi-Chashmi, S.-Y., and Tutsoy, O. Modified adaptive discrete-time incremental nonlinear dynamic inversion control for quad-rotors in the presence of motor faults. *Mechanical Systems and Signal Processing 188* (2023), 109989.

[2] Arra, M. *L'elicottero*. Biblioteca tecnica Hoepli. Hoepli, 2001.

[3] Avanzini, G., de Angelis, E. L., Fattizzo, D., and Giulietti, F. Autorotation design and simulation for a small-scale helicopter. In *48rd European Rotorcraft Forum, ERF* (2022).

[4] Avanzini, G., and Martínez, D. S. Risk assessment in mission planning of uninhabited aerial vehicles. *Proceedings of the Institution of Mechanical Engineers, Part G: Journal of Aerospace Engineering 233*, 10 (2019), 3499–3518.

[5] Bibik, P., and Narkiewicz, J. Helicopter optimal control after power failure using comprehensive dynamic model. *Journal of Guidance, Control, and Dynamics 35*, 4 (2012), 1354–1362.

[6] Bijjahalli, S., Sabatini, R., and Gardi, A. Advances in intelligent and autonomous navigation systems for small uas. *Progress in Aerospace Sciences 115* (2020), 100617.

[7] Bramwell, A., Done, G., and Balmford, D. *Bramwell's Helicopter Dynamics*, ii ed. Butterworth-Heinemann, Oxford, 2000.

[8] Bryson, A., and Ho, Y. *Applied Optimal Control*. Taylor and Francis Group, New York, 1975.

[9] Byrd, R. H., Gilbert, J. C., and Nocedal, J. A trust region method based on interior point techniques for nonlinear programming. *Mathematical Programming 89*, 1 (Nov. 2000), 149–185.

[10] Cheeseman, I., Bennett, W., Council, A. R., and of Supply, G. M. *The Effect of the Ground on a Helicopter Rotor in Forward Flight*. ARC technical report. H.M. Stationery Office, 1957.

[11] Chen, R. T. N. A simplified rotor system mathematical model for piloted flight dynamics simulation. *NASA Technical Memorandum*, 78575 (1979).

[12] Chen, R. T. N. Effects of primary rotor parameters on flapping dynamics. *NASA Technical Paper*, 1431 (1980).

[13] Choi, H. S., KIM, E., YOU, D., and Shim, D. Improvements in small-scale helicopter rotor modeling for the real-time simulation of hovering flight. *Transactions of the Japan Society for Aeronautical and Space Sciences 54* (2011), 229–237.

[14] Connolly, L., O'Gorman, D., and Tobin, E. Design and development of a low-cost inspection uas prototype for visual inspection of aircraft. *Transportation Research Procedia 59* (2021), 85–94. 10th International Conference on Air Transport – INAIR 2021, TOWARDS AVIATION REVIVAL.

[15] da Costa, R. R., Chu, Q. P., and Mulder, J. A. Reentry flight controller design using nonlinear dynamic inversion. *Journal of Spacecraft and Rockets 40*, 1 (2003), 64–71.

[16] de Angelis, E. L., Giulietti, F., Pipeleers, G., Rossetti, G., and Van Parys, R. Optimal autonomous multirotor motion planning in an obstructed environment. *Aerospace Science and Technology 87* (2019), 379–388.

[17] de Angelis, E. L., Giulietti, F., and Rossetti, G. Multirotor aircraft formation flight control with collision avoidance capability. *Aerospace Science and Technology 77* (2018), 733–741.

[18] de Angelis, E. L., Giulietti, F., Rossetti, G., Turci, M., and Albertazzi, C. Toward smart air mobility: Control system design and experimental validation for an unmanned light helicopter. *Drones 7*, 5 (Apr 2023), 288.

[19] G., P. *Helicopter Flight Dynamics: The Theory and Application of Flying Qualities and Simulation Modelling*. John Wiley and Sons, Ltd, 2007.

[20] Gopmandal, F., and Ghosh, A. Lqr-based mimo pid control of a 2-dof helicopter system with uncertain cross-coupled gain. *IFAC-PapersOnLine 55*,

22 (2022), 183–188. 22nd IFAC Symposium on Automatic Control in Aerospace ACA 2022.

[21] Heffley, R. *Minimum-complexity Helicopter Simulation Math Model*. 1988.

[22] Johnson, W. Helicopter optimal descent and landing after power loss. *NASA Technical Memorandum 73244* (1977).

[23] Johnson, W. *Helicopter Theory*. Dover Books on Aeronautical Engineering Series. Dover Publications, 1994.

[24] Kirchner, M. R., Ball, E., Hoffler, J., and Gaublomme, D. Reachability as a unifying framework for computing helicopter safe operating conditions and autonomous emergency landing ∗∗this research was supported in part by the navy innovative science and engineering program under grant 219wfd-sg-18-003 and grant n00421-19-wx00648 and in part by the office of naval research under grant n00014-19-wx00546. *IFAC-PapersOnLine 53*, 2 (2020), 9282–9287. 21st IFAC World Congress.

[25] Kovacova, M., Gravio, G. D., and Patriarca, R. Unmanned aerial systems: Status and forthcoming challenges for safety risk management. *Transportation Research Procedia 65* (2022), 329–338. 11th International Conference on Air Transport – INAIR 2022, Returning to the Skies.

[26] Leishman, J. *Principles of Helicopter Aerodynamics*. Cambridge Aerospace Series. Cambridge University Press, 2002.

[27] Lopez, C. A., and Wells, V. L. Dynamics and stability of an autorotating rotor/wing unmanned aircraft. *Journal of Guidance, Control, and Dynamics 27*, 2 (2004), 258–270.

[28] Luxhøj, J. T. A socio-technical model for analyzing safety risk of unmanned aircraft systems (uas): An application to precision agriculture. *Procedia Manufacturing 3* (2015), 928–935. 6th International Conference on Applied Human Factors and Ergonomics (AHFE 2015) and the Affiliated Conferences, AHFE 2015.

[29] Mandirola, M., Casarotti, C., Peloso, S., Lanese, I., Brunesi, E., and Senaldi, I. Use of uas for damage inspection and assessment of bridge infrastructures. *International Journal of Disaster Risk Reduction 72* (2022), 102824.

[30] Marcos, A., Peñín, L. F., Caramagno, A., Sommer, J., and Belau, W. Atmospheric re-entry ndi control design for the hopper rlv concept. *IFAC Proceedings Volumes 40*, 7 (2007), 786–791. 17th IFAC Symposium on Automatic Control in Aerospace.

[31] Martinez, J. G., Albeaino, G., Gheisari, M., Issa, R. R., and Alarcón, L. F. isafeuas: An unmanned aerial system for construction safety inspection. *Automation in Construction 125* (2021), 103595.

[32] Martín-Lammerding, D., Astrain, J. J., Córdoba, A., and Villadangos, J. An ontology-based system to avoid uas flight conflicts and collisions in dense traffic scenarios. *Expert Systems with Applications 215* (2023), 119027.

[33] Meng, W., and Chen, R. Study of helicopter autorotation landing following engine failure based on a six-degree-of-freedom rigid-body dynamic model. *Chinese Journal of Aeronautics 26*, 6 (2013), 1380–1388.

[34] Mettler, B. *Identification Modeling and Characteristics of Miniature Rotorcraft*. Springer US, 2013.

[35] Opromolla, R., and Fasano, G. Visual-based obstacle detection and tracking, and conflict detection for small uas sense and avoid. *Aerospace Science and Technology 119* (2021), 107167.

[36] Ozana, S., Vojcinak, P., Pies, M., and Hajovsky, R. Mixed sensitivity h8 control for helicopter model. *IFAC Proceedings Volumes 46*, 28 (2013), 104–109. 12th IFAC Conference on Programmable Devices and Embedded Systems.

[37] Pang, B., Hu, X., Dai, W., and Low, K. H. Uav path optimization with an integrated cost assessment model considering third-party risks in metropolitan environments. *Reliability Engineering and System Safety 222* (2022), 108399.

[38] Peters, D., and HaQuang, N. Dynamic inflow for practical applications. *Journal of the American Helicopter Society 33*, 4 (1988), 64–85.

[39] Prouty, R. *Helicopter Performance, Stability, and Control*. R.E. Krieger Publishing Company, 1995.

[40] Ress, R., Grawunder, M., and Breitsamter, C. Aerodynamic analysis of a helicopter fuselage with rotating rotor head.

[41] Seddon, J. *Basic Helicopter Aerodynamics*, i ed. AIAA education series. American Institute of Aeronautics and Astronautics, 1990.

[42] Stádník, J., Šárka Hulínská, and Kraus, J. Comparison of methods for the safety evaluation of uas operation. *Transportation Research Procedia 65* (2022), 78–85. 11th International Conference on Air Transport – INAIR 2022, Returning to the Skies.

[43] Taamallah, S., Bombois, X., and Van den Hof, P. M. Trajectory planning and trajectory tracking for a small-scale helicopter in autorotation. *Control Engineering Practice 58* (2017), 88–106.

[44] Tabassum, A., and Bai, H. Dynamic control allocation between onboard and delayed remote control for unmanned aircraft system detect-and-avoid. *Aerospace Science and Technology 121* (2022), 107323.

[45] Talaeizadeh, A., Antunes, D., Pishkenari, H. N., and Alasty, A. Optimal-time quadcopter descent trajectories avoiding the vortex ring and autorotation states. *Mechatronics 68* (2020), 102362.

[46] Talbot, P. D., Tinling, B. E., Decker, W. A., and Chen, R. T. N. A mathematical model for a single main rotor helicopter for piloted simulation. *NASA Technical Memorandum*, 84281 (1982).

[47] Tripathi, A. K., Patel, V. V., and Padhi, R. Autonomous landing of uavs under unknown disturbances using ndi autopilot with l1 adaptive augmentation. *IFAC-PapersOnLine 50*, 1 (2017), 3680–3684. 20th IFAC World Congress.

[48] Wang, C. J., Tan, S. K., and Low, K. H. Collision risk management for non-cooperative uas traffic in airport-restricted airspace with alert zones based on probabilistic conflict map. *Transportation Research Part C: Emerging Technologies 109* (2019), 19–39.

[49] Wang, C. J., Tan, S. K., and Low, K. H. Three-dimensional (3d) monte-carlo modeling for uas collision risk management in restricted airport airspace. *Aerospace Science and Technology 105* (2020), 105964.

[50] Yafei, C., Ruyi, Y., Guoliang, F., and Jianqiang, Y. Robust control for aircraft with reaction jets using dynamic inversion and fuzzy neural networks. *IFAC Proceedings Volumes 46*, 20 (2013), 512–517. 3rd IFAC Conference on Intelligent Control and Automation Science ICONS 2013.

[51] Yu, L., Huang, M. M., Jiang, S., Wang, C., and Wu, M. Unmanned aircraft path planning for construction safety inspections. *Automation in Construction 154* (2023), 105005.

[52] Zhang, B.-Y., and Morton, B. Robustness analysis of dynamic inversion control laws applied to nonlinear aircraft pitch-axis models. *Nonlinear Analysis: Theory, Methods and Applications 32*, 4 (1998), 501–532.